Modelling the effects of swift heavy ion irradiation on metals and band gap materials

Galvin Khara

Department of Physics and Astronomy,
& London Centre of Nanotechnology,
University College London

A thesis submitted in fulfillment of the requirements for the degree of Doctor of Engineering

September 2017

Declaration

I, Galvin Khara, confirm that the work presented in this thesis is my own. Where information has been derived from other sources, I confirm that this has been indicated in the thesis.

Relevant Publications

- **G. S. Khara**, S. Murphy, and D. Duffy. "Dislocation loop formation by swift heavy ion irradiation of metals." *Journal of Physics : Condensed Matter*, 29 (28), 285303, 2017.
- **G. S. Khara**, S. Murphy, S. Daraszewicz, and D. Duffy. "The influence of the electronic specific heat on swift heavy ion irradiation simulations of silicon." *Journal of Physics : Condensed Matter*, 28 (39), 395201, 2016.

Acknowledgements

Firstly (and most importantly), I have to thank my supervisor, Dorothy Duffy, whose guidance was instrumental in every facet of this research. I would also like to thank Samuel Murphy and Szymon Daraszewicz, collaborating with excellent researchers such as yourselves was a real pleasure. Most of the work contained in this thesis would not be possible without the software developed by Ilian Todorov, and our brief projects together (along with Michael Seaton) were always fun and stimulating.

Other scientists I have to mention are Sultan Abdul-Jawad and Selçuk Bedük, while we never discussed physics (or much science at all), your support and friendship were important to me throughout the process. I won't mention all of the close friends that have helped support me over the past few years by name, but Mutton Place has been a real special place, and that is thanks to each of you.

A massive thanks needs to be extended to my girlfriend, Antonia (LUBBS), who has been there throughout every high and low. You are my rock. I would also like to thank my sister, Garzie, who is about to embark on her own scientific journey. Finally, the biggest thank you of all is reserved for you Mum and Dad. Your constant love and support helped foster my love for science in the first place. None of this would have been possible without you both.

Table of Contents

1

Background Theory

> "The only fence against the world is a thorough knowledge of it."
>
> John Locke

The research presented in this thesis focuses on developing computational models that are capable of accurately simulating radiation damage in a variety of materials. In the most general terms, this involves the intersection of three scientific fields : materials science, quantum mechanics, and computational physics. Materials science is arguably the first scientific endeavour humans undertook, harnessing the earth's natural resources in a manner that gave our species significant survival advantages. In fact, since the emergence of Homo sapiens, our historical timeline has been named after the defining material of that period (from the stone age, bronze age, and iron age, all the way up to the present silicon age). This ability to efficiently exploit the materials around us is a uniquely human trait, and this thesis focuses on furthering our understanding of how two specific types of materials are affected by extremely fast, heavy particles; metals and band gap materials. Both of these materials properties are determined by their characteristic electronic structures, of which quantum mechanics is required to accurately describe their physical evolution when irradiated.

The interaction is made up of multiple complex processes, each evolving over distinct time periods. Initial excitations can lead to the production of point defects, which over time can lead to defect clustering, and potentially the formation of dislocation loops and voids. These changes in structure can lead to significantly different physical properties when compared to an unirradiated material. These transformations occur over the timescales of almost instantaneous excitation (a few picoseconds), all the way up to geological timescales.

This poses a real issue when trying to develop robust theoretical models from experimental observations alone, and this is where a relatively new field, computational science, proves its worth.

While properly devised experiments are the purest way of verifying the underlying physical structure of the universe, it can prove extremely difficult (or impossible) to flexibly change elements of an experiment. A more powerful source of radiation may only be possible by building another particle accelerator, or more fine-grained spectroscopic data may require an entirely different laser. Computational physics bridges the gap between theory and experiment in a manner that (given an accurate model), changing the energy or spatio-temporal resolution of an experiment can in some cases be as simple as changing a number in the input parameters. Thus the development of physically realistic and robust computer models means we have the ability to freeze, fast forward, reverse, or zoom in on an experiment in a way that is not possible when conducting real life experiments.

This rest of this chapter contains a summary of all the theoretical frameworks utilised in this thesis. It begins with a brief literature review on the results observed from various swift heavy ion irradiation experiments to date. These results are then analysed in the context of various models describing the physical mechanisms underlying swift heavy ion irradiation. These models describe the theoretical processes underpinning swift heavy ion irradiation, thus subsequently, a description of how these models are computationally implemented is outlined. The chapter ends with a final overview of the field, and suggests how research will develop in the near to long term future. A caveat applicable throughout this work : while the term radiation usually refers to any form of electromagnetic wave, or massive particle (from an electron to a C_{60} fullerene), in this thesis the term radiation is restricted to projectiles with a mass (unless otherwise explicitly stated).

1.1 Experimental Observations and Applications

Most experimental studies on the effects of radiation interacting with materials have been conducted in particle accelerators. While from a popular science perspective particle accelerators (such a the Large Hadron Collider at CERN) are primarily associated with probing and testing our understanding of fundamental particle physics at the subatomic scale, they

are also extremely important for materials science research. Nowadays, particle accelerators are capable of producing beams with energies ranging from a few keV all the way up to the tens TeV, and across this vast energy scale a huge spectrum of physical interactions are possible. In the vast majority of cases, when discussing how radiation interacts with materials, one thinks of an incoming particle colliding elastically with the nuclei of the target. This radiation may continue to penetrate the material, colliding with more nuclei in the target, while the ejected target nuclei may also have enough energy to displace other nuclei. This process is known as a collision cascade, lies on the lower edge of this energy scale, and is not the subject of this thesis.

As the energy of incident radiation increases ($\geq$ MeV) an interesting phenomenon occurs. The projectile no longer collides elastically with the nuclei of the target, instead it penetrates through the material and leaves a characteristic defect distribution (dependent on the physical properties of the target) in a narrow region surrounding the path of the projectile. This type of projectile is known as a swift heavy ion (SHI), and is the focus of this thesis. The first experimental study of damage caused by swift heavy ions was on lithium flouride [1], in 1958. The observed damage was unlike anything seen in cascades. The SHI created a defect rich amorphous cylinder along its path through the material. This defect distribution is commonly referred to as an ion track. Since then, ion tracks have been observed in many other insulators [2, 3, 4, 5], semi-conductors [6, 7, 8, 9, 10, 11, 12], and even amorphous semi-conductors [13]. Figure 1.1 shows the typical morphology of ion tracks from various angles.

Various metals [15, 16, 17, 18] have also been irradiated with swift heavy ions, however, the damage observed is distinct from that of band gap materials. Metals show a remarkable resistance to ion track formation, with defects (if any) taking the form of dislocation loops or isolated clusters at the centre of the projectile's path. This is a topic explored in depth later on in the thesis. It is important to stress that SHI irradiation is not exclusively a destructive process, for example pre-existing defects in Ni have been shown to decrease following irradiation via various swift heavy ions [19].

The ability to produce such precise and novel structural modifications in materials has a huge number of applications in nanotechnology. By far the most commonly used industrial application for swift heavy ions is in the production of track etched membranes [20]. Chemical

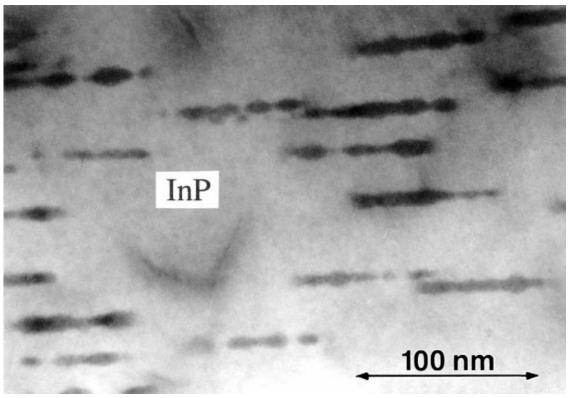

(a) Side profile of ion tracks formed in InP. [6]

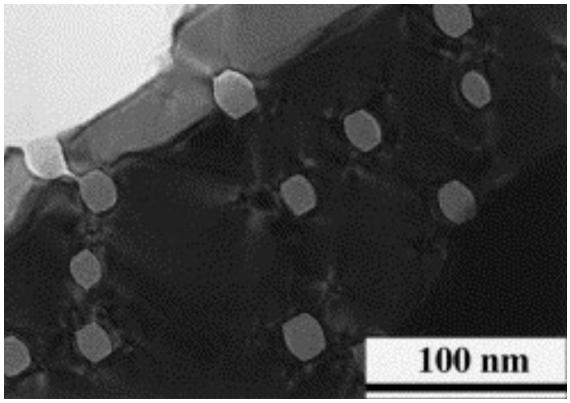

(b) Top down profile of ion tracks in GeS. [14]

Figure 1.1: Typical ion track images. Permission has been granted to republish this material.

etching is a form of pore production in a material, and the use of swift heavy ions allows for the process to be more delicately controlled and manipulated. First a polymer is irradiated by swift heavy ions, producing ion tracks in the material. These ion tracks have unique mechanical, optical, and chemical properties when compared to the undamaged bulk. When an etching chemical is applied to the material, it reacts more strongly to the ion track region, thus producing controllable micro and nanoporous membranes. This has applications in a wide variety of industries, from the biosensing, where bacteria are too large to pass through a fabricated membrane, to the purification of water via deionising, to the filtering of electromagnetic radiation. Swift heavy ions can also be used to precisely modify band gaps, something crucial in the fabrication of quantum wells and quantum dots [21, 22]. Figure 1.2 illustrates a typical track etched membrane, and a membrane capable of preventing the transfer of bacteria. Outside of nanofabrication, swift heavy ions may also play a crucial role in the production of a viable high temperature superconductor. It has been shown that the columnar defects formed via SHI irradiation of Bi-2212 leads to huge increases in the critical superconducting current [23]. A good historical account of how amorphous materials can be modified by swift heavy ion from an engineering stand point can be found in work by Rizza in 2015 [24].

A deeper understanding of the physical processes governing swift heavy ion irradiation also has a number of very important applications. The biggest determining factor in the

operational lifetime of an extraterrestrial satellite, is how long the electrical components can withstand the intense environment of space. Finally, perhaps the most important application is in the nuclear industry. Inside a nuclear reactor, reactions with actinide-bearing components can produce heavy particles in the energy range of swift heavy ions. A deep understanding of the underlying damage mechanisms can thus also have a impact on the design of safe nuclear reactors, and also safe methods of nuclear waste immobilisation. Swift heavy ions have produced a variety of defects in materials, and in turn have an even wider variety of applications. This is a significant enough motivation for the study of SHI irradiation to be worthwhile endeavour, and the rest of this chapter will summarise how this has been achieved to date.

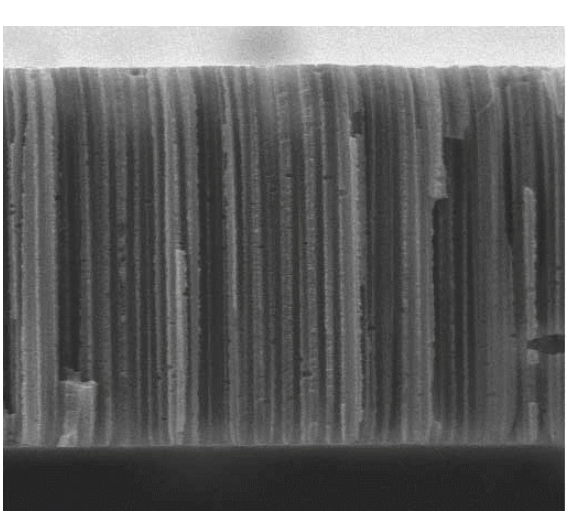

(a) Typical track etched membrane. [20]

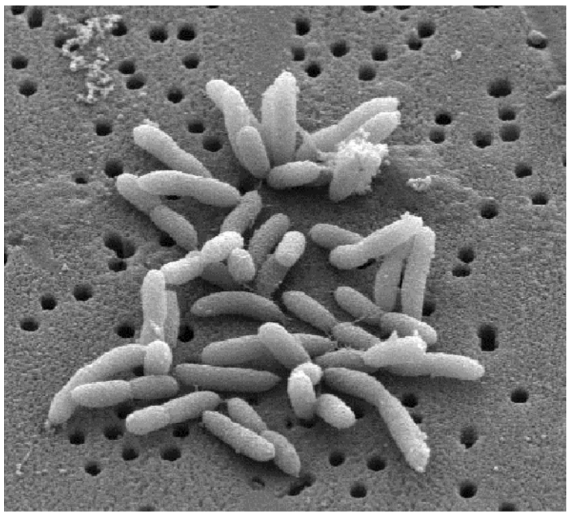

(b) Bacteria prevented from passing through a membrane.

Figure 1.2: Images of track membranes fabricated with swift heavy ions. Permission has been granted to republish this material.

1.2 Stopping Power

The main distinction between different types of radiation is how energy is transferred from the incident ions to the material they are travelling through. This process is quantified by

the stopping power, and is defined as the energy lost by the ion as it travels through the target material.

$$S = \frac{dE}{dr} \tag{1.1}$$

S is the stopping power, E kinetic energy and r distance travelled. It is a quantity that represents the sum of all the ways in which energy can be transferred from the radiation to the material, including chemical and nuclear reactions, emission of radiation, kinetic energy transfer via collisions, and changes in internal state of the projectile or target. This is broadly categorised into two distinct stopping power regimes, nuclear energy deposition, where the kinetic energy of the incident radiation is deposited directly to the nuclei in the material, and the other is electronic energy deposition, where the kinetic energy is transferred to the electrons in the material. In reality a projectile will transfer kinetic energy to the material via a combination of both of these, hence the total stopping power S can be written,

$$S = S_n + S_e, \tag{1.2}$$

where S_n is nuclear stopping, and S_e is electronic stopping. The relationship between nuclear and electronic stopping is summarised in figure 1.3. A particle with a relatively low incident energy ($\sim$ keV/amu) has a significant nuclear interaction cross-section, thus energy is predominantly lost via elastic collisions with the nuclei in the target material. High energy ions ($\geq$ MeV/amu) pass through a material much faster, this results in a much lower nuclear interaction cross section. Thus damage caused by ions in this energy range is a result of elastic electronic excitation in the target material. It is also important to stress that in the intermediate ranges a complex mixture of both processes exists. All of the work presented in this thesis is centred on the regime where electronic stopping is the dominant energy loss mechanism.

1.2.1 Time scales for defect creation

A knowledge of the time scales at which the complex dynamics occur during swift heavy ion irradiation is key for any descriptive model. While the precise time scale for these

effects is highly material dependent, distinct processes do emerge on a relative time scale. Firstly electron-electron scattering causes a local electronic temperature to be established (determined via a Fermi-Dirac distribution) within a few to a hundred femtoseconds [25]. Energy diffuses amongst the electrons on a picosecond scale, and electron-phonon scattering allows energy to transfer from the electrons to the lattice from anywhere between a few hundred femtoseconds and multiple picoseconds. Thermal equilibrium of the lattice occurs between the tens and hundreds of ps. Due to the large discrepancy between electron-electron thermalisation, and the thermalisation of the system as a whole, the temperature of the electronic system is usually assumed to be established instantaneously.

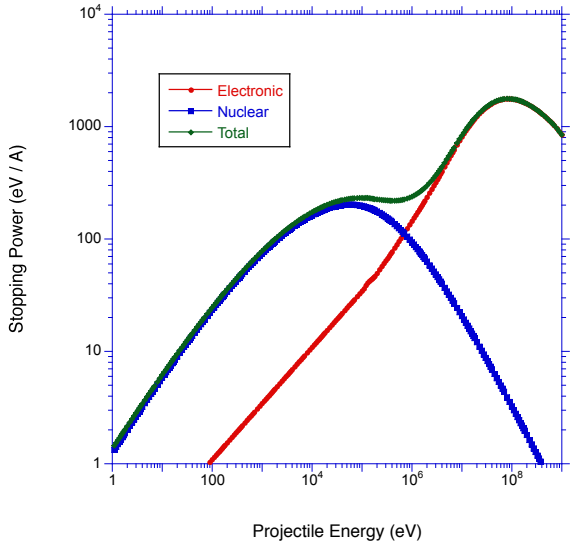

Figure 1.3: Graph illustrating the constituent stopping power contributions of an Fe ion travelling through Fe. Data obtained from SRIM [26].

A similar analysis for band gap materials is more complex, as carriers (electron-hole pairs) have a number of extra generation and recombination processes that occur. During carrier excitation, impact ionisation also contributes to carrier generation. It occurs when an excited electron transfers some energy to a bound electron, generating an extra electron-hole pair in the process. This occurs within 10 fs to a ps. Conversely, an extra carrier de-excitation process is Auger recombination (the opposite of impact ionisation), occuring on a time scale

of a few ps to ns.

1.3 Descriptive Models

The various defect distributions that arise in materials following swift heavy ion irradiation have been described. It has also been established that these defects occur due to energy being transferred to the electrons in the target material (as well as the associated time scales on which this energy transfer occurs). The next logical step is to review the models that have been developed to account for the physical processes that occur and in turn describe the defect distributions observed when a swift heavy ion passes through a target medium.

1.3.1 Coulomb Explosion Model

One of the first attempts to describe the physics occuring during swift heavy ion irradiation was the Coulomb explosion model [27], developed by R. Fleischer *et al* in 1965. The basic idea behind the model is that as the swift heavy ion enters the medium, electrons in the target are displaced by the Coulombic repulsion with the electrons in the projectile. This causes an ionisation of the material around the path of the projectile, and thus the electromagnetic repulsion between the positive charge nuclei results in disordering of the target. This model provided a successful description of the defects observed at the time, but two significant shortcomings exist within the model.

Firstly, the model is basically qualitative in nature, so the development of a robust atomistic model that can simulate the effects of the Coulomb explosion in any material is yet to be achieved. Thus a proper analysis of its validity in the realm of ion track generation is still in question. Most attempts involve artificially charging a cylindrical region at the centre of an MD cell, and observing the dynamics afterwards. This approach has been sucessfully used to model SHI irradiation in a number of insulating materials [28, 29, 30]. It has also been moderately successful in describing ion sputtering from the surfaces of a variety of materials, including Si [31], and Al_2O_3 [32].

The second criticism is how the model fails to account for the damage observed in metals. Disorder should only occur if the charge neutralisation time of the material is greater than 10^{-14} seconds. This time, τ, can be determined by,

$$\tau = \sqrt{\frac{m\epsilon_0}{ne^2}}, \tag{1.3}$$

where m is electron mass, ϵ_0 is the permittivity of free space, n is the conduction electron density, and e is the electronic charge. This value is smaller than 10^{-14} s in metals, so electrons can return to the ionised core and neutralise the target before the Coulomb explosion occurs, hence the model can not be used to explain defect formation in metals. More recent time-dependent density functional theory simulations [33] also suggest that swift heavy ions do not cause the ejection of electrons from the target material, but in way that maintains charge neutrality. This scenario is better illustrated by structural relaxation methods (described next).

1.3.2 Bond Weakening Model

A model less explored, but capable of describing electronic excitation, while maintaining charge neutrality, is the bond weakening model. In regions of high electronic excitation, a material's electron density can be sufficiently altered so that the interatomic forces also change. This in turn can contribute to materials modification. The model has mainly been applied to ultrafast laser irradiation. However the underlying physical mechanisms involved in swift heavy ion irradiation and ultrafast laser irradiation are the same. They both cause electronic excitation, but swift heavy ions cause a much higher magnitude of energy to be deposited into a smaller region of the target material. A comprehensive review of the physics underlying the structural relaxation model was conducted by Bennemann in 2004 [25]. Itoh *et al* [34] specifically discuss the model in relation to swift heavy ion irradiation.

The physical mechanisms that occur in the model are illustrated in figure 1.4. Each electronic temperature has a uniquely associated potential energy surface (PES), which describes the interatomic forces of the material. As the electronic temperature of tungsten increases, the minimum of the PES also shifts to a larger volume. This indicates an increase in the equilibrium lattice parameter at increasing electronic temperatures. At high enough temperatures, the minimum disappears, implying the interatomic forces become repulsive at all interatomic separations. A number of previous computational and experimental results

indicate that this type of bond weakening can considerably contribute to materials modification. Sciaini *et al* [35] showed that bismuth melted within 190 fs following ultrafast laser irradiation, much faster than the time for electron-phonon scattering to occur. This type of melting is known as non-thermal melting, and has also been observed in *ab initio* molecular dynamics simulations in silicon [36]. Other similar simulations have verified the same effect in silicon [37], but also found that the bonds actually strengthen in aluminium and gold.

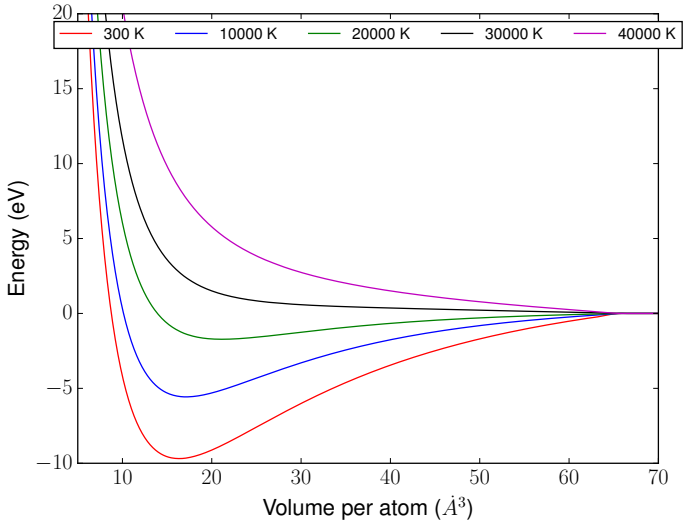

Figure 1.4: The change in the energy of a W unit cell as a function of volume, for various electronic temperatures. [38]

The main disadvantage in utilising this model is the difficulty in accurately deriving usable electronic temperature dependent potential energy surfaces. The most promising present day method is to implement them into molecular dynamics ready interatomic potentials. This way a sufficiently sized simulation can be carried out to study the effects of SHI irradiation (explored in detail in this thesis). However, only a few of these potentials exist [39, 38, 40, 41]. An alternative method is to employ *ab initio* molecular dynamics [33], however these simulations are limited to hundreds of atoms, meaning the cell dimensions required for ion track formation is impossible with current computational power. Unfortunately a large simulation cell is the only way to properly validate past experimental observations of ion tracks. This is due to the nature of tracks themselves, they are nanometer in width and

micrometer depth, so accurate reproduction requires a large enough MD volume to contain a melted region at the centre, surrounded by enough undamaged crystal that boundary effects have not contributed to the induced damage (this will be discussed in more detail in this chapter).

1.3.3 Inelastic Thermal Spike Model

By far the most ubiquitous model used to describe swift heavy ion irradiation is the inelastic thermal spike (iTS) model, of which the foundations were developed by Dessauer in 1923 [42]. The model assumes the electrons and nuclei of the material are split up into two separate, but interacting media. The entire system can then be described by a set of coupled second order differential equations. As the swift heavy ion traverses the material, the energy is deposited within the electronic subsystem, causing significant excitation. This energy then diffuses throughout the electronic system, while also being transferred to the lattice via a process known as electron-phonon coupling. This in turn leads to localised heating of the lattice, and depending on the deposited energy may lead to melting and residual defect creation post recrystallisation. Figure 1.5 illustrates the physics of the iTS model.

The inelastic thermal spike model has many variants. A detailed description of each implementation, their respective parameterisations, and a review of the materials they have been used to model is contained in the next section.

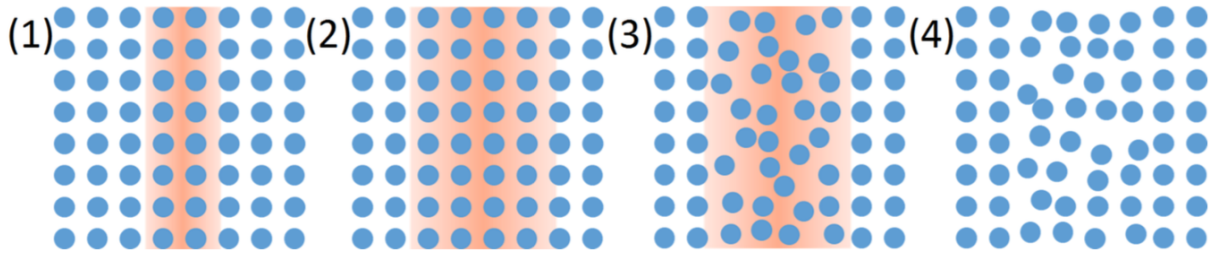

Figure 1.5: Diagram illustrating the processes that contribute to defect creation following swift heavy ion irradiation. (1) Swift heavy ion travels through material and transfers energy to electrons. (2) Energy diffuses through electronic system. (3) Electron-phonon coupling transfers energy from electrons to lattice, causing local melting. (4) Some lattice recrystallisation, resulting in the final observed defect distribution.

1.4 Computational Models

The models described previously are all qualitative in nature. They described the physical mechanisms that occur during SHI irradiation, but not how to quantitatively simulate them. This section contains a chronological review of how the inelastic thermal spike model has been traditionally implemented.

1.4.1 Two-Temperature Model

The two-temperature model (2TM) was the first attempt to computationally implement the physics of the inelastic thermal spike model, and was developed by Lifshits *et al* in 1960 [43]. The separate electronic and lattice subsystems are described by a set of coupled second order differential equations so energy lost by one system is gained by the other. These thermal diffusion equations are described below.

$$C_e(T_e)\frac{\partial T_e}{\partial t} - \nabla.[\kappa_e \nabla T_e] = -G(T_e - T_i) + A(r[v_{ion}], t), \tag{1.4}$$

$$C_i(T_i)\frac{\partial T_i}{\partial t} - \nabla.[\kappa_i \nabla T_i] = +G(T_e - T_i), \tag{1.5}$$

Here the subscript e references the electronic system, and i the lattice. T is the temperature, t is time, v is velocity. C is the specific heat capacity, κ the thermal conductivity, G the electron-phonon coupling, and A is the characteristic source term for the irradiation.

The specific heat capacity is defined as the amount of energy required to change one cubic metre of a material's temperature by one degree Kelvin. Thus it is a measure of a material's ability to store heat. The lattice component of the specific heat is measurable from past experiments. However, the electronic component proves a little more complicated. Elementary statistical mechanics predits a constant electronic specific heat of $\frac{3}{2}k_B$ per electron in 3 dimensions. In reality, at low temperatures the value is much lower due to Pauli's exclusion principle inhibiting the homogeneous excitation of electrons with the same quantum state. A quantum mechanical description of the electronic specific heat takes the form,

$$C_e = \int_{-\infty}^{\infty} g(\epsilon) \frac{\partial f(\epsilon, \mu, T_e)}{\partial T_e} \, \epsilon \, d\epsilon, \tag{1.6}$$

where $g(\epsilon)$ is electronic density of states (DOS) at the energy ϵ, μ is the chemical potential at electronic temperature T_e, and $f(\epsilon, \mu, T_e)$ is the Fermi-Dirac distribution function at these values. Various metals have been characterised in this way by Lin *et al.* [44]. However, the majority of 2TM experiments have utilised a number of approximations for the electronic specific heat [45]. A low temperature approximation is imposed via the Sommerfeld-Drude model [46, 47, 48, 49]. This approximation states that the electronic specific heat capacity is described by a homogeneously excited free electron gas,

$$C_e(T_e) = \left(\frac{\pi^2 k_B n_e}{2} \right) \frac{T_e}{T_F}, \tag{1.7}$$

where n_e is the electron density, and T_F is the Fermi-temperature, defined as,

$$T_F = \left(\frac{\hbar^2}{2 m_e k_B} \right) (3\pi^2 n_e)^{2/3}. \tag{1.8}$$

This low temperature linear approximation becomes constant at the classical limit of $\frac{3}{2}k_B$ per electron at $T_e > \frac{3}{\pi^2} T_F$. One clear problem arises in the application of this approximation to band gap materials, namely that electrons in a band gap are bound and unable to contribute to excitation instantaneously. Most past work attempts to overcome this hurdle by assuming hot electrons in a band gap material behave in a similar fashion to a metal [50].

Thus the same free electron gas approximation described has been used for materials such as quartz [45]. Another approximation involves neglecting the low temperature limit completely, and assuming that the electronic specific heat takes the classical form of $\frac{3}{2}k_B$ per electron [51, 52, 53]. However, both of these approximations fail to account for the vital contribution from the band gap itself. Thus an *ab initio* calculation of the specific heat (for both metals [44] and band gap materials [54]) ensures the most physically realistic possible parameterisation is taken into account. This is a central issue dealt with in this thesis, and will be discussed in more detail later. It is also worth noting that while these methods are currently the best possible avenue for accurate high temperature parameterisations, they still have a contain a number of approximations. One is to due to the fact DFT only accounts for the valence electrons in the material, and as SHI irradiation can excite electrons to temperatures up to 100,000K (if even only for a few fs), core electrons will be excited at this level of excitation. Another, perhaps more fundamental limitation, arises from neglecting the motion of the lattice itself. As the lattice melts, crystal symmetry is broken, and the resulting sharp peaks and troughs in the equilibrium density of states get strongly smeared. However, the work of Zhang *et al* [55] show that for metals, this contribution is not significant enough to invalidate electronic specific heats derived by ground state ab initio methods.

The thermal conductivity determines a material's ability to transfer heat. It is made up of both a lattice and electronic component, and in metals the electronic part significantly dominates due to the availability of free electrons. At low temperatures the thermal conductivity of a metal, κ, is determined using the Wiedemann-Franz law, $\kappa = LT\sigma$, where L is the Lorentz number, and σ is the electronic conduction. It is also worth noting that this assumes equilibrium conditions between the electrons and lattice. A more general form of the electronic thermal conductivity from the Sommerfeld-Drude model takes the form,

$$\kappa_e = \frac{1}{3}{v_e}^2 C_e \tau_e, \tag{1.9}$$

where v_e is the electron velocity, and τ_e is the electron relaxation time. A number of other approximations have been used to simplify this expression [56, 57], leading to $\kappa_e \approx \kappa_0 \frac{T_e}{T_i}$, where κ_0 is the thermal conductivity at room temperature. In band gap materials the situation is more complicated, as both the electronic and thermal conductivities are significant. It is customary to describe the electronic component in terms of the electronic

diffusivity, D_e,

$$\kappa_e = D_e C_e \tag{1.10}$$

Initial attempts to estimate D_e involved recasting equation 1.9 such that,

$$D_e = \frac{1}{3} v_F l, \tag{1.11}$$

where l is the electron-electron mean free path. An upper bound equal to the material's interatomic distance yields a diffusivity of roughly $2\,\mathrm{cm}^2/\mathrm{s}$ [58] . However this completely neglects all temperature dependencies, severely limiting the predictive power of the model. The diffusivity can be related to the electron mobility, μ_e, using the Einstein-Smoluchowski relation,

$$D_e = \frac{1}{e} \mu_e k_B T \tag{1.12}$$

Here, e is the charge on an electron. The electron mobility is a well known quantity for a number of band gap materials (at room temperature), thus allowing the diffusivity to be calculated. Dufour *et al* [45] then suggested a method for incorporating a temperature dependence which is based on Toulemonde's upper bound of $2\,\mathrm{cm}^2/\mathrm{s}$ (for all materials based roughly on interatomic distances). Recently, however, there has been attempts to characterise the temperature dependent mean free paths using Monte Carlo methods to model electron transport in silicon [59], based on analytical models by Pop *et al* [60, 61]. While this marks a significant leap forward in calculating the electronic diffusivity of a band gap material, the work by Akkerman *et al* [59] only treats two lattice temperatures, 300 K and 1000 K. A much more complete dataset of the electronic and lattice temperature dependence of this diffusivity is required for a truly predictive model.

The next key parameter in equation 1.4 is the electron-phonon coupling, G. It describes the rate of energy exchange between the lattice and electrons. An excellent general description for the interaction between electrons and phonons in a material can be found in the classic textbook by Ziman [62]. A complex set of interactions occur between an excited electronic and lattice system, and treatments involve considering non-adiabatic perturbations to the adiabatic approximation in the Born-Oppenheimer approximation [63]. This involves com-

plex quantum field theory considerations, and are beyond the scope of this thesis. However, as it is critical in the context of swift heavy ion irradiation modelling, a concise description of how the term has been considered follows.

Due to the highly non-equilibrium nature of the dynamics induced by swift heavy ion irradiation, there remains a significant uncertainty in the electron-phonon coupling of all but a few materials. Thus in the vast majority of literature, the electron-phonon coupling term is treated as a fitted parameter (fitted to determine the correct melt radius). This leads to extra problems in the case of band gap materials [58], where,

$$G = \frac{D_e C_e}{\lambda^2} \tag{1.13}$$

λ is the electron-phonon mean free path length. In this equation, initial approximations for both D_e and C_e mean that despite G being fitted to melt radii, there is far too much uncertainty in every component parameter for the method to be useful. One of the most common methods for calculating G is via high resolution optical pump probe reflectivity experiments. Here a material is initially pulsed via femtosecond laser, exciting the electrons. A number of other pulses follow, and via measuring the transient reflectivity (which is dependent on both the lattice and electronic temperatures, which naturally fits into the 2TM) the electron-phonon relaxation time can be determined. This has been achieved for metals [64, 65], and band gap materials [66]. These experimental results also can vary appreciably, as they rely on an accurate parameterisation of the reflectivity to the electronic temperature.

These results also only apply to the temperatures at which the experiments were conducted. To maximise the predictive accuracy of the model, a solid theoretical method for deriving an electronic temperature dependent electron-phonon coupling is key. So far this has only been achieved for metals. The method is based on work conducted by Allen *et al* [67], in which the phonon spectrum of a material is calculated over a number of different electronic temperatures. The electronic temperature dependent electron-phonon coupling term can be written as,

$$G_0(T_e) = \frac{2\pi g(\epsilon_F) k_B}{\upsilon} \int d\omega \int d\epsilon \, \alpha^2 F(\epsilon, \epsilon + \hbar\omega, \omega) \Big[f(\epsilon) - f(\epsilon + \hbar\omega) \Big] \tag{1.14}$$

Here, $g(\epsilon_F)$ is the density of states per unit cell at the Fermi energy, υ is the unit cell volume, $f(\epsilon)$ is the Fermi-Dirac distribution at temperature T_e, ω is the phonon frequency, and α^2F is the Eliashberg function. This method has been used to derive the temperature dependent electron-phonon coupling of numerous metals, including Bi [68], W [65], and Au [69]. A temperature dependent parameterisation was proposed by Lin *et al* [44], with a number of extra metals also characterised. Despite the difficulties of accurately determining the electron-phonon coupling, recent work has achieved significant successes in bridging the gap between theoretical and experimental postulates in tungsten [65].

A similar extension for band gap materials is even more complex, and thus remains undetermined. This is due to the fact that the electron-phonon coupling in equation 1.14 depends on the density of states at the Fermi level, which is zero in a band gap material. The best possible parameterisation would come from treating the temperature dependence of equation 1.13,

$$G(T_e) = \frac{D_e(T_e)C_e(T_e)}{\lambda(T_e)^2}, \tag{1.15}$$

where, $C_e(T_e)$ could be determined via *ab initio* methods [44], and the diffusivity and mean free path can be determined by the same method outlined by Akkerman *et al* [59].

The final electronic component of equation 1.4 is the source term. This describes the characteristic spatial and temporal energy deposited into the electronic system as the swift heavy ion penetrates through the material. This spatial deposition is characterised by the velocity of the impinging ion, the so called 'velocity effect', where increasing the velocity of an ion results in a more concentrated level of electronic excitation [2, 70]. Traditionally the spatial deposition is taken to be Gaussian, and the temporal deposition is exponential. The source term is normalised so integration over time and space results in the corresponding electronic stopping power, S_e, of the swift heavy ion [71].

$$S_e = \int_{t=0}^{\infty}\int_{r=0}^{r_{max}} 2\pi A(r[v_{ion}], t)r\, dr\, dt \tag{1.16}$$

Here τ is the characteristic temporal deposition time (usually assumed to be 1 fs, the time to slow down delta ray electrons [53]) and r_{max} is the maximum spatial distance of the excited electrons laterally from the centre of the cell (this is assumed to be 5σ, where σ is

the standard deviation of the Gaussian spatial deposition). The source term can be split up into individual temporal and spatial contributions following a change of variable.

$$A(r[v_{ion}], t) = AD(r[v_{ion}])\tau^{-1}e^{-\tau^{-1}t}, \tag{1.17}$$

Where the spatial component can be expressed as,

$$D(r[v_{ion}]) = \frac{S_e}{\sqrt{2\pi\sigma^2}} \exp\left[-\frac{r^2}{2\sigma^2}\right], \tag{1.18}$$

and where r is the lateral distance from the centre of the projectile's path. The spatial region in which most of the excitation occurs is defined by the mean absorption radius, r'_{ion}, and is determined via Bohr's principle of adiabatic invariance [72]. This can be calculated easily for a non-relativistic ion travelling through a band gap material by linking the transit time of the passing ion to the reaction time of the electrons, resulting in,

$$r'_{ion} = \frac{\hbar v_{ion}}{2E_g}, \tag{1.19}$$

where E_g is the material's band gap. This mean absorption radius is used as the standard deviation of the spatial component. A calculation of this quantity for metals is much more difficult, and thus the broadly applicable source term suggested by Waligorski [73] is the most accurate source term formulation to date. This was based on deriving an analytical expression for the energy deposited by charged particles (in the same energy range as SHIs). The main improvement stems from accounting for the maximum and minimum energy range of the initial excited delta electrons.

Due to uncertainty in the parameterisation of the two-temperature formalism, the initial applications of the model relied on making a number of broad assumptions in order to gain any physical insights. The best early application of the model to metals was achieved by Wang *et al* [71]. By choosing a valence electron number of two for all the metals studied (Ti, Zr, Co, Al, Cu, Nb, Ag, Fe, Be, Ga, and Ni), the work examined which materials should be sensitive to defect creation via swift heavy ion irradiation (with a number of good agreements with experimental data). The main message from this work is that the sensitivity of a material to electronic excitation is determined by the mean free path (equation 1.13). The simplicity of this parameter in describing a materials response to SHI irradiation forms

a significant portion of investigation in this thesis.

While the model was capable of making a few predictions when applied to metals, initial implementations for band gap materials required even broader assumptions in the parameterisation. Thus the mean free path was fitted to experimental track radii, allowing for the prediction of thresholds for damage creation, and track radii values outside the experimental data. Toulemonde *et al* [58] describes a thorough analysis of the descriptive power of the two-temperature model when applied to band gap materials. This work also stresses the mean free path as the pivotal parameter, and compares various insulators mean free path to band gaps. A general inverse relationship is observed between the mean free path and band gap.

Looking past an incomplete knowledge in the parameterisation of the two-temperature model, a number of key difficulties remain. The first is that while insulating materials are the most sensitive in forming defects when irradiated by SHI, the coupled heat diffusion equations (eq 1.4) have no means of explicitly treating the dynamics of carriers in a band gap. Secondly, most implementations of the model use a continuum formulation. This means there are no well defined atomic positions, so individual atomistic detail is impossible. Once a region of the model is above the melting temperature of the material, it is assumed to form an ion track. Thus processes such a superheating, shock waves, volume changes during phase transitions, and the specific nature of the defect distributions observed are impossible with the model. The proceeding section describes a hybrid model which overcomes these coarse grained limitations [72].

1.4.2 Two-Temperature Molecular Dynamics

Molecular dynamics (MD) is a simulation technique where a discrete set of particles evolve deterministically according to Newton's equation of motion. This method of simulation allows the user to explicitly track the trajectory of each individual particle.

The catalyst for work aimed at studying the effects of electronic excitation within a molecular dynamics context was a model proposed by Caro and Victoria in 1989 [74]. While the work was not motivated by swift heavy ions, it proved pivotal in incorporating electronic effects into molecular dynamics simulations. The idea was to model the electronic contri-

butions in radiation damage cascade (lower energy ions which interact elastically with the target nuclei) simulations via a damping force in the MD equations. This is analogous to the electrons acting as a viscous medium which slows down the lattice dynamics (as in cascades the lattice is initially excited, with energy being transferred to the cooler electrons). This idea was built upon in further research by Finnis *et al* [75].

The model outlined by Duffy and Rutherford [76] forms the basis of all of the models used throughout this thesis. The key premise is that energy from the electronic system (which is described by the tradiational two-temperature formalism in equation 1.4), can transfer energy stochastically to a molecular dynamics cell via an inhomogeneous Langevin thermostat. The lattice heat diffusion in equation 1.4) is replaced by a modified version of Newton's second law.

$$m_i \frac{\partial \mathbf{v}_i}{\partial t} = \mathbf{F}_i(t) - \gamma_i \mathbf{v}_i + \tilde{\mathbf{F}}_i(t), \tag{1.20}$$

where m_i and $\mathbf{v}_i$ are the mass and velocity of the atom i at time t, $\mathbf{F}_i$ is the deterministic force on i determined by the interatomic potential, γ_i is the frictional force allowing energy to be transferred to the electronic subsystem, and $\tilde{\mathbf{F}}_i$ is the stochastic force allowing energy to transfer from the electronic subsystem. This hybrid two-temperature and molecular dynamics model will be referred to as the 2T-MD model throughout this thesis, and a more detailed description of the implementation is contained in the methodology.

Despite the 2T-MD model being relatively new in comparison the original 2TM formalism, it has been applied to swift heavy ion irradiation in metals [77], semi-conductors [78, 79], and insulators [54, 80]. Each of these pieces of work highlight how much accessing individual atomistic trajectories within this hybrid model leads to much richer results. The most successful demonstration of the two-temperature models validity in the context of radiation damage simulations did not come in the domain of studying swift heavy ions, but in the physically similar area of laser irradiation. Daraszewicz *et al* [81] showed excellent agreement between experimental and simulated Bragg peaks for a variety of laser irradiated gold nanofilms. This work demonstrates that, despite all of the valid criticisms within utilising the two-temperature for electronic excitations (summed up well in the work by Klaumunzer [72]), it remains the most successful simulation model, at least when applied to metals. The application of this hybrid approach to band gap materials also forms a significant portion

of this thesis. However, significant doubts still remain with regards to applying equation 1.4 to band gap materials (no band gap terms are explicitly characterised within the model), so other more complex extensions of the model will be explored next.

1.4.3 Extending the inelastic thermal spike model

The first attempt at incorporating band dynamics into the carrier subsystem (no longer just electrons, as holes must also be considered) was achieved by Van Driel in 1987 [82]. The entire development of the model was fuelled by a motivation to understand ultrafast dynamics in silicon following laser irradiation. In fact, to this day, very few papers have been published applying the model to swift heavy ion irradiation [83, 84]. The central basis in the development of the model is that carrier concentration and band gap vary spatially in semiconductors and insulators, something unable to be accounted for by regular incarnations of the TTM. The implementation is based on a reformulation of Boltzmann's transport equations, by taking into account the conservation of carrier density as well as carrier energy. Only electrons which have been excited to the conduction band (and corresponding holes in the valence band) can carry energy. Thus an extra conservation equation is required to deal with carrier generation and recombination.

$$\frac{\partial N}{\partial t} - \nabla \cdot J = G_{e-h} - R_{e-h} \tag{1.21}$$

Here N is the concentration of carriers (electron-hole pairs, as the model is assumed to be charge neutral), G_{e-h} is the carrier generation rate, and R_{e-h} is the carrier recombination rate. J is the carrier current density.

$$J = -D(T_i)\left(\nabla N + \frac{2N}{k_B T_e}\nabla E_g + \frac{N}{2T_e}\nabla T_e\right) \tag{1.22}$$

D is the ambipolar diffusivity of a bound electron-hole pair and E_g is the band gap. The temperature of the holes and electrons are assumed to be equal. The carrier energy density, U, is the total energy in the carrier subsystem.

$$U = NE_g + 3Nk_B T_e, \tag{1.23}$$

This key term is made up of two components, the energy to excite the electrons across the band gap (NE_g), and the kinetic energy of the carriers once they have been excited $3Nk_BT_e$. The next equation describes the generation of carrier energy following SHI irradiation,

$$\frac{\partial U}{\partial t} - \nabla \cdot W = -\frac{C_{e-h}}{\tau_{ep}}(T_e - T_i) + A(r[v_{ion}], t) \tag{1.24}$$

W is the carrier energy flux density, C_{e-h} is the electron-hole specific heat capacity, τ_{ep} is the electron-phonon relaxation time, and $A(r[v_{ion}], t)$ is the same source term as described previously. The two terms on the right hand side of equation 1.24 represent a sink (when $T_e > T_i$) and source term for carrier energy respectively. The carrier energy flux density, which describes the amount of carrier energy crossing a given area, is,

$$W = (E_g + 4k_BT_e)J - (\nabla\kappa_e + \nabla\kappa_h)\nabla T_e \tag{1.25}$$

Here κ_e and κ_e are the electron and hole thermal conductivities respectively. Using equation 1.23, the carrier specific heat C_{e-h} takes the form,

$$C_{e-h} = \frac{\partial U}{\partial T_e} = N\frac{\partial E_g}{\partial T_e} + 3Nk_B \approx 3Nk_B \tag{1.26}$$

In simplified terms, a swift heavy ion will deposit energy into the carrier subsystem, with 1/3 of the energy going into exciting carriers across the band gap, and 2/3 contributing to their kinetic energy [85].

Recombination in Si, R_{e-h}, is dominated by two competing processes, Auger recombination, and impact ionisation [82, 86].

$$-R_{e-h} = -\gamma N^3 + \delta(T_e)N \tag{1.27}$$

Here γ and δ are the Auger and impact ionisation coefficients respectively. The Auger process reduces the total number carriers, as an electron and hole recombine, and energy subsequently gets transferred to another electron in the conduction band. Impact ionisation is the opposite of this process, an excited electron can excite a bound electron in the valence band, while itself still remaining in the conduction band. Both of these processes are non-

radiative, and do not change the total carrier energy (Auger process results in an increase in kinetic energy, and impact ionisation results in a decrease in kinetic energy). However, Auger recombination does increase the temperature of the carrier subsystem, which can increase the rate of energy transferred to the lattice (depending on the electron-phonon coupling).

There exists a whole host of other process which can cause carrier excitation / de-excitation in band gap materials, highly dependent on the properties of the material (band gap, impurity level, etc), and are discussed in more detail by Duffy *et al* [87]. Other examples of excitation processes include Schokeley-Read-Hall recombination, electron trapping and self-trapping. However, none of these processes are significant in silicon (where impact ionisation and Auger recombination are the dominant excitation mechanisms). The lattice subsystem in this extended two-temperature model is identical to that of the traditional formalism,

$$C_i(T_i)\frac{\partial T_i}{\partial t} - \nabla.[\kappa_i \nabla T_i] = \frac{C_{e-h}}{\tau_{ep}}(T_e - T_i) \tag{1.28}$$

Again this parameterisation is based on experimental measurements. These parameters neglect the highly non equilibrium carrier and lattice systems. Thus a more thorough knowledge of temperature dependence in these parameters would increase the physical accuracy of the simulations. The parameterisation of the carrier subsystem is subject to the exact same limitations as the regular two-temperature model : a temperature dependent electron-phonon coupling for most band gap materials is currently unknown and the thermal conductivity is still usually treated via a modification to the Wiedemann-Franz law [88] (which applies to metals).

$$\kappa_{e-h}(T_e) = \left(\frac{5}{2} - p\right)\left(\frac{k_B}{q}\right)^2 q\,\mu_{e-h}\,N\,T_e \tag{1.29}$$

Here κ_{e-h} is the bound electron-hole thermal conductivity, q is the charge, p is a correction factor, and μ_{e-h} is the electron-hole mobility, where $\mu_{e-h} = 1/2(\mu_e + \mu_h)$. The electron and hole mobilities of conventional semiconductor materials are well known from experiment and theory [86], however, again as in the case of swift heavy ion irradiation, the highly non equilibrium nature of the carrier and lattice subsystem mean an accurate temperature de-

pendence is currently unknown. A simple carrier mobility temperature dependence proposed by Baccarani *et al* [89] states,

$$\mu(T_e) = \mu_0 \frac{T_i}{T_e} \tag{1.30}$$

Here μ_0 is the equilibrium carrier (electron or hole) mobility at 300 K. While this continuum implementation of the extended inelastic thermal spike model has only once been applied to swift heavy ion irradiation [84], the same dynamics have been widely modelled for ultrafast laser irradiation simulations [90, 91, 92]. The initial formulation in Si [86] showed good agreement with experimental reflectivity experiments [93], while also showing that Auger recombination plays a significant role in determining the carrier concentration. It was also the first simulation to show that long lasting non equilibrium temperature distributions exist between the carrier and lattice subsystem. More recently the model has been used to explain the increase in reflectivity in GaAs following laser irradiation, which is due to band gap shrinking during electronic excitation [94]. A recent comparison between the regular TTM and the extended version have shown that thermal equilibrium takes much longer when accounting for specific carrier dynamics [90]. Recent use of the model by Zhang *et al* has also shown that increasing the laser intensity is more efficient than increasing the pulse duration in the excitation of carriers in germanium [95]. Another comparison between the regular and extended TTM was conducted by Sim *et al* [96]. Interestingly, they showed that carrier temperatures are much lower in the extended implementation, as carriers absorbing high peak intensities transfer their energy to acoustic and optical phonons almost instantaneously.

Despite the successes in the model described above, this continuum implementation still suffers from the same drawbacks as its original TTM counterpart. Namely, an inability to examine the microstructural evolution of defects within the material. Thus the next section will describe how this molecular dynamics can be incorporated into this extended two-temperature continuum formalism.

1.4.4 Extended two-temperature molecular dynamics

The creation of a hybrid extended two-temperature and molecular dynamics model follows the exact path as described previously. In this augmented continuum-atomistic approach, the lattice evolves as described by equation 1.20, with a modified frictional coefficient, γ_i.

$$\gamma_i = \gamma_{ep} = \frac{V}{N_{atoms}} \frac{mN}{\tau_{ep}} \tag{1.31}$$

V is the volume of the cell, N_{atoms} is the number of atoms in that cell, N is the carrier density, m is the mass of the atomic species, and τ_{ep} is the electron-phonon relaxation time. This atomistic-continuum hybrid has also only once been applied in the study of swift heavy ion irradiation, in Ge [83]. The ambipolar diffusivity was found to be the parameter most sensitively correlated to defect creation. It has also been sparingly used for ultrafast laser irradiation in band gap materials [97, 98, 99]. However, the ability of the model to output atomistic level detail on damage distributions, and account for processes such as superheating, volume changes and shock wave generation, mean that the model has significant benefits over its continuum analogue. Lipp *et al* [97] specifically show that the diamond structure of silicon contributes to a reduction in its stability when homogeneously melted by ultrashort laser pulses.

In summary, swift heavy ions are a particular form of radiation, which interact with materials by transferring energy to the target's electrons. Depending on the level of excitation, and the characteristic material properties, this energy transfer can eventually lead to a permanent defect rich cylindrical region perpendicular to the SHIs trajectory, known as an ion track. An in depth understanding of how these ion tracks can be controlled and manipulated has a huge range of potential engineering applications. There have been various attempts at modelling SHI irradiation (all described in this chapter), with the two-temperature model being the central model investigated within this thesis. However a number of legitimate criticisms means a modified version of the model is required when studying band gap materials. This thesis will focus on modelling swift heavy ions in both metals and band gap materials, using both the regular and extended two-temperature molecular dynamics formalisms. The next section outlines the computational techniques employed to model SHI irradiation.

2
Methodology

"Physicists like to think that all you have to do is say, these are the conditions, now what happens next?"

Richard Feynman

This chapter contains a description of the simulation techniques employed in this thesis to model swift heavy ion irradiation. The techniques can be broadly grouped into two types of atomistic simulation, classical methods and quantum mechanical methods (often referred to as *ab initio* methods). The ability to analyse swift heavy ion irradiation requires systems containing hundreds of thousands to millions of atoms, that evolve over hundreds of picoseconds, thus the ability to fully account for the electrons quantum mechanically is extremely difficult. Instead a modified version of classical molecular dynamics (MD) is employed with many of the relevant parameters derived from density functional theory (DFT), this ensures that large MD simulations are exploiting as much *ab initio* derived information as possible.

2.1 Classical Molecular Dynamics

Classical molecular dynamics is a simulation technique based on the idea that the dynamics of your system, regardless of how big and complex, can be determined by solving Newton's equation of motion for each constituent part. This involves treating the entire atom (nucleus and electrons) as an inert sphere, with the forces between them derived as follows. Consider the scenario of N interacting particles, Newton's second law takes the form,

$$\boldsymbol{F}_i(\boldsymbol{r}_1, \boldsymbol{r}_2, ..., \boldsymbol{r}_N) = m_i \frac{d^2 \boldsymbol{r}_i}{dt^2}, \qquad i = 1, 2, ..., N. \tag{2.1}$$

Here m_i is the mass, $\boldsymbol{r}_i$ is the position vector, and $\boldsymbol{F}_i$ is the force of the ith particle in the system. These forces can be derived from,

$$\boldsymbol{F}_i(\boldsymbol{r}_1, \boldsymbol{r}_2, ..., \boldsymbol{r}_N) = -\nabla_{\boldsymbol{r}_i} U(\boldsymbol{r}_1, \boldsymbol{r}_2, ..., \boldsymbol{r}_N), \tag{2.2}$$

where $U(\boldsymbol{r}_1, \boldsymbol{r}_2, ..., \boldsymbol{r}_N)$ is the potential energy function due to that configuration of particles. This potential energy function takes the form of an empirical interatomic potential in classical MD simulations, thus if an appropriate interatomic potential is chosen, accurate phase spaces of our system can be explored. There are numerous ways in which empirical potentials are derived, ranging from fitting to experimentally known quantities, to taking into account *ab initio* results.

2.1.1 Integration Schemes

Equation 2.1 yields $3N$ coupled second order differential equations, which determine how the system evolves in time. The equations are solved computationally by translating them into difference equations and applying an appropriate integrator, which should ideally fulfil a number of criteria, listed below :

(i) Time reversal invariance : this property ensures that when integrating a trajectory forward in time (with a timestep $+\Delta t$), the entire trajectory can be revisited to using $-\Delta t$.

(ii) Accuracy : it should duplicate the actual trajectory as closely as possible.

(iii) Efficient : the calculation of the forces is expensive, thus an integrator that can reliably use as large a timestep as possible while maintaining accuracy is invaluable.

(iv) Symplectic : this property ensures that the volume in phase space is preserved when moving from one configuration to another. This allows the total system energy to be conserved.

One of the most common MD integrators is the Verlet algorithm [100]. It is be derived by adding two third-order Taylor expansions for the positions, $\mathbf{r}(t)$, to each other, one forward and one backward in time t. The velocity is denoted $\mathbf{v}$, acceleration $\mathbf{a}$, and $\dot{\mathbf{a}}$ the third derivative of $\mathbf{r}$ with respect to time.

$$\mathbf{r}(t+\Delta t) = \mathbf{r}(t) + \mathbf{v}(t)\Delta t + \frac{1}{2}\mathbf{a}(t)\Delta t^2 + \frac{1}{6}\dot{\mathbf{a}}(t)\Delta t^3 + O(\Delta t^4) \tag{2.3}$$

$$\mathbf{r}(t-\Delta t) = \mathbf{r}(t) - \mathbf{v}(t)\Delta t + \frac{1}{2}\mathbf{a}(t)\Delta t^2 - \frac{1}{6}\dot{\mathbf{a}}(t)\Delta t^3 + O(\Delta t^4) \tag{2.4}$$

All terms of higher than order three are grouped into $O(\Delta t^4)$. Adding the two expressions gives,

$$\mathbf{r}(t+\Delta t) = 2\mathbf{r}(t) - \mathbf{r}(t-\Delta t) + \mathbf{a}(t)\Delta t^2 + O(\Delta t^4) \tag{2.5}$$

This is the basic form of the Verlet algorithm. The algorithm is a good integrator for Newton's laws of motion, as the third order terms actually cancel out, meaning it is an order higher in accuracy than a Taylor series expansion up to $\mathbf{a}$. This algorithm is also simple to implement, accurate and stable, and time reversible. However it also has significant drawbacks. It does not explicitly calculate velocities, which are essential for calculating the kinetic energy of our system. The velocity can be calculated from,

$$\mathbf{v}(t) = \frac{1}{2\Delta t}[\mathbf{r}(t+\Delta t) - \mathbf{r}(t-\Delta t)] + O(\Delta t^4) \tag{2.6}$$

This is far from ideal, as the positions need to be saved for three successive timesteps. The revised velocity Verlet algorithm [101] overcomes this hurdle and is summarised below.

$$\mathbf{r}(t+\Delta t) = \mathbf{r}(t) + \mathbf{v}(t)\Delta t + \frac{1}{2}\mathbf{a}(t)\Delta t^2 \tag{2.7}$$

$$\mathbf{a}(t+\Delta t) = -\frac{1}{m}\nabla U(r(t+\Delta t)) \tag{2.8}$$

$$\mathbf{v}(t+\Delta t) = \mathbf{v}(t) + \frac{1}{2}(\mathbf{a}(t) + \mathbf{a}(t+\Delta t))\Delta t \tag{2.9}$$

The positions are first updated from the previous values of position, velocity, and accel-

eration. The acceleration can then be recalculated from the potential energy function with updated position, and finally the velocity is updated. This algorithm dynamically updates in two steps, with a force calculation in between. It yields the positions, velocities, and accelerations all at the same time ($9N$ values to update for an N particle system), while maintaining all of the advantages of the original Verlet algorithm.

2.1.2 Thermostats

Integrating equation 2.1 results in the exploration of a phase space where the number of particles N, volume V, and energy E are constant. This is known as the microcanonical (NVE) ensemble. However, in reality scientific experiments are usually conducted under specific conditions of temperature and pressure, thus ensembles reflecting these conditions need to be formulated.

If the NVE ensemble is connected to a heat bath, the canonical ensemble is generated (also known as the NVT ensemble, as the number of particles, volume, and temperature T are kept constant). By controlling the pressure of the canonical ensemble the NPT ensemble is produced (also known as the isothermal-isobaric ensemble), the unit cell vectors are allowed to change, meaning this ensemble is the ideal choice for equilibration simulations, as the sample is allowed to geometrically expand or contract to find its relaxed structure. An ensemble that extends on the NPT ensemble is the NST ensemble (constant stress), which allows anisotropic deformation of the simulation cell in response to a stress. Thermostats can be broadly categorised into two types, local and global. A global thermostat acts instantaneously and equally on all the particles in a simulation. A description of two global commonly used thermostat follows.

2.1.2.1 Berensden thermostat & barostat

The simplest way to maintain a constant temperature in an MD simulation is to rescale the velocities of each particle at each timestep. However, this completely fixes the temperature of your system (allowing no fluctuations), which also constrains the kinetic energy of your system, and thus only a limited portion of the true canonical ensemble is explored. A modification of this velocity rescaling method was formulated by Berensden [102], which allowed for more realistic temperature fluctuations. The idea now is that the velocities are

rescaled at each step so that,

$$\frac{dT}{dt} = \frac{1}{\tau_T}(T_0 - T) \tag{2.10}$$

where T is the temperature, t is the time, T_0 is the target temperature, and τ_T is the strength of the thermostat coupling. This results in a velocity rescaling factor,

$$\chi = \left[1 + \frac{\Delta t}{\tau_T}\left(\frac{T_0}{T} - 1\right)\right]^{1/2} \tag{2.11}$$

where χ is the rescaling factor, and Δt is the timestep. The empirical choice of τ_T is extremely important as it has a considerable effect on the phase space explored. As $\tau_T \to \infty$ the thermostat becomes inactive, $\tau_T \to 0$ results in unrealistically low temperature fluctuations, and $\tau_T = \Delta t$ is the same result as simple velocity rescaling. Berensden also proposed a similar way to control the pressure of an MD simulation,

$$\frac{dP}{dt} = \frac{1}{\tau_P}(P_0 - P) \tag{2.12}$$

where P is pressure, P_0 is the target pressure, and τ_P is the strength of the barostat coupling, which similarly rescales the MD box volume by,

$$\chi = 1 - \beta_T \frac{\Delta t}{\tau_P}(P_0 - P) \tag{2.13}$$

where β_T is the isothermal compressibility and the positions are rescaled by $\chi^{1/3}$. This thermostat and barostat also suffers from an inability to sample the true canonical ensemble, which leads to the question of why use it at all? Although it is not recommended to use this as your final thermostat in MD simulations, it is an extremely fast and efficient way to thermostat a system that is far from equilibrium, once it has reached the desired temperature and pressure, a more physically accurate algorithm can be employed.

2.1.2.2 Nosé-Hoover thermostat & barostat

A method for globally thermostating an MD system which also leads to a physically real canonical distribution was proposed by Nosé and Hoover[103, 104]. This is achieved by adding a virtual degree of freedom to the system, which simulates the influence of a heat

bath on the physical degrees of freedom. The entire system (including the virtual degree of freedom) samples the micro-canonical ensemble, allowing the real degrees of freedom to sample the true canonical ensemble. The modified equation of motion takes the form,

$$\frac{d\mathbf{v}}{dt} = \frac{\mathbf{F}(t)}{m} - \chi(t)\mathbf{v}(t) \tag{2.14}$$

The thermostat friction coefficient, χ, is controlled by the first order differential equation,

$$\frac{d\chi(t)}{dt} = \frac{1}{Q_T}\Big[mv^2 - gk_BT_0\Big] \tag{2.15}$$

$$Q_T = gk_BT_0\tau_T^2 \tag{2.16}$$

where Q_T is the thermostatting mass, g is the number of real degrees of freedom in the system, τ_T is the strength of thermostat coupling, and T_0 is the target temperature. The term in brackets in equation 2.15 shows that the strength of the friction term is proportional to the difference between the instantaneous kinetic energy $(1/2)mv^2$ and the average kinetic energy $(3N/2)k_BT$. A choice of large Q_T (corresponding to weak coupling) can lead to poor temperature control, as well as increased simulation times before equilibrium is reached. Small Q_T values lead to larger amplitudes of the temperature fluctuation.

The equations of motion for Nosé-Hoover barostat are fomulated similarly. Another virtual degree of freedom corresponding to an isotropic piston acting on the system is added to the equations of motion.

$$\frac{d\mathbf{v}}{dt} = \frac{\mathbf{F}(t)}{m} - [\chi(t) + \eta(t)]\mathbf{v}(t) \tag{2.17}$$

$$\frac{d\eta(\mathbf{t})}{dt} = \frac{1}{Q_P}V(t)[P - P_0] \tag{2.18}$$

$$Q_P = gk_BT_0\tau_P^2 \tag{2.19}$$

$$\frac{dV(t)}{dt} = 3\eta(t)V(t) \tag{2.20}$$

Here η is the barostat friction coefficient, Q_P is the barostat mass, V is the volume of the cell, P the pressure, P_0 the target pressure, and τ_P the barostat coupling strength. The barostat mass suffers from the same behaviour described previously for thermostat mass. Although this algorithm allows for sampling of the canonical ensemble, it can be unstable if the system under study is far from equilibrium.

2.1.3 Interatomic potentials

As mentioned previously, the validity of the physical interactions in an MD simulation are determined by the interatomic potential, $U(\boldsymbol{r}_1, \boldsymbol{r}_2, ..., \boldsymbol{r}_N)$, which describes how the potential energy of a system of N atoms varies depending on co-ordinates $\boldsymbol{r}_1, \boldsymbol{r}_2, ..., \boldsymbol{r}_N$. The atomic motions are considered by Taylor expanding the potential energy function in terms of 1-body, 2-body,..., N-body terms,

$$U(\boldsymbol{r}_1, \boldsymbol{r}_2, ..., \boldsymbol{r}_N) = \sum_{i=1}^{N} V_i(r_j) + \sum_{i=1}^{N} \sum_{j \neq i}^{N} V_{ij}(r_{ij}) + \sum_{i=1}^{N} \sum_{j \neq i,k}^{N} \sum_{k \neq i,j}^{N} V_{ijk}(r_i, r_j, r_k) + ..., \quad (2.21)$$

where the V_i is the one body contribution (usually zero unless there is an external field present). V_{ij} is the two body contribution, which in some cases is enough to approximate $U(\mathbf{r_1}, \mathbf{r_2}, ..., \mathbf{r_n})$ alone, r_{ij} is the distance between the ith and jth atom. V_{ijk} is the three body contribution, which is determined by the spatial location of each constituent particle, r_i, r_j, and r_k.

The forces are evaluated via equation 2.2, and this step is by far the most computationally expensive. This leads to an inherent trade-off between the detail of the encapsulated physics and the simulations time and length scales. Interatomic potentials are generated in a number of ways, depending on where on this trade-off continuum one wishes to lie. Given a functional form one can choose parameters that reproduce experimentally measured quantities, or one can quantum mechanically solve the equations of motion for a given configuration of particles, and then generate a functional form from this. We utilise both types of potentials, but the latter model is sometimes preferred as it increases transferability, which is the ability of a potential to accurately reproduce physical quantities that weren't explicitly parameterised.

This thesis investigates the study of both metallic and band gap systems, with the relevant interatomic potentials described below.

2.1.3.1 Extended Finnis-Sinclair potential

Traditionally atomistic simulations employed empirical pair potentials. This posed significant hurdles in the case of metallic systems, as only 10% of the experimentally known cohesive energies could be accounted for. The remainder is contained in density dependent, geometry independent energy. This problem was overcome with the Finnis-Sinclair potential [105], via the addition of an attractive density dependent term derived from a second moment approximation of the tight-binding density of states. This also had its shortcomings, however, as certain equilibrium properties of fcc metals were badly reproduced.

The extended Finnis-Sinclair potential [106] successfully remedied these problems and is capable of accurately modelling fcc metals, bcc metals, and alloys. The potential energy takes the form,

$$U(\mathbf{r_1}, \mathbf{r_2}, \ldots, \mathbf{r_N}) = \frac{1}{2}\sum_{i=1}^{N}\sum_{j\neq i}^{N} V_{ij}(r_{ij}) + \sum_{i=1}^{N} F(\rho_i) \quad , \tag{2.22}$$

where $F(\rho_i)$ is a functional describing the energy of embedding an atom, i, in electronic density, ρ_i.

$$\rho_i = \sum_{i=1, j\neq i}^{N} \phi(r_{ij}) \quad . \tag{2.23}$$

Here $\phi(r_{ij})$ is the electronic charge density on atom i by j. The repulsive interactions between atoms is described by

$$V_{ij}(r_{ij}) \quad = \quad \begin{cases} (r_{ij}-c)^2(c_0 + c_1 r_{ij} + c_2 r_{ij}^2 + c_3 r_{ij}^3 + c_4 r_{ij}^4) & : \quad r_{ij} < c \\ 0 & : \quad r_{ij} > c, \end{cases} \tag{2.24}$$

Here c is a cut-off between the second and third nearest neighbours and c_1, c_2, c_3, and c_4 are fitted material dependent parameters. The r_{ij}^3 and r_{ij}^4 terms were added to the new parameterisation as the original potential underestimated the repulsive forces at extended

lengths. The embedding function F is expressed,

$$F(\rho_i) \;=\; A\sqrt{\rho_i} \;\;, \tag{2.25}$$

where A is another potential parameter, and the linear superposition of the each atoms electron density function is calculated by,

$$\phi(r_{ij}) \;=\; \begin{cases} (r_{ij}-d)^2 + B^2(r_{ij}-d)^4 & : \quad r_{ij} < d \\ 0 & : \quad r_{ij} > d. \end{cases} \tag{2.26}$$

$$\tag{2.27}$$

d again is cut-off taken to be between the second and third nearest neighbour distance. B is the parameter added to the original potential to allow for the more accurate treatment of fcc metals and bcc-fcc alloy systems.

2.1.3.2 Tersoff Potential

Tetrahedral semiconductors are even more difficult to empirically parameterise than metals. This is due to the open diamond structure, coupled with the fact that the liquid phase is more dense than the solid phase. One of the most successful attempts at generating an interatomic potential for silicon was achieved by Tersoff [107], based on work by G. Abell [108], which fundamentally parameterised chemical potentials using LCAO (linear combination of atomic orbital) theory (and thus is classified as a semi-empirical potential).

The Tersoff potential describes covalent systems, and abandons the N-body form of equation 2.21, instead coupling two and higher body contributions into one functional form, with a bond order term included as an angular term. This is ideal for simulating covalent systems as the electrons are localized between the atoms, so covalent bonds have a strong directional dependence. Therefore, the energy of such a system is not simply dependent on the distances between the atoms but also on the angles. It reproduces covalent systems by realistically simulating the interaction environment, so the more neighbours an atom bonds with, the weaker each bond will be. The potential energy can be written as,

$$U(\mathbf{r_1}, \mathbf{r_2}, \ldots, \mathbf{r_N}) = \sum_{i=1}^{N} \sum_{j \neq i}^{N} \sum_{k \neq j}^{N} U_{Tersoff}(i, j, k, \mathbf{r_i}, \mathbf{r_j}, \mathbf{r_k}) = \frac{1}{2} \sum_{i \neq j} U_{ij}, \tag{2.28}$$

$$\tag{2.29}$$

where the indices i, j, k indicate the atoms involved in the intermolecular interactions, and $\mathbf{r_i}, \mathbf{r_j}, \mathbf{r_k}$ are the position vectors of the specific atoms involved in a given interaction. The potential energy function is,

$$U_{ij} = f_C(r_{ij}) \left[f_R(r_{ij}) - \gamma_{ij} \; f_A(r_{ij}) \right] \quad , \tag{2.30}$$

where f_R and f_A are the repulsive and attractive pair potential terms respectively:

$$f_R(r_{ij}) = A_{ij} \; \exp(-a_{ij} \; r_{ij}) \quad , \quad f_A(r_{ij}) = B_{ij} \; \exp(-b_{ij} \; r_{ij}) \tag{2.31}$$

The energy of each atom is governed by $f_C(r)$, a smooth cut-off function, which reduces the magnitude of the potential between R_{ij} and S_{ij}. The form of the cut-off function is,

$$f_C(r_{ij}) = \begin{cases} 1 & : \quad r_{ij} < R_{ij} \\ \frac{1}{2} + \frac{1}{2} \cos \left[\pi \; \frac{r_{ij} - R_{ij}}{S_{ij} - R_{ij}} \right] & : \quad R_{ij} < r_{ij} < S_{ij} \\ 0 & : \quad r_{ij} > S_{ij} \end{cases} \tag{2.32}$$

γ_{ij} expresses a dependence that can increase or decrease the attractive component of the force relative to the repulsive component, according to the local environment,

$$\gamma_{ij} \;\; = \;\; (1 + \mathcal{L}_{ij}^{\eta_i})^{-\delta_i} \tag{2.33}$$

$$\mathcal{L}_{ij} \;\; = \;\; \sum_{k \neq i,j} f_C(r_{ik}) \; g(\theta_{ijk}) \; \overbrace{\exp \left[\alpha_i (r_{ij} - r_{ik})^{\beta_i} \right]}^{\omega_{ik}} \tag{2.34}$$

Here $\mathcal{L}$ is the effective co-ordination number (no. of nearest neighbours) of atom i, taking

into account the relative distances of neighbours j, and k. The exponential is a term whose strength depends on the difference in bond length of ij and ik. The value for this ω_{ik} describes the behaviour of the material far from equilibrium, and can be taken to be a constant (= 1) in silicon, which greatly simplifies the implementation of the potential.

$$g(\theta_{ijk}) \;=\; 1 + \frac{c_i^2}{d_i^2} - \frac{c_i^2}{d_i^2 + (h_i - \cos\theta_{ijk})^2} \tag{2.35}$$

$g(\theta_{ijk})$ is the angular term dependent on the angle between ij and jk bonds, with constants c and d determining the strength of the overall angular dependence. Tersoff was unable to find a parameter set that successfully predicted both the elastic and surface properties of Si simultaneously, thus two parameter sets exist, the T2 parametrisation of surface properties, and the T3 parameterisation of elastic behaviour. However, despite these faults it still remains one of the most widely used potentials for silicon.

2.1.3.3 Modified Tersoff Potential

The modified Tersoff potential was developed in 2007 by T. Kumagai *et al.* [109], after it proved impossible to accurately reproduce both elastic constants and melting properties simultaneously with the original Tersoff functional form. To reproduce both of these properties, the functional form of the Tersoff was modified as follows,

$$f_C(r_{ij}) = \begin{cases} 1 & : \quad r_{ij} < R_{ij} \\ \frac{1}{2} + \frac{9}{16}\cos\left[\pi\,\frac{r_{ij}-R_{ij}}{S_{ij}-R_{ij}}\right] - \frac{1}{16}\cos\left[3\pi\,\frac{r_{ij}-R_{ij}}{S_{ij}-R_{ij}}\right] & : \quad R_{ij} < r_{ij} < S_{ij} \\ 0 & : \quad r_{ij} > S_{ij} \quad . \end{cases} \tag{2.36}$$

The cut-off function was modified so it has continuous second order derivatives.

$$\gamma_{ij} \;=\; (1 + \mathcal{L}_{ij}^{\eta_i})^{-\delta_i} \tag{2.37}$$

$$\mathcal{L}_{ij} \;=\; \sum_{k \neq i,j} f_C(r_{ik})\; g(\theta_{ijk})\; \overbrace{\exp\left[\alpha_i (r_{ij} - r_{ik})^{\beta_i}\right]}^{\omega_{ik}} \tag{2.38}$$

Here γ_{ij} and $\mathcal{L}_{ij}$ have the same meaning and form, but in the modified Tersoff the ω_{ik} term, which describes the system far from equilibrium, is not taken to be a constant.

$$\begin{aligned} g(\theta_{ijk}) &= c_{1i} + g_o(\theta_{ijk})\ g_a(\theta_{ijk}) \\ g_o(\theta_{ijk}) &= \frac{c_{2i}\ (h_i - \cos\theta_{ijk})^2}{c_{3i} + (h_i - \cos\theta_{ijk})^2} \\ g_a(\theta_{ijk}) &= 1 + c_{4i}\ \exp\left[-c_{5i}\ (h_i - \cos\theta_{ijk})^2\right]\ , \end{aligned} \tag{2.39}$$

The potential accurately reproduces both the elastic constants and melting point of diamond Si, and the new angular dependent term $g(\theta_{ijk})$ is the most significant contributor in reproducing the correct melting temperature.

2.1.4 Periodic Boundary Conditions

The entirety of this thesis focuses on SHI irradiation in bulk materials. A macroscopic volume contains $\sim 10^{23}$ particles, so when doing MD simulations of $\sim 10^6$ particles, one must be careful not to disproportionately account for surface effects. The use of periodic boundary conditions (PBC) ensures that results from smaller MD simulations can be analogously compared to macroscopic behaviours. Figure 2.1 shows a schematic of PBCs in a typical MD simulation.

The original MD cell (on the left) is surrounded by infinitely many identical 'virtual' images in each dimension (on the right). As the simulation proceeds, each cell evolves identically, so any particle that leaves a boundary of the original cell re-enters from the opposing side. This is not complication free however, as a particle may interact with both a nearby particle, and its corresponding image in the neighbouring virtual system. This is overcome by ignoring interactions with particles beyond a certain cut-off radius, r_{cut}, thereby bounding r_{cut} to less than half the simulation cell length.

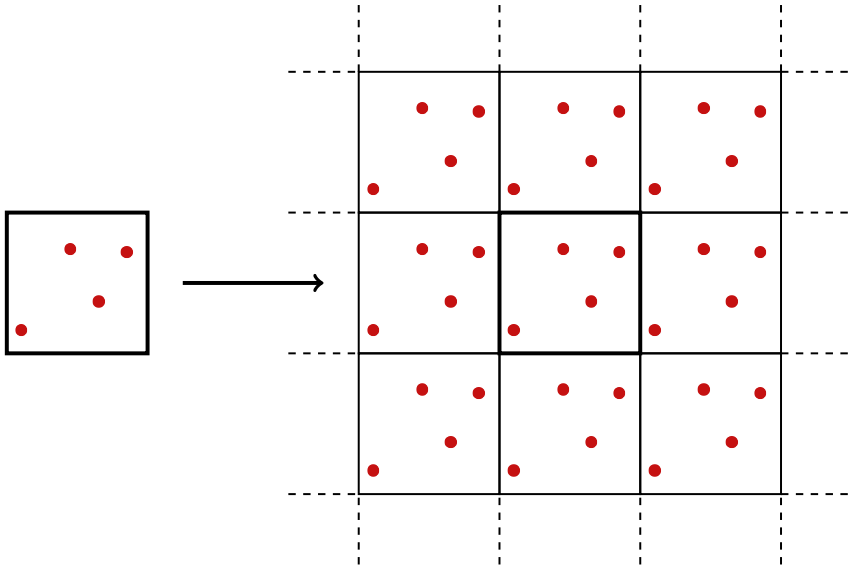

Figure 2.1: Periodic boundary conditions in a typical MD simulation. Left : actual simulation cell. Right : 2D periodic boundary conditions surrounding the original simulation cell.

2.2 Two-Temperature Molecular Dynamics

Classical molecular dynamics is a simulation method which is incapable of explicitly treating the electrons in a material, and as SHI irradiation primarily results in electronic excitation, modifications are required to encompass these processes. Two-temperature molecular dynamics (2T-MD) is an augmented version of classical MD which can simulate this highly excited electronic system. The premise is based on treating the electrons and atoms as two separate, but interacting, subsystems. The temperature of the electrons evolve according to a heat diffusion equation (solved via finite difference methods), and the atoms positions evolve according to a modified version of classical MD, with energy being exchanged while the systems are out of thermal equilibrium with each other.

2.2.1 Finite Difference Method

The electronic temperature is treated as a continuum system, surrounding the MD cell, and evolves according to Fourier's law of heat conduction,

$$C_e(T_e)\frac{\partial T_e}{\partial t} - \nabla.[\kappa_e \nabla T_e] = -G(T_e - T_i) + A(r,t), \tag{2.40}$$

$C_e(T_e)$ is the electronic specific heat capacity, κ_e is the electronic thermal conductivity, G is the electron phonon coupling, and $A(r,t)$ is the temporal and spatial dependent source term. This equation describes how energy evolves in the electronic system as follows : the SHI transfers energy into the centre of the material via the source term, the electronic specific heat determines the electronic temperature (T_e) rise due to this deposition, the thermal conductivity describes how energy dissipates throughout the electronic subsystem, and the electron-phonon coupling determines energy transfer from the electrons to the ions (and is proportional to the temperature difference between the T_e and the lattice temperature (T_i)). Equation 2.40 can be equated to the more general heat diffusion equation,

$$\frac{\partial T}{\partial t} - \alpha \nabla^2 T = \frac{\dot{q}}{C}, \tag{2.41}$$

T is temperature, t is time, $\dot{q}$ is a heat source or sink, C is specific heat, and α is thermal diffusivity. This partial differential equation is solved using Euler's method, which a space-centred, forward in time integration algorithm. For a temperature T_i^n (at time step n, and of grid point i) the forward in time implementation can be Taylor expanded and rearranged to,

$$\left(\frac{\partial T}{\partial t}\right)_i = \frac{T_{i+1}^n - T_i^n}{\Delta t} - \frac{\Delta t}{2}\left(\frac{\partial^2 T}{\partial t^2}\right)_i - \frac{\Delta t^2}{6}\left(\frac{\partial^3 T}{\partial t^3}\right)_i - \dots \approx \frac{T_{i+1}^n - T_i^n}{\Delta t}, \tag{2.42}$$

for equally space timesteps Δt, and leads to a truncation error $O(\Delta t)$. The space-centred integration is the forward difference and backward difference added together,

$$Forward : \left(\frac{\partial T}{\partial x}\right)_n = \frac{T_{i+1}^n - T_i^n}{\Delta x} - \frac{\Delta x}{2}\left(\frac{\partial^2 T}{\partial x^2}\right)_i - \frac{\Delta x^2}{6}\left(\frac{\partial^3 T}{\partial x^3}\right)_i - \dots, \tag{2.43}$$

$$Backward: \left(\frac{\partial T}{\partial x}\right)_n = \frac{T_i^n - T_{i-1}^n}{\Delta x} + \frac{\Delta x}{2}\left(\frac{\partial^2 T}{\partial x^2}\right)_i - \frac{\Delta x^2}{6}\left(\frac{\partial^3 T}{\partial x^3}\right)_i + \ldots, \tag{2.44}$$

$$Central: \left(\frac{\partial T}{\partial x}\right)_n = \frac{T_{i+1}^n - T_{i-1}^n}{\Delta x} - \frac{\Delta x^2}{6}\left(\frac{\partial^3 T}{\partial x^3}\right)_i - ... \approx \frac{T_i^{n+1} - T_i^{n-1}}{\Delta x} \tag{2.45}$$

for equally spaced grid lengths Δx, and leads to a truncation error of $O(\Delta t^2)$. The second derivative is calculated as follows,

$$\left(\frac{\partial^2 T}{\partial x^2}\right)_n = \left[\frac{\partial}{\partial x}\frac{\partial T}{\partial x}\right]_n = \lim_{\Delta x \to 0} \frac{\text{forward difference - negative difference}}{\Delta x} \tag{2.46}$$

$$\left(\frac{\partial^2 T}{\partial x^2}\right)_n \approx \frac{\frac{T_{i+1}^n - T_i^n}{\Delta x} - \frac{T_i^n - T_{i-1}^n}{\Delta x}}{\Delta x} = \frac{T_{i+1}^n - 2T_i^n + T_{i-1}^n}{\Delta x^2} \tag{2.47}$$

Inserting these numerical solutions into equation 2.41, the one dimensional heat diffusion equation can be expressed via a finite difference scheme as,

$$\frac{T_i^{n+1} - T_i^n}{\Delta t} - \alpha \frac{T_{i+1}^n - 2T_i^n + T_{i-1}^n}{\Delta x^2} = \frac{\dot{q}}{C}. \tag{2.48}$$

Rearranging for T_i^{n+1} gives,

$$T_i^{n+1} = T_i^n + \Delta t\left[\alpha \frac{T_{i+1}^n - 2T_i^n + T_{i-1}^n}{\Delta x^2} + \frac{\dot{q}}{C}\right], \tag{2.49}$$

which is also known as the 1-D explicit finite difference solution to Fourier's law of heat conduction and is illustrated in figure 2.2 . It is explicit as the temperature at time n+1 *explicitly* depends on the temperature at time n. The forward in time, space-centred nature of the algorithm is evident in figure 2.2.

Δt and Δx must be chosen carefully to ensure the stability of this algorithm, and this is provided by defining the Fourier mesh number, F, as,

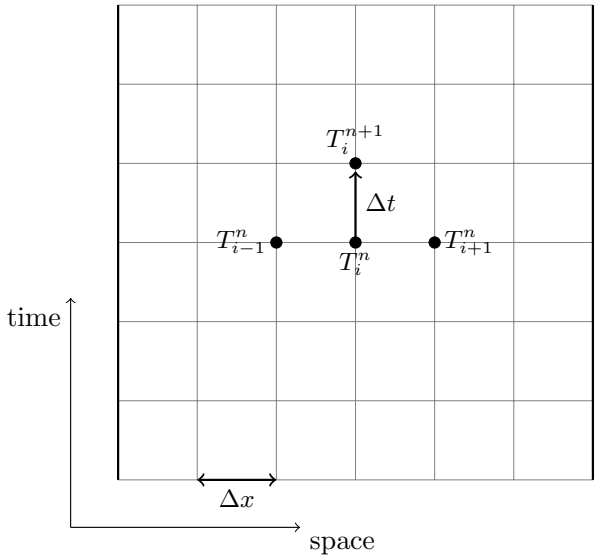

Figure 2.2: 1-D (spatial) finite difference schematic. The algorithm is constrained to forward in time movement, but varies in both spatial directions. The dark vertical lines at the edge of the schematic are the boundary nodes.

$$F = \alpha \frac{\Delta t}{\Delta x^2} \tag{2.50}$$

This can be thought of as the ratio of timestep to the time it takes to equilibrate a region of length Δx, and in this 1-D case must satisfy $0 < F < \frac{1}{2}$, or else the algorithm becomes unstable and oscillates wildly. The algorithm can be expanded to 3-D as follows,

$$T_{i,j,k}^{n+1} = T_{i,j,k}^n + \Delta t \left[\alpha \frac{T_{i+1,j,k}^n + T_{i-1,j,k}^n + T_{i,j+1,k}^n + T_{i,j-1,k}^n + T_{i,j,k+1}^n + T_{i-1,j,k-1}^n - 6T_{i,j,k}^n}{\Delta x^2} + \frac{\dot{q}}{C} \right], \tag{2.51}$$

$$T_{i,j,k}^{n+1} = T_{i,j,k}^n + F[T_{i+1,j,k}^n + T_{i-1,j,k}^n + T_{i,j+1,k}^n + T_{i,j-1,k}^n + T_{i,j,k+1}^n + T_{i-1,j,k-1}^n - 6T_{i,j,k}^n] + \Delta t \frac{\dot{q}}{C}, \tag{2.52}$$

with new a new stability criteria of $0 < F < \frac{1}{6}$. Thus the size of the timestep must satisfy $\Delta t < \frac{\Delta x^2}{6\alpha}$. Equation 2.52 applies under the assumption that $\nabla.[\alpha \nabla T] = \alpha \nabla^2 T$, but the

more general (and hence more complicated) case, where α can vary spatially, takes the form,

$$T_{i,j,k}^{n+1} = \frac{\Delta t}{\Delta x^2} \frac{\kappa\left[\frac{1}{2}(T_{i+1,j,k}^{n} + T_{i,j,k}^{n})\right]}{C(T_{i,j,k}^{n})}(T_{i+1,j,k}^{n} - T_{i,j,k}^{n}) + \frac{\Delta t}{\Delta x^2} \frac{\kappa\left[\frac{1}{2}(T_{i-1,j,k}^{n} + T_{i,j,k}^{n})\right]}{C(T_{i,j,k}^{n})}(T_{i-1,j,k}^{n} - T_{i,j,k}^{n}) + \cdots + \Delta t \frac{\dot{q_{i,j,k}^{n}}}{C_{i,j,k}^{n}} \quad (2.53)$$

Here the electronic thermal conductivity has an explicit spatial dependence. To simplify this relationship, κ is assumed to be constant locally, and is taken to be the average value between the current and neighbouring cells. An adaptive timestep is also utilised, so at each timestep the 'worst case scenario' for the Fourier mesh number, F, is chosen, ensuring the stability of the electronic subsystem.

2.2.1.1 Electronic Boundary Conditions

Various boundary condition choices are available for the edge cells in figure 2.2. In our simulations the edge cells surround the simulation in all three spatial dimensions. These boundary conditions are;

- Dirichlet Boundary Conditions : Also known as infinite flux boundary conditions, here the edge cell is fixed at a finite temperature, $T = T_0$, where T_0 is the target temperature.
- Neumann Boundary Conditions : Also known as zero flux boundary conditions, here the temperature of the edge cell is taken to be the value at the corresponding neighbour, thus $\frac{dT}{dt} = 0$ in this region.
- Robin Boundary Conditions : Also known as partial or variable flux boundary conditions, here the temperature of the edge cell is taken to be a fixed proportion of the neighbouring cell's temperature. Thus $\frac{dT}{dt} = -k(T - T_0) + T_0$, where k is the fraction of the neighbouring temperature that is 'targeted'.

A typical approach when simulating SHI irradiation in a new material is to initially use Neumann BCs. This allows the system to be tested for energy conservation and algorithm

stability. When this is verified the more physically realistic Robin BCs are chosen, as these conditions simulate energy dissipation into bulk materials.

2.2.2 Inhomogeneous Langevin Thermostat

In 2T-MD, the electrons and ions are split up into two separate subsystems. This section will describe how the ions (also called atoms, lattice, or nuclei) are treated within the 2T-MD model, and is a method derived by D. Duffy and A. Rutherford [76]. The principal idea is to modify the MD equations of motion according to Langevin dynamics, which describes the movement of particles in a viscous medium. This viscous medium will represent the electronic subsystem, and the modified equation of motion takes the form,

$$m_i \frac{\partial \mathbf{v}_i}{\partial t} = \mathbf{F}_i(t) - \gamma_i \mathbf{v}_i + \tilde{\mathbf{F}}_i(t), \tag{2.54}$$

where m_i and $\mathbf{v}_i$ are the mass and velocity of atom i at time t,

- $\mathbf{F}_i(t)$ is the deterministic force on i due to the interatomic potential.
- $\gamma_i \mathbf{v}_i$ is the frictional force due to the electrons.
- $\tilde{\mathbf{F}}_i(t)$ is a stochastic force with random magnitude and orientation.

Thus the last two terms on the right of equation 2.54, which are the Langevin modifications to Newton's second law, allow energy to be lost and gained by the MD system. $\tilde{\mathbf{F}}_i(t)$ is a stochastic force which returns energy from the electrons to the ions. It is formulated as follows, $\tilde{\mathbf{F}}_i(t) = \sqrt{\Gamma}\tilde{\mathbf{A}}_i(t)$, where $\tilde{\mathbf{A}}_i(t)$ is a three dimensional vector with components randomly distributed in $[-1, 1]$. Γ is the stochastic friction coefficient, and will be described in more detail later. $\tilde{\mathbf{F}}_i(t)$ must satisfy two important time-averaged conditions ;

$$\langle \tilde{\mathbf{F}}_i(t) \rangle = 0, \tag{2.55}$$

$$\langle \tilde{\mathbf{F}}_i(t) \cdot \tilde{\mathbf{F}}_j(t') \rangle \propto \delta_{ij}\delta(t - t') \tag{2.56}$$

The first states that over a significant period of time, $\tilde{\mathbf{F}}_i(t)$ must not behave as a net source or sink. Equation 2.56 is known as the fluctuation-dissipation theorem, which describes how

the drag felt by a particle as it moves through a viscous medium can give rise to Brownian motion. In the standard homogeneous Langevin thermostat every atom in the MD simulation is thermostatted to a target temperature, the inhomogeneous case allows for each atom to be thermostatted to the electronic temperature of the corresponding continuum electronic cell. This leads to the stochastic friction term,

$$\Gamma = \frac{6\gamma_{ep}^{j} k_B T_e^{j}}{\Delta t}, \tag{2.57}$$

Where γ_{ep}^{j} is the electron-phonon friction of the j^{th} electronic finite element cell, T_e^{j} is the electronic temperature of the corresponding cell, k_B is Boltzmann's constant, and Δt is the timestep. The electron-phonon friction term can be calculated at each point in the finite electronic temperature grid using,

$$\gamma_{ep} = \frac{VmG_{ep}}{3k_B N}, \tag{2.58}$$

Here, V is the volume of the cell, m is the mass of the atomic species, G_{ep} is the electron-phonon coupling constant of the material, and N is the number of atoms in the cell. Thus as the size of the grid gets larger, N also increases, reducing γ_{ep}. The friction term in equation 2.54 is made up of two forms of energy loss, the electron-phonon friction which has just been discussed, and electronic stopping, which is inelastic electron scattering of ballistic atoms.

$$\begin{aligned} \gamma_i &= \gamma_{ep} + \gamma_{es} \quad \text{for } v_i > v_{cut}, \\ \gamma_i &= \gamma_{ep} \qquad\quad \text{for } v_i \leq v_{cut}, \end{aligned} \tag{2.59}$$

Here γ_i is the total electron friction coefficient, γ_{es} is the electronic stopping friction, v_i is the velocity, and v_{cut} is the cut-off velocity for which electronic stopping becomes significant. From equations 2.54 and 2.58 the difference between the contributions from electron-phonon coupling and electronic stopping are evident. Electron-phonon coupling allows energy to flow from to and from the lattice (depending on the temperature gradient between the lattice and electrons), whereas electronic stopping is only an energy loss mechanism for the lattice.

Figure 2.3 illustrates these processes, and highlights how the MD cell is now indirectly thermostatted to a heat bath. The lattice will reach local equilibrium with the electrons, which are thermostatted to the heat bath, thus eventually driving both subsystems to the chosen ambient temperature. Energy can only be removed from the system through the electrons. This is justified as lattice heat diffusion is extremely slow in comparison to electronic heat diffusion.

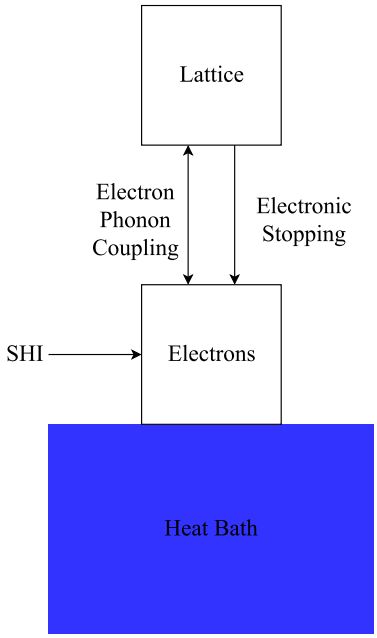

Figure 2.3: Schematic of the thermodynamic coupling and processes in 2T-MD model

2.2.3 Simulation Setup

The schematic for a SHI simulation using this 2T-MD implementation is shown in figure 2.4. The electronic subsystem is divided into a number of coarse grained electronic temperatue cells (which will be referred to as CETs), and the MD cell is divided up into coarse grained ionic temperature cells (CITs).

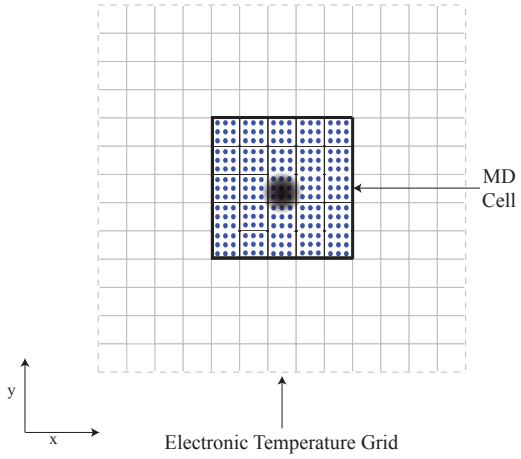

(a) Top View

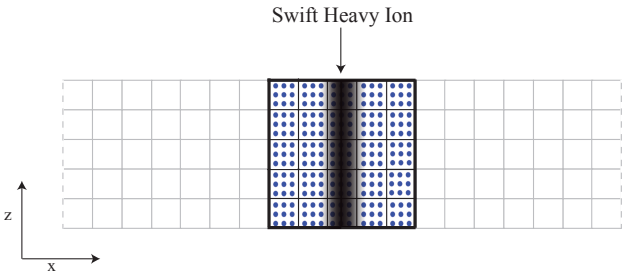

(b) Side View

Figure 2.4: Schematic of the 2T-MD simulation setup for swift heavy ion irradiation. The grey boxes are CETs, the black boxes are the CITs, Robin boundary conditions are represented by the dashed grey line, and the periodic boundary conditions of the MD by the thick black line. The swift heavy ion travels perpendicular to the page in figure 2.4a, and vertically through the cell in figure 2.4b

.

The volume of each of these cells is roughly 1000 $\dot{A}^3$. The number of CETs extends far beyond the MD cell in the xy direction, which ensures the boundary conditions imposed on the electronic system does not drive the temperature in the simulation artificially. The number of CET = CIT in the z-direction, and the simulation is setup so that all the atoms

in a given CIT are assigned the electronic temperature of the overlapping CET. Energy deposited into the electronic system is represented by a Gaussian distribution in space, and exponentially decaying in time. More accurate distributions based on work by Waligorski [73] have been proposed, but are beyond the scope of this thesis.

2.3 Extended Two-Temperature Molecular Dynamics

A key criticism levelled at the 2T-MD model is its validity when applied band gap materials. The model was developed for metals, and its application to band gap materials is based on the assumption that hot electrons in a band gap material behave the same way as electrons in a metal. The extended inelastic thermal spike (eiTS) model was developed specifically to account for band gap processes (such a carrier generation and recombination), and the extended two-temperature molecular dynamics model is the implementation of the eiTS that is explored in this thesis. The basic idea remains the same, in that an augmented continuum-atomistic approach is utilised, where the electrons, or in this case electron-hole pairs, and the lattice are split into two separate interacting subsystems. The model is described in the background section of this thesis. A description of the more complicated finite difference solver follows.

2.3.1 Carrier finite difference solver

Due to the presence of an extra conservation equation, the finite difference solver for the extended 2T-MD is significantly more complicated than the regular version. Equations 1.21 and 1.24 are rewritten as follows :

$$\begin{aligned} \frac{\partial N}{\partial t} &- \nabla \cdot \left[D(T_i) \nabla N \right] \\ &- \nabla \cdot \left[D(T_i) \left(\frac{2N}{k_B T_e} \right) \nabla E_g \right] \\ &- \nabla \cdot \left[D(T_i) \left(\frac{N}{2T_e} \right) \nabla T_e \right] \\ &= G_{e-h} - R_{e-h} \end{aligned} \tag{2.60}$$

$$
\begin{aligned}
\frac{\partial U}{\partial t} &- \nabla \cdot \big[(E_g + 4k_B T_e)J\big] \\
&+ \nabla \cdot \big[(\nabla\kappa_e + \nabla\kappa_h)\nabla T_e\big] \\
&= -\frac{C_{e-h}}{\tau_{ep}}(T_e - T_i) + A(r[v_{ion}], t) \\
\implies \frac{\partial U}{\partial t} &+ \nabla\big[D(T_i)(E_g + 4k_B T_e)\nabla N\big] \\
&+ \nabla \cdot \left[D(T_i)(E_g + 4k_B T_e)\left(\frac{2N}{k_B T_e}\right)\nabla E_g\right] \\
&+ \nabla \cdot \left[D(T_i)(E_g + 4k_B T_e)\left(\frac{N}{2T_e}\right)\nabla T_e\right] \\
&+ \nabla \cdot \big[(\nabla\kappa_e + \nabla\kappa_h)\nabla T_e\big] \\
&= -\frac{C_{e-h}}{\tau_{ep}}(T_e - T_i) + A(r[v_{ion}], t)
\end{aligned}
\tag{2.61}
$$

In this form, equations 2.60 and 2.61 are computationally solved via Euler's method for each individual component (∇N, ∇E_g, ∇T_e, etc), with the summation yielding the final solution. It is important to stress that this model explicitly tracks the carrier concentration N and carrier energy U. The carrier temperature T_e is calculated from equation 1.23.

2.4 T_e - dependent interatomic potentials

The vast majority of MD simulations that explore electronic excitation assume that the ground state interatomic potential remains valid regardless of how 'hot' the electrons are. The main reason for this assumption is due to the difficulty in developing T_e dependent interatomic potentials. In this thesis the contribution of these T_e dependent potentials is explored for two different systems, tungsten and silicon. The physical basis for these potentials is that the bonding characteristics of material change significantly in regions of high electronic excitation, which was discussed previously by the bond weakening model.

2.4.1 Tungsten

The most commonly used interatomic potentials for tungsten adopt the embedded atom model (EAM), of which the extended Finnis-Sinclair is a particular example (and described in section 2.1.3.1). The potential energy, U of such an N atom system is described by,

$$U = \frac{1}{2}\sum_{i=1}^{N}\sum_{j\neq i}^{N} V_{ij}(r_{ij}) + \sum_{i=1}^{N} F(\rho_i) \tag{2.62}$$

V_{ij} is the pair repulsion between atoms i and j. $F(\rho_i)$ is a functional describing the energy of embedding an atom, i, in electronic density, ρ_i.

$$F(\rho_i) = -A\sqrt{\rho_i} = -A\Big[\sum_{i=1,j\neq i}^{N} \phi(r_{ij})\Big]^{\frac{1}{2}} \tag{2.63}$$

Here A is an embedding term, which is empirically derived for each material in question. Electronic temperature dependence is built into this potential via modifications to the embedding energy functional, $F(\rho_i)$ [38], and is derived by fitting the potential to high temperature DFT free energy-volume surfaces. This T_e dependent embedding term is thus,

$$F(\rho_i, T_e) = A^{DFT}(\rho_i, T_e) + dE(T_e) - \frac{1}{2}\sum_{i=1}^{N}\sum_{j\neq i}^{N} V_{ij}(r_{ij}) \tag{2.64}$$

A^{DFT} is the free energy calculated via DFT, and dE is the constant energy shift at each electronic temperature so the energy splines to zero at infinity. The resulting energy-volume curves for various electronic temperatures are show in figure 2.5.

As the electronic temperature of tungsten increases, three significant changes can be observed. Firstly, the minima of the free energy shifts to larger volumes, implying the equilibrium lattice parameter increases with increased electronic excitation. Secondly, the depth of the potentials get shallower for larger T_e, which indicates that the melting temperature of tungsten decreases for increasing T_e, as less energy is required to excite a particle out of this potential well. Finally, at 30,000 K and above, there is no minimum in the energy-volume

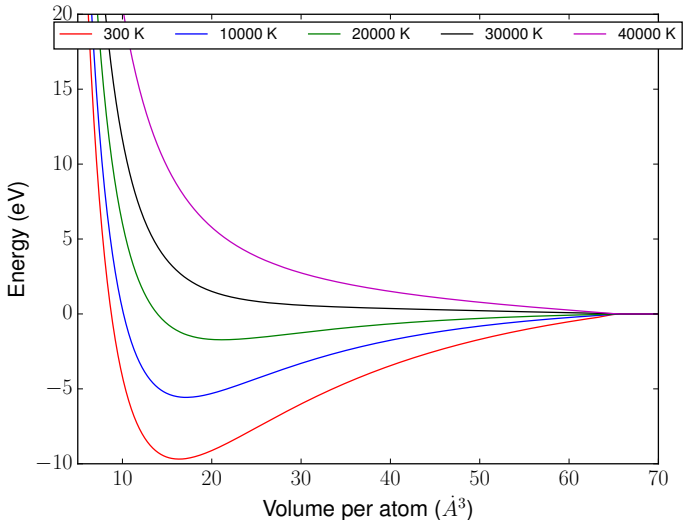

Figure 2.5: Energy-volume curves for various T_e in W, data reproduced from [38]. As the electronic temperature increases the bonding characteristics of the material change (equilibrium lattice paramter and well depth).

curve, thus the potential is completely repulsive. The implementation of these potentials was achieved by generating DFT energy-volume curves between 0 K and 40,000 K, in increments of 5,000 K. Potentials at intermediate values were obtained by cubic splining.

2.4.2 Silicon

Electronic temperature dependent interatomic potentials for silicon based on the well known modified Tersoff (MOD) potential [109] (described in section 2.1.3.3) have been developed by Shokeen and Schelling [39]. Conversely to W, the potentials are constructed using the force matching method [110], in which the potential is fit such that it reproduces the DFT cohesive free-energies for the diamond, fcc, bcc and simple cubic structures at several different volumes. The functional form of the potential is assumed to remain unchanged under this electronic excitation. Unfortunately the MOD potential was not properly contained in the software package DL_POLY. Thus the first substantial piece of work contained in this thesis was the correct implementation of the MOD potential. Figure 2.6 shows the energy-volume curve obtained from the correctly performing potential. It is in excellent agreement with

published results [109].

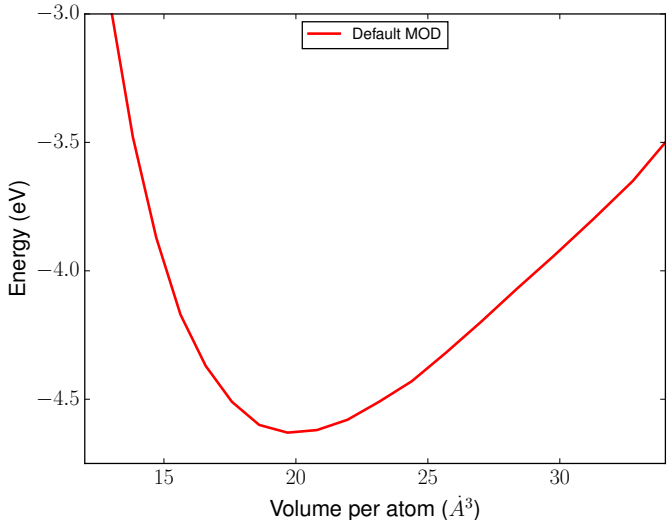

Figure 2.6: Cohesive free energy per volume for diamond silicon using the MOD interatomic potential

The corresponding energy-volume curves for the T_e dependent potentials are shown in figure 2.7, all of which agree with the original work [39]. An unrelaxed vacancy defect energy of 2.85 eV was also obtained using the potential, which is also in agreement with the past results. To ensure that the forces using the interatomic potential were also correct, a selection of simulations were setup to reproduce the thermodynamic results obtained by the original authors [111].

Figure 2.8 illustrates the thermal expansion of each of the elevated T_e dependent potential under NPT simulations for various different lattice temperatures.

The lattice with 300 K and 600 K T_e potentials both expand by about 7.5% from 0 to 1800 K. The more excited potentials become unstable between 200 K ($T_e = 30000$ K) and 600 K ($T_e = 15000$ K), the point at which the data terminates is where the lattice becomes unstable and melts. This clearly illustrates that electronic excitation can cause the melting temperature of silicon to decrease significantly. Once the potential was proven to work as expected, the

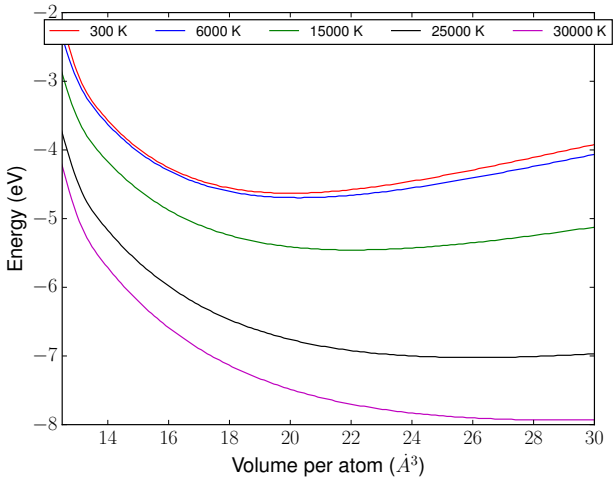

Figure 2.7: Energy-volume curves for various T_e in silicon

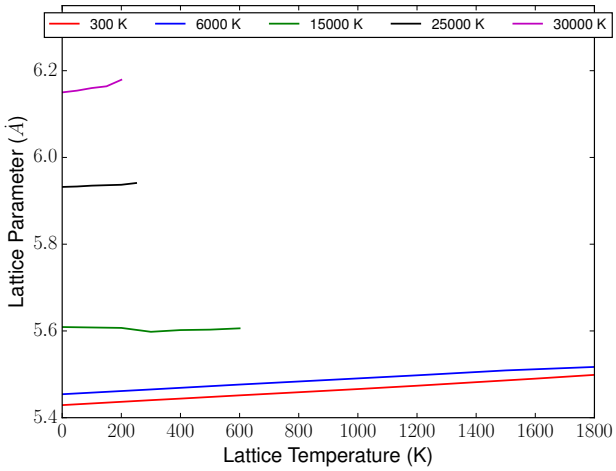

Figure 2.8: Thermal expansion of various T_e potentials in silicon

T_e dependence for intermediate values was implemented as follows. The functional form of the T_e dependent potentials is assumed to remain unchanged (see section 2.1.3.3), and each parameter in the potential is taken to vary as a sixth order polynomial;

$$\Gamma(T_e) = \sum_{n=0}^{6} a_n (k_B T_e)^n \tag{2.65}$$

Here Γ represents any of the default MOD parameters, and a_n is the polynomial coefficient. It was noticed during the implementation of this T_e dependence that there were a number of significant errors for the coefficients of two parameters in the potential in the original paper, c_4, which makes up the angular dependent term (and is attributed to being the main component in accurately reproducing the melting temperature of silicon), and α, an angular dependent term which is used to describe the system when far from equilibrium (something which is also clearly important for highly non equilibrium electronic excitation). The polynomials for α were completely recalculated with existing data, and the corrected values for both parameters are contained table 2.1.

Parameter	a_0	a_1	a_2	a_3	a_4	a_5	a_6
c_4	1.0	0.18	0.0	0.0	0.0	0.0	0.0
α	1.9	-0.39672	-0.112842	0.089009	0.01201	0.0	0.0

Table 2.1: Corrected polynomial values for c_4 and α.

2.5 Quantum Mechanical Methods

An all encompassing description of atomistic interactions requires quantum mechanics, which can be summarised by the many-body Schrödinger equation :

$$\hat{H}\Psi(\{\boldsymbol{r}_n\},\{\boldsymbol{R}_N\}) = E\Psi(\{\boldsymbol{r}_n\},\{\boldsymbol{R}_N\}) \tag{2.66}$$

$\hat{H}$ is the Hamiltonian operator, E is the energy of the system, and Ψ is the many-body wavefunction of the system, which depend on the set of electronic positions, $\{\boldsymbol{r}_n\}$, and nuclear positions, $\{\boldsymbol{R}_N\}$, respectively. The Hamiltonian for this many-body system is,

$$\hat{H} = -\frac{\hbar^2}{2m_e}\sum_i^n \nabla_i^2 - \sum_I^N \frac{\hbar^2}{2M_I}\nabla_I^2 + \frac{1}{2}\sum_{i\neq j}^n \frac{e^2}{4\pi\epsilon_0|\boldsymbol{r}_i - \boldsymbol{r}_j|} + \frac{1}{2}\sum_{I\neq J}^N \frac{Z_I Z_J e^2}{4\pi\epsilon_0|\boldsymbol{R}_I - \boldsymbol{R}_J|} - \sum_{i,I}^{N,n} \frac{Z_I e^2}{4\pi\epsilon_0|\boldsymbol{R}_I - \boldsymbol{r}_i|}, \quad (2.67)$$

where the electrons are denoted by lower case variables and subscripts, and the nuclei are described by upper case variables and subscripts. The first line of equation 2.67 is the kinetic energy of the electrons and nuclei respectively, the second line is the electron-electron and nuclear-nuclear potential energy respectively, and the third line is the electron-nuclei potential energy. Due to the complexity of this equation, the many-body Schrödinger equation is impossible to solve for even the most primitive systems. Thus realistic simplifications that do not significantly compromise the physics, but do ensure the system is computationally tractable, must be made.

2.5.1 The Born-Oppenheimer approximation

The forces acting on both the electrons and nuclei are of the same order of magnitude (due to their electric charge, e). However, the difference in mass between both particles is multiple orders of magnitude, thus nuclei have a much smaller velocity relative to the electrons. The separation of these nuclear and electronic motions allow for the construction of a wavefunction that explicitly depends on the electronic positions alone. This reduced Born-Oppenheimer Hamiltonian [63], H_{BO}, ignores the kinetic energy of the nuclei,

$$\hat{H}_{BO} = -\frac{\hbar^2}{2m_e}\sum_i^n \nabla_i^2 + \frac{1}{2}\sum_{i\neq j}^n \frac{e^2}{4\pi\epsilon_0|\boldsymbol{r}_i - \boldsymbol{r}_j|} - \sum_{i,I}^{N,n} \frac{Z_I e^2}{4\pi\epsilon_0|\boldsymbol{R}_I - \boldsymbol{r}_i|} \quad (2.68)$$

This leads to a new wavefunction for the electrons, Φ, which only depends parametrically on the nuclear positions,

$$\hat{H}_{BO}\Psi(\{\boldsymbol{r}_n\},\{\boldsymbol{R}_N\}) = E(\{\boldsymbol{R}_N\})\ \Phi(\{\boldsymbol{r}_n\},\{\boldsymbol{R}_N\}), \tag{2.69}$$

Despite the simplifications contained equation 2.68, the solution to this wavefunction is still computationally impossible for most systems (it is also important to note the explicit dependence of the energy eigenvalues, E, on the nuclear positions, $\{\boldsymbol{R}_N\}$). Thus further simplifications are necessary.

2.5.2 The Hartree and Hartree-Fock approximation

The next step in simplifying the many-body Schrödinger equation comes from separating the multi-electron wavefunction, Ψ, into the product of individual electron wavefunctions, ϕ_i.

$$\Psi(\boldsymbol{r}_1,\boldsymbol{r}_2,\ldots,\boldsymbol{r}_n) = \phi_1(\boldsymbol{r}_1)\phi_2(\boldsymbol{r}_2)\ldots\phi_n(\boldsymbol{r}_n) \tag{2.70}$$

Plugging equation 2.70 into the Schrödinger equation, and using reduced units, ($e = 4\pi\epsilon_0 = \hbar = m_e = 1$), results in,

$$\left[-\frac{1}{2}\sum_i^n \nabla_i^2 + \frac{1}{2}\sum_{i\neq j}^n \frac{1}{|\boldsymbol{r}_i-\boldsymbol{r}_j|} - \sum_{i,I}^{N,n}\frac{Z_I}{|\boldsymbol{R}_I-\boldsymbol{r}_i|}\right]\phi_1(\boldsymbol{r}_1)\ldots\phi_n(\boldsymbol{r}_n) = E[\phi_1(\boldsymbol{r}_1)\ldots\phi_n(\boldsymbol{r}_n)] \tag{2.71}$$

The solution of equation 2.71 using the variational principle leads to the Hartree equation.

$$\left[-\frac{1}{2}\nabla^2 + \frac{1}{2}\sum_{i\neq j}^n \int \frac{|\phi_i(\boldsymbol{r'})|^2}{|\boldsymbol{r}-\boldsymbol{r'}|}\,d^3\boldsymbol{r'} - \sum_I^N \frac{Z_I}{|\boldsymbol{R}_I-\boldsymbol{r}|}\right]\phi_j(\boldsymbol{r}) = E'\phi_j(\boldsymbol{r}) \tag{2.72}$$

Equation 2.72 is an extremely important step in making quantum mechanical calculations computationally possible for non-trivial systems. This is due to the fact that equation 2.72 describes a set of independent Schrödinger equations for each individual electron wavefunction (a 3n-dimensional function is reduced to n 3-dimensional functions). Here the first term is the kinetic energy of the individual electron in question, the second term is the interaction of the electron with all the other electrons in a 'mean field' average, and the third term is

the interaction of the electron with all of the nuclei. A few problems remain, the first being that the electron wavefunctions (which we want to solve) themselves appear in the electron-electron interaction of the effective Hamiltonian. This is overcome using the self consistent field method, which assumes initial estimate for ϕ, and iteratively solves equation 2.72 until convergence is achieved.

Another fundamental problem exists when using the Hartree approximation, and that is that Pauli's exclusion principle is not satisfied when assuming that the many-electron wavefunction can be split up into the product of individual electron wavefunctions. Pauli's exclusion principle states that the electronic wavefunction needs to be anti-symmetric, or,

$$\Psi(\boldsymbol{r}_1, \boldsymbol{r}_2, \ldots, \boldsymbol{r}_n) = -\Psi(\boldsymbol{r}_2, \boldsymbol{r}_1, \ldots, \boldsymbol{r}_n) \tag{2.73}$$

This can be achieved by assuming the wavefunction takes the form of a Slater determinant,

$$\Psi(\boldsymbol{r}_1, \boldsymbol{r}_2, \ldots, \boldsymbol{r}_n) = \frac{1}{\sqrt{n!}} \begin{vmatrix} \phi_1(\boldsymbol{r}_1) & \phi_2(\boldsymbol{r}_1) & \ldots & \phi_N(\boldsymbol{r}_1) \\ \phi_1(\boldsymbol{r}_2) & \phi_2(\boldsymbol{r}_2) & \ldots & \phi_N(\boldsymbol{r}_2) \\ \vdots & \vdots & & \vdots \\ \phi_1(\boldsymbol{r}_n) & \phi_2(\boldsymbol{r}_n) & \ldots & \phi_N(\boldsymbol{r}_n) \end{vmatrix} \tag{2.74}$$

Plugging this into the Schrödinger equation leads to the Hartree-Fock equation :

$$\left(\frac{1}{2}\nabla^2 - \sum_I^N \frac{Z_I}{|\boldsymbol{R}_I - \boldsymbol{r}|}\right)\phi_k(\boldsymbol{r}) + \sum_i^n \int \frac{|\phi_i(\boldsymbol{r'})|^2 \phi_k(\boldsymbol{r})}{|\boldsymbol{r} - \boldsymbol{r'}|}\, d^3\boldsymbol{r'} - \sum_i^n \frac{\phi_i^*(\boldsymbol{r'})\phi_k(\boldsymbol{r'})\phi_i(\boldsymbol{r})}{|\boldsymbol{r} - \boldsymbol{r'}|}\, d^3\boldsymbol{r'} = E_k\phi_k(\boldsymbol{r}). \tag{2.75}$$

The last term on the left of the Hartree-Fock equation is the exchange interaction term, and is a direct result of including the anti-symmetric Slater determinant for the wavefunction. This term has no classical counterpart. It creates repulsion between electrons of the same spin (due to Pauli's exclusion principle). There is still one fundamental concept that is not properly accounted for using the Hartree-Fock approximation, the electron-electron

interaction is treated as the sum of the interactions between each electron and the 'mean field' average of the others. This gives rise to electron correlation, which describes how much an electron is influenced by the presence of all the others, and without it electrons in Hartree-Fock theory end up getting too close to one another.

2.5.3 Density Functional Theory

DFT is by far the most widely used method for electronic structure calculation, and it is arguably the most widely used simulation technique across all of the physical sciences [112]. The main ideas behind DFT stem from the fact that the wavefuntion is an extremely complex quantity, so how can this be simplified? Equation 2.76 represents the probability of finding electrons at $\boldsymbol{r}_1, \boldsymbol{r}_2, \ldots, \boldsymbol{r}_n$.

$$\Psi^*(\boldsymbol{r}_1, \boldsymbol{r}_2, \ldots, \boldsymbol{r}_n)\Psi(\boldsymbol{r}_1, \boldsymbol{r}_2, \ldots, \boldsymbol{r}_n) = |\Psi(\boldsymbol{r}_1, \boldsymbol{r}_2, \ldots, \boldsymbol{r}_n)|^2 \tag{2.76}$$

The intergral of this probability in all of space will result in the total number of electrons in the system, n.

$$\int |\Psi(\boldsymbol{r}_1, \boldsymbol{r}_2, \ldots, \boldsymbol{r}_n)|^2 \, d\boldsymbol{r}_1 d\boldsymbol{r}_2 \ldots d\boldsymbol{r}_n = n \tag{2.77}$$

The integral of the probability of finding an electron, $n(\boldsymbol{r})$ (described in equation 2.76, and is a true observable), over space is thus also the total number of electrons in the system.

$$\int n(\boldsymbol{r}) \, d\boldsymbol{r} = n \tag{2.78}$$

If the electron density is considered instead, the problem is instantly made more simple (a $3n$-dimensional problem is reduced to a 3-dimensional problem), but the question remains, is the electron density a valid replacement for the multi-electron wavefunction? To more formally introduce the essential equations in DFT, it is useful to rewrite the electronic Hamiltonian (with the Born-Oppenheimer approximation included) with the electron-nuclei interaction represented as an external potential, V_{ext}, which act on each electron due to the spatial distribution of the nuclei. This external potential is the only term which distinguishes one material from another, as electron-electron interactions are identical.

$$\hat{H} = -\frac{1}{2}\sum_{i}^{n}\nabla_i^2 + \frac{1}{2}\sum_{i\neq j}^{n}\frac{1}{|\boldsymbol{r}_i - \boldsymbol{r}_j|} - \sum_{i}^{n}V_{ext}(\boldsymbol{r}_i) \tag{2.79}$$

The validity of using electron density as a quantity in quantum mechanical calculations was rigorously derived in two seminal theorems by Pierre Hohenberg and Walter Kohn in 1964 [113]. The proof of each is not included, but a description of each follows. The first theorem states that the external potential, V_{ext}, and hence the total energy of the ground state system (as the other components of equation 2.79 are not unique), is a unique functional of the ground state electron density, $n(\boldsymbol{r})$. Equation 2.80 summarise this results.

$$\Psi_0(\boldsymbol{r}_1, \boldsymbol{r}_2, \ldots, \boldsymbol{r}_n) = \Psi[n_0(\boldsymbol{r})], \tag{2.80}$$

Ψ_0 is the ground state wavefunction, Ψ is the unique functional (a function which outputs another function), and n_0 is the ground state electron density. This in turn allows us to define the ground state of any observable, O_0, as,

$$O_0 = O[n_0(\boldsymbol{r})] = \langle \Psi[n_0(\boldsymbol{r})] \,|\, \hat{O} \,|\, \Psi[n_0(\boldsymbol{r})] \rangle \tag{2.81}$$

Thus any operator, $\hat{O}$, is also a functional of the ground state electron density. The second theorem states that electron density that minimises the energy of this functional is the true ground state density of the system.

$$E_v[n_0(\boldsymbol{r})] \leq E_v[n(\boldsymbol{r})] \tag{2.82}$$

Here E_v is the energy of a system in a given external potential, n_0 is the ground state electron density, and $n(\boldsymbol{r})$ is any electron density. It is important to stress that the actual form of this functional is unknown. The total energy is formulated as follows,

$$E[n] = F[n] + V_{ext}[n] = F[n] + \int V_{ext}(\boldsymbol{r})n(\boldsymbol{r})d^3\boldsymbol{r} \tag{2.83}$$

Thus the total energy functional, $E[n]$, is made up of two separate functionals, one due to the external potential functional, and the universal functional, $F[n]$, which is made up of the electronic kinetic energy, and electron-electron interactions. The external poten-

tial functional is relatively straightforward, the challenge is in determining what makes up the universal functional (here is where exchange and correlation exist). The Kohn-Sham approach considers a fictitious system of non-interacting electrons where the ground state density is the same as in the real system. The total energy of this non-interacting electronic system becomes :

$$E[n] = T_{ni}[n] + V_{ne}[n] + V_{ee}[n] + \Delta T[n] + \Delta V[n] \tag{2.84}$$

$T_{ni}[n]$ is non-interacting electronic kinetic energy, $V_{ne}[n]$ is electron-nuclear interaction, $V_{ee}[n]$ is the classical electron-electron repulsion (which includes self interaction, the influence presence an electron will have on itself), $\Delta T[n]$ is the correction required to obtain the correct kinetic energy, and $\Delta V[n]$ is the correction required to obtain the correct electron-electron repulsion. The correction terms are grouped together, along with the quantum mechanical terms (exchange and correlation) into one term known as the exchange-correlation term, $E_{xc}[n]$. The energy is thus,

$$E[n] = T_{ni}[n] + V_{ne}[n] + V_{ee}[n] + E_{xc}[n] \tag{2.85}$$

The density can be expressed as a basis set of single electron wavefunctions, ϕ_i,

$$n(\boldsymbol{r}) = \sum_{i=1}^{n} |\phi_i|^2, \tag{2.86}$$

The minimisation of this energy functional leads to a set of one electron eigenvalue equations similar to those described previously in Hartree-Fock theory.

$$\left[-\frac{1}{2}\nabla^2 - \sum_{I}^{N} \frac{Z_I}{|\boldsymbol{R}_I - \boldsymbol{r}|} + \frac{1}{2}\int \frac{n(\boldsymbol{r'})}{|\boldsymbol{r} - \boldsymbol{r'}|}\, d\boldsymbol{r'} + V_{xc}(\boldsymbol{r}) \right] \phi_i(\boldsymbol{r}) = E_i \phi_i(\boldsymbol{r}) \tag{2.87}$$

E_i is the energy eigenvalue, and equation 2.87 is known as the Kohn-Sham equation. The exchange-correlation term is also defined as,

$$V_{xc}(\boldsymbol{r}) = \frac{\delta E_{xc}[n(\boldsymbol{r})]}{\delta n(\boldsymbol{r})}, \tag{2.88}$$

which is a functional derivative of the exchange-correlation energy, with respect to a change

in the electron density. Despite the similarity of equation 2.87 and the Hartree-Fock equation, it is important to distinguish some of their key differences. In the Kohn-Sham model, no knowledge of the form of the wavefunctions is assumed, as in Hartree-Fock, but instead we are formulating the density 2.86. In Kohn-Sham theory, ignorance is shifted into a single parameter, $V_{xc}(\boldsymbol{r})$. This shift results in DFT being an exact theory. If the form of the exchange-correlation interaction is known, the energy is exactly known (the problem arises in knowing $V_{xc}(\boldsymbol{r})$). Hartree-Fock theory can be seen analogously as the reverse of this. It is inherently approximate as a theory (it is incapable of accounting for correlation), and it does not suffer from electron self interaction.

There are two significant aspects of DFT that have contributed to its enormous success in applications to real world systems. One is the variety of ways in which exhange-correlation is accounted for (which will be discussed in detail later), and the second is the pseudopotential approximation. The pseudopotential approximation states that in a solid, electrons close to the nucleus do not significantly contribute to the chemical, mechanical, or electronic properties of the material, thus it is possible to model the Coulombic interaction of the core electrons as a simpler pseudopotential. This simplification allows for the computation of larger systems, leading to an increase in tractability.

2.5.3.1 Exchange-correlation functionals

A key tenet of DFT is to group all of the difficult to deal with interactions into a single functional known as exchange-correlation. Exchange is typically a small contribution, and correlation even smaller, thus even somewhat crude methods for estimating $V_{xc}(\boldsymbol{r})$ can lead to accurate results. The first successful attempt is known as the local density approximation (LDA) [114], and it treats the generally inhomogeneous electronic system as locally homogeneous.

$$E_{xc}^{\mathrm{LDA}}[n] = \int n(\mathbf{r})\epsilon_{xc}(n)\ \mathrm{d}\mathbf{r} \tag{2.89}$$

E_{xc}^{LDA} is the exchange-correlation energy predicted by LDA. $\epsilon_{xc}(n)$ is the exchange-correlation energy per particle of a uniform electron gas and is characterised from Quantum Monte-Carlo data. LDA tends to favour electron densities that are more homogeneous than in reality. It tends to overestimate the binding energies of molecules and the cohesive energy of solids (op-

posite trend to Hartree-Fock). It also underestimates band gaps, and in some cases predicts metallic behaviour for semiconductors.

The success of LDA was built upon by attempting to incorporate the effects of inhomogeneities. This was achieved by considering the gradient of the local electron density. This method is know as the generalised gradient approximation (GGA), and the exchange-correlation functional takes the form,

$$E_{xc}^{\mathrm{GGA}}[n] = \int n(\mathbf{r})\epsilon_{xc}(n)F_{xc}[n, \nabla n]\ \mathrm{d}\mathbf{r}\ , \tag{2.90}$$

$\epsilon_{xc}(n)$ is the same exchange-correlation energy found in LDA, and F_{xc} is an enhancement factor. Unlike LDA, there are many approaches in which this enhancement factor can be applied. The method by Perdew, Burke, and Ernzerhof [115] is used here. GGA leads to an improvement in binding energies, atomic energies, lattice constants (not in all cases), and angles. It predicts better band gaps than LDA, but still far from actual values. Electron self interaction still remains a key problem.

A method developed to overcome self interaction is the utilisation of hybrid functionals, where a portion of the exchange contribution is taken from Hartree-Fock, and portion from DFT. This mixing can lead to results that are significantly more accurate in comparison to either method when used independently. Two hybrids are used in this thesis, PBE0 [116] and HSE [117]. The exchange-correlation energy of PBE0 takes the form,

$$E_{\mathrm{xc}}^{\mathrm{PBE0}} = aE_{\mathrm{x}}^{\mathrm{HF}} + (1-a)E_{\mathrm{x}}^{\mathrm{PBE}} + E_{\mathrm{c}}^{\mathrm{PBE}} \tag{2.91}$$

$E_{\mathrm{x}}^{\mathrm{HF}}$ is the exchange contribution from Hartree-Fock, and $E_{\mathrm{x}}^{\mathrm{PBE}}$ is the portion taken from DFT (in this case the PBE functional, which is a form of the generalised gradient approximation). $E_{\mathrm{c}}^{\mathrm{PBE}}$ is the correlation contribution (all of which must be taken from DFT, as it is not accounted for in HF theory). a is the proportion of exchange taken from Hartree-Fock, and is usually taken to be 0.25, a value obtained via perturbation theory. The PBE0 functional leads to much more accurate energies for molecular systems, but now suffers from an overestimation of band gaps in semiconductors.

Heyd, Scuseria, and Ernzerhof formulated a screened Coulomb approach which solved inaccuracies in the band gap of semiconductor systems. The approach involves splitting

exchange into short and long range contributions, with a screening function tuning between these both these limits. The screening function is parameterised by ω, so when $\omega = 0$, the short range component is sole contributor to exchange, and vice versa for $\omega \to \infty$. The HSE screened Coulomb potential hybrid density functional takes the form,

$$E_{\mathrm{xc}}^{\mathrm{HSE}} = aE_{\mathrm{x}}^{\mathrm{HF,SR}}(\omega) + (1-a)E_{\mathrm{x}}^{\mathrm{PBE,SR}}(\omega) + E_{\mathrm{x}}^{\mathrm{PBE,LR}}(\omega) + E_{\mathrm{c}}^{\mathrm{PBE}} \tag{2.92}$$

$E_{\mathrm{x}}^{\mathrm{HF,SR}}$ is the short ranged component of the Hartree-Fock exchange energy, $E_{\mathrm{x}}^{\mathrm{PBE,SR}}$ is the short ranged component of the DFT exchange contribution (in this case again the PBE approach to the generalised gradient approximation), $E_{\mathrm{x}}^{\mathrm{PBE,LR}}$ is the long ranged component of the DFT exchange energy, $E_{\mathrm{c}}^{\mathrm{PBE}}$ is the correlation energy, ω is the screening parameter for the exchange contribution, and a is the proportion of exchange taken from Hartree-Fock. Standard values of $\omega = 0.2$ and $a = 0.25$ yield accurate results for many systems. The screening function means that at $\omega = 0$ the functional is identical to PBE0, and at $\omega \to \infty$ the functional reproduces PBE.

2.5.3.2 High temperature DFT

Up until this point the exact nature of DFT is only applicable to the ground state properties of the system in question. Extending this to systems at finite temperature is extremely important for SHI applications, as the electrons can reach temperatures up to 1,000,000 K. The extension of the Kohn-Sham theorems to encompass systems at finite temperature was achieved by Mermin in 1965 [118]. The central idea is to construct approximate free-energy functionals, which in turn allow the determination of the equilibrium free-energy at various electronic temperatures. The electronic free-energy is,

$$F = E - T_e S, \tag{2.93}$$

where F is the free-energy, E is the internal energy, T_e is the electronic temperature, and S is the entropy. The energy, E, is made up of the same components described previously, only now they apply to a certain equilibrium temperature (and not the ground state). The electronic entropy, S , is a sum over all occupied and unoccupied states,

$$S = -2k_B \sum_i \big[f_i \ln(f_i) + (1 - f_i) \ln(1 - f_i) \big], \tag{2.94}$$

where f_i is the occupancy of the excited electrons, and can be described by a Fermi-Dirac distribution.

$$f_i = \frac{1}{e^{(\epsilon_i - \mu_e)/k_B T_e} + 1} \tag{2.95}$$

ϵ_i is the corresponding energy of i, μ_e is the chemical potential, T_e is the electronic temperature, and k_B is Boltzmann's constant. The equilibrium density for the excited electrons that minimises the free-electron functional takes the form,

$$n(\boldsymbol{r}) = \sum_{i=1}^{n} f_i |\phi_i|^2, \tag{2.96}$$

where ϕ again is a basis set of single electron wavefunctions. Thus all the constitiuent energy quantities that depend on the electron density have an inherent temperature dependence (via the occupation term in equation 2.96). While Mermin put the high temperature DFT on the same robust theoretical level as ground state DFT (by extending the Kohn-Sham equations to high tempeartures), there are still some important caveats in actually applying the theory in these extreme conditions. These have been discussed in the previous chapter.

2.6 Track radius determination

The creation of ion tracks in silicon forms a substantial part of the research contained in this thesis, and as ion tracks are defect rich cylindrical regions, quantifying the radius of said track accurately is a key indicator of the extent of disorder in a given simulation. A number of approaches were considered, and a brief description and analysis of each follows. The MD simulation cell is setup to be centred at (0,0,0), and the energy is also centrally deposited, thus the 'cylindrical' ion track is also centred at the origin. The first two approaches involved picking the edge region of an ion track by eye, and using structural analysis modifiers contained in the OVITO [119] visualisation package to determine the radius. Figure 2.9 demonstrates ion track images analysed with these modifiers. Figures 2.9 (a) and (c) il-

lustrate the various structures in the cell. Figures 2.9 (b) and (d) contain images of the Wigner-Seitz analysis of the same simulation cell. Wigner-Seitz defects are determined as follows : first a reference Wigner-Seitz cell is created from the initially undamaged reference cell, then a Wigner-Seitz cell is constructed for the final configuration. Cells are subsequently compared, and any initial cell where an extra atom has moved into is counted as an interstitial defect, and any initial cell which now lies empty is counted as a vacancy defect.

Analysing the various images in figures 2.9 show that there is negligible difference between the ion track edge when highlighting a lack of diamond structure, and Wigner-Seitz defects. Despite this consistency, there are numerous disadvantages to attempting to determine track radii via eye. The most significant is the inhomogeneous nature of the track, (a) and (b) are far from a perfect circle (the track radius varies between 25.73 Å and 28.39 Å). Likewise, (c) and (d) show large variations in track radius longitudinally. Thus the ability to accurately (and consistently) determine the radius of an ion track by eye is doubtful. There is also significant discussion on how valid comparisons are between ion track measurements made between Rutherford backscattering spectrometry (RBS-c) and small angle xray scattering (SAXS) experiments. RBS-c experiments measure the ratio of damaged to perfect crystal, and SAXS measures the spatial change in electron density. It is postulated that the discrepancy between both methods arises due to small defect channels that occur on the edges of the ion track. RBS-c experiments are sensitive to these defects, and at high electronic stopping powers a larger proportion of these channels are formed, meaning RBS-c measurements overestimate track radii in comparison to SAXS. As a correspondence between simulation and experiment is pivotal, a more comprehensive approach to determining track radii was chosen.

As SAXS experiments examine changes in electron density, a plot of particle density (or volume) vs distance from the centre of the cell allows for a more direct comparison with any future results. The following was achieved using the voro++ [120] software package in conjunction with OVITO : a Voronoi cell is constructed from our simulation cell, which results in each atom having a polyhedron which is determined by the orientation of its nearest neighbours. This polyhedron has a corresponding volume, and this volume gives an accurate measurement of the local packing fraction. Thus when each particle's volume is converted

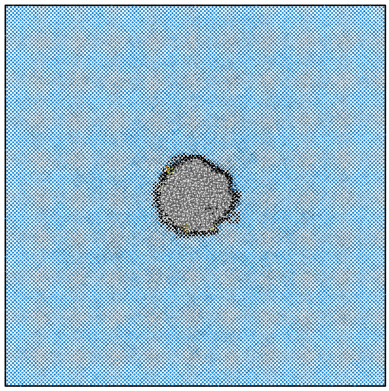

(a) Top view - diamond modifier

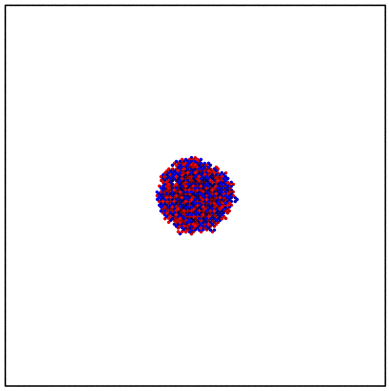

(b) Top view - Wigner-Seitz defects

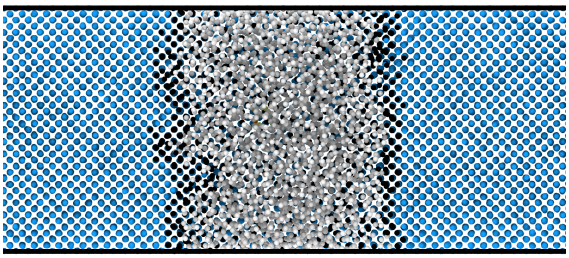

(c) Vertical slice - diamond modifier

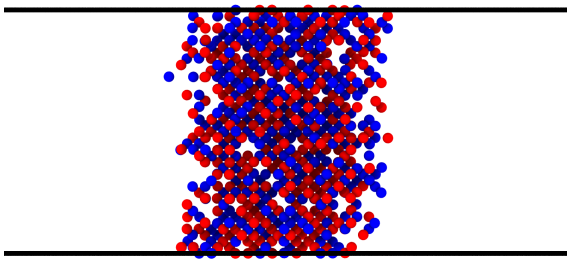

(d) Vertical slice - Wigner-Seitz modifier

Figure 2.9: Images of ion track simulations in silicon using various structure analysis modifiers. (a) and (c) use illustrate diamond structure, with blue representing cubic diamond, black labels atoms with cubic diamond as first or second nearest neighbours, and grey represents amorphous structure. (b) and (d) represent Wigner-Seitz defects, where blue is a vacancy, and red an interstitial.

to a density, a graph of density vs distance from the centre of the simulation cell can be obtained. Figure 2.10 illustrates a typical example of this.

The ion track can clearly be seen as overdense region, and the radius is the point at which this region ends. This corresponds to the first turning point in the curve when the relative density drops below one (26.01 Å). This method for determining track radii is significantly

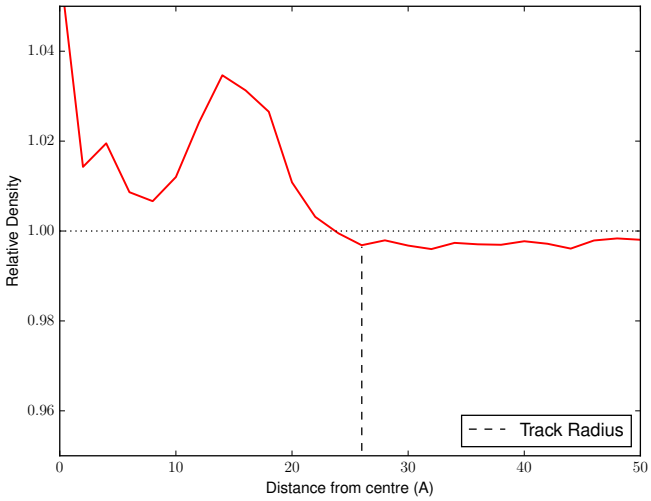

Figure 2.10: Relative density vs distance from the centre of a typical SHI irradiated silicon cell.

more robust and detailed, as it takes into account every atom in the simulation cell, it allows direct comparison with SAXS experiments, and it also illustrates thermodynamic properties of the material under investigation (the density of crystalline silicon has been shown to increase in the process of melting, which is verified in figure 2.10). This method is inherently more statistically robus, as the relative density of every atom in the cell is taken into account, as opposed to focusing on treating the radius of a certain slice of the 'pseudo-cylindrical' ion track (and potentially averaging across a variety of these slices).

In summary, the main technique used to simulate SHI irradiation in this thesis is an augmented formulation of molecular dynamics. However, due to the inherently quantum mechanical nature of the systems under investigation, as many parameters as possible that are put into the MD simulations are derived via *ab initio* methods (with explicit temperature dependence if possible, as SHI irradiation is an extremely non-equilibrium interaction). The theory behind these techniques has been described thoroughly, as well as the methods required to accurately quantify the level of damage caused in a typical SHI simulation. The next chapter will describe how all of these methodologies were combined to successfully describe defect formation in various fcc and bcc metals.

3

Swift heavy ion irradiation of metals

> "For me too, the periodic table was a passion. ... As a boy, I stood in front of the display for hours, thinking how wonderful it was that each of those metal foils had its own distinct personality."
>
> Freeman Dyson

The aim of this chapter is to investigate the established defect distributions (and their evolution) following swift heavy ion irradiation of various bcc and fcc metals using atomistic two-temperature molecular dynamics (2T-MD). There are a number of motivations for this. Firstly, metals have been broadly overlooked when it comes to SHI irradiation as it has been assumed that the rapid redistribution of free electrons means that damage is highly unlikely. The results that follow conflict with this predominant view. Another important reason is to do with the two-temperature model itself. There still remains criticism of how accurately it applies to situations with significant electronic excitation. The best parameterisation of the electronic system possible for the two-temperature model exists for simple metallic systems. Thus the reliability and applicability of the model itself can be strengthened by reproducing past experimental results and/or predicting interesting outcomes that may be verifiable in future experiments.

The chapter is split into two sections, one for two bcc metals (iron and tungsten), and one for two fcc metals (nickel and copper). Each section begins with an introduction into the model parameters. This is followed by a description of the simulation setup, and a detailed

analysis of the system throughout various swift heavy ion irradiations. A number of different bcc and fcc metals were chosen to highlight how a multitude of factors contribute to defect creation, and there are clear and significant differences in each metal investigated. Although research on SHI irradiation of monatomic metals has been rare, the comparisons between simulations and literature are made where possible, and the results agree extremely well.

3.1 Body-centred cubic metals

The two body-centred cubic metals chosen for investigation were iron and tungsten. The reason being experimental literature exists on which the simulations can be compared, as well as good data on the electronic parameters, and accurate interatomic potentials derived with the same functional form.

3.1.1 Model parameters for body-centred cubic metals

3.1.1.1 Electronic system

The key parameters that determine the temperature evolution of the electronic subsystem are the electronic thermal conductivity, (κ_e), the electronic specific heat capacity, (C_e), the electron-phonon coupling, G_e, and deposition profile of the incoming SHI, A. The biggest hurdle in utilising the 2T-MD model arises from a lack of depth in knowledge about one or many of these parameters. Fortunately in the case of Fe and W, most of these are well characterised, including explicit temperature dependences. At this point it is worth recasting the electronic heat diffusion equation in a way that clearly illustrates how the parameters influence electronic temperature evolution.

$$\frac{\partial T_e}{\partial t} = \underbrace{\frac{\kappa_e(T_i)}{C_e(T_e)}}_{(a)} \nabla^2 T_e - \underbrace{\frac{G_e(T_e)}{C_e(T_e)}}_{(b)}(T_e - T_i) + \underbrace{\frac{A(r,t)}{C_e(T_e)}}_{(c)}, \tag{3.1}$$

(a) describes the rate at which energy gets transferred laterally through the electronic system (also called the diffusivity). (b) describes the rate of energy transfer to the lattice, and, (c), the source term, describes how much energy gets initially transferred from swift heavy ion to the electrons in the metal. The electronic specific heat outlined by Lin *et al.* [44]

was used, which states the electronic specific heat depends on the derivative of the Fermi function and the electronic density of states.

$$C_e = \int_{-\infty}^{\infty} g(\epsilon) \frac{\partial f(\epsilon, \mu, T_e)}{\partial T_e} \, \epsilon \, d\epsilon \tag{3.2}$$

$g(\epsilon)$ is electronic density of states (DOS) at the energy ϵ, μ is the chemical potential at electronic temperature T_e, and $f(\epsilon, \mu, T_e)$ is the Fermi-Dirac distribution function at these values,

$$f(\epsilon, \mu, T_e) = \frac{1}{e^{(\epsilon_i - \mu_)/k_B T_e} + 1} \tag{3.3}$$

The chemical potential can be obtained by equating the number of electrons, N_e, to the integral product of the Fermi-Dirac distribution with the DOS across all energy levels.

$$N_e = \int_{-\infty}^{\infty} g(\epsilon) f(\epsilon, \mu, T_e) \; d\epsilon \tag{3.4}$$

This allows for the calculation of a temperature dependent electronic specific heat capacity, and figure 3.1 illustrates this relationship for iron and tungsten.

For the majority of ranges of electronic temperatures considered, the electronic specific heat of iron is significantly greater than that of tungsten. The cause of this is due to differences in the electronic density of states, and is outlined in the work of Lin [44]. The number of available electronic states around the fermi level is key in determining any materials behaviour (and is the distinguishing difference between band gap materials and metals). As iron has a much higher proportion of available density of states at the Fermi level, the corresponding electronic specific heat is lower at lower electronic temperatures. As the temperature increases, the smearing effect of the Fermi-Dirac distribution allows the population of states either side of the Fermi level in tungsten (which eventually saturates). In Fe, at the highest electronic temperatures the same smearing reduces the number of available, resulting in an increase in the electronic specific heat. These differences in these $C_e(T_e)$ will contribute to pronounced differences in the temperature evolution of the electronic system of W and Fe. The first contribution is in the temperature rise due to the energy deposition, and is illustrated by (c) in equation 3.1. So for a given constant energy deposition, tung-

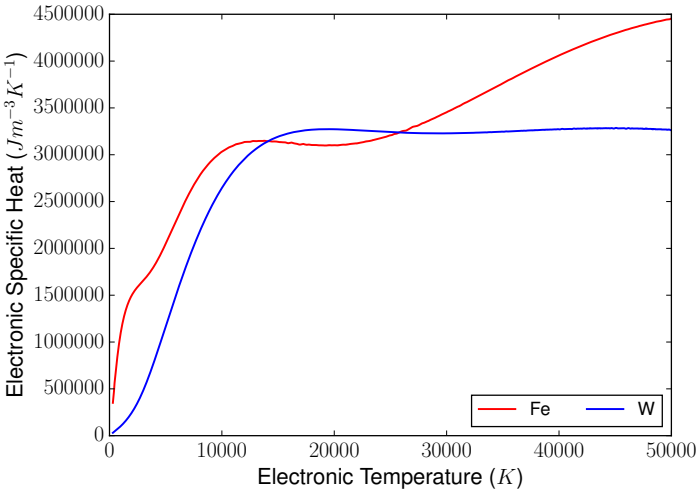

Figure 3.1: Graph of the electronic specific heat capacity vs electronic temperature for tungsten and iron. Data reproduced from the work of Lin *et al.* [44]. The electronic specific heat of iron is higher than that of tungsten for the majority of the electronic temperatures.

sten, which has a consistently lower electronic specific heat, will reach significantly higher electronic temperature than iron.

The electron-phonon coupling constant is obtained in the same way as described by Lin *et al.* [44]. A detailed approach is based on quantum field theory, and is beyond the scope of this thesis. However in simple terms, the electrons and lattice are assumed to have two distinct temperatures, thus the occupations can be described by Fermi-Dirac and Bose-Einstein distributions respectively. Near room temperature only electronic states near the Fermi level contribute to scattering processes, allowing a simplified value for the electron-phonon coupling to be obtained. At high electronic temperatures the thermal excitation of electrons below the Fermi level contribute significantly to the electron-phonon coupling, so the DOS again plays a key role. After making an assumption that the probability of an electron scattering from one energy state to another is independent of the electronic states themselves, when summed over all scattering angles, the electronic temperature dependent electron-phonon coupling term simplifies to equation 3.5.

$$G_e(T_e) = \frac{\pi \hbar k_B \lambda \langle \omega^2 \rangle}{g(\epsilon_F)} \int_{-\infty}^{\infty} g^2(\epsilon) \left(-\frac{\partial f}{\partial \epsilon} \right) d\epsilon \tag{3.5}$$

$G_e(T_e)$ is the electron-phonon coupling, λ is the electron-phonon mass enhancement factor, $\langle \omega^2 \rangle$ is the second moment of the phonon spectrum, and $g(\epsilon_F)$ is the density of states at the Fermi level. Figure 3.2 illustrates this relationship for iron and tungsten. At 300 K there is an order of magnitude difference between the respective e-p coupling values, after which the e-p coupling of iron significantly decreases, while the e-p coupling of tungsten signficantly increases. At roughly 20 000 K the values converge, and for both materials the e-p coupling decreases at a similar rate (with a difference of about 20%). During a typical SHI irradiation, it is rare for the electrons in the material to exceed 20 000 K for a period of time (and spatial region) long enough for this area of the graph to be a significant contributor to the electronic temperature evolution. Therefore the most important portion of figure 3.5 is where the e-p coupling of iron is significantly greater than that of tungsten, with convergence at higher temperatures. From this region it is expected that the rate of energy exchange between the electronic and lattice subsystems will be greater in iron than in tungsten.

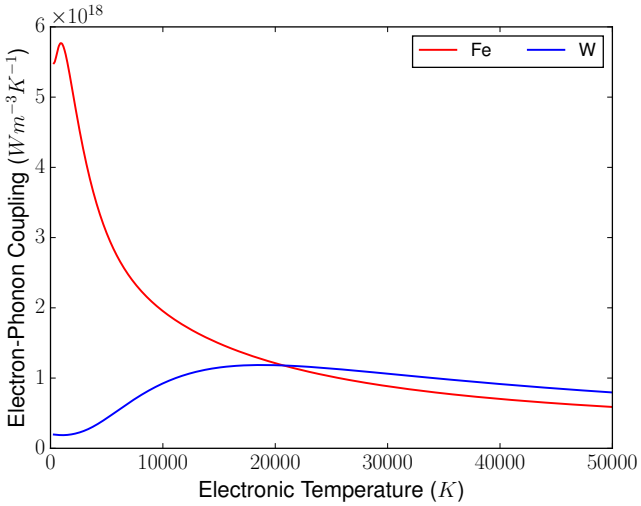

Figure 3.2: Graph of the electronic-phonon coupling vs electronic temperature for tungsten and iron. Data reproduced from the work of Lin *et al.* [44]. The electronic specific heat of iron is higher than that of tungsten up to 20.000 K, after which the trend reverses.

However, by analysing (b) in equation 3.1, $G_e(T_e)$ is not the sole contributor. It is actually the ratio of the e-p coupling to the electronic specific heat that determines this rate of exchange. This ratio is $G_e(T_e)/C_e(T_e) = \tau_{ep}^{-1}$, where the inverse of τ_{ep} is the electron-phonon coupling strength. Figure 3.3 illustrates that this coupling strength is significantly greater for iron for all realistic elevated electronic temperatures in a SHI simulation. Thus energy will flow from the electrons to the lattice significantly faster for iron than tungsten. It is important to emphasise that this information does not necessarily mean iron will damage more or less than tungsten for the same energy deposition, as the thermal properties of the lattice (heat capacity, melting temperature, latent heat of melting, etc), and the rate at which energy disperses throughout the electronic system, are also crucial in determining the produced defect distributions.

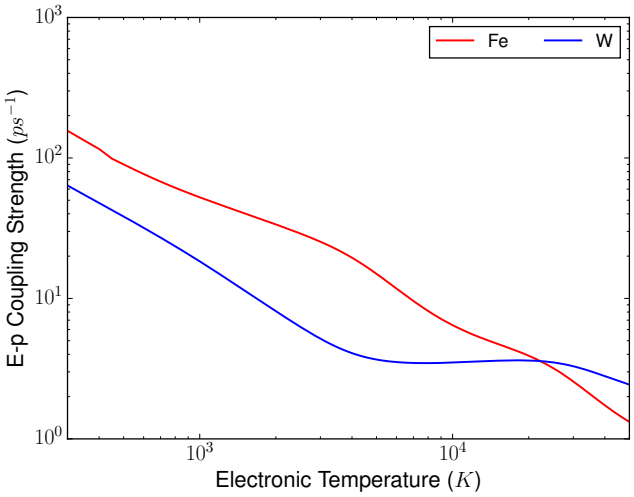

Figure 3.3: Graph of the electronic-phonon coupling strength vs electronic temperature for tungsten and iron. The coupling strength is greater for iron than tungsten up to 20 000 K. After this point this trend reverses.

The source term takes the form described in Khara *et al.* [121] (and previously described in chapter 2). All metals had a characteristic spatial deposition radius taken to be 1 nm (which is the diameter of the electronic temperature voxcells), and characteristic deposition time 1 fs, which corresponds to the thermalisation time for the initially produced delta electrons.

Changing both of these parameters by up to an order of magnitude was found to have little impact on the electronic temperatures. The final term to discuss in the electronic subsystem is the electronic thermal conductivity, κ_e, which describes how heat diffuses in the electronic system. For all metals studied, this is assumed to be the same as the thermal conductivities determined by various experiments in the handbook [122]. While these values are the total thermal conductivity (made up of both lattice and electronic contributions), it is well known that the electronic contribution is dominant in metals due to the availability of free electrons. A complete description of these thermal conductivities would also have explicit electronic and lattice temperature dependences. However, this work also assumes that the thermal conductivity is lattice temperature dependent only. Again from looking at (a) equation 3.1, the important parameter is not only the electronic thermal conductivity, but its ratio to the electronic specific heat. This ratio is called the electronic diffusivity, D_e. Figure 3.4 illustrates the electronic thermal conductivity and diffusivity for iron and tungsten. As the diffusivity is a function of both the electronic and lattice temperature, this diffusivity takes the form of a surface plot.

κ_e is significantly greater in tungsten for every electronic temperature. This also holds true for the diffusivity across a majority of the temperature ranges. The only point at which they are similar is at extreme electronic excitation. Thus for a given energy deposition, temperature will spread faster throughout the electronic subsystem in tungsten. This can have two effects. If the e-p coupling (and initial deposited energy) is high enough, a large thermal conductivity can cause a larger region of the lattice to melt. However, if the e-p coupling is not high enough, this spread of energy in the electronic system can actually reduce the number of defects produced, as the energy will dissipate throughout the electronic system before being transferred to the lattice. This highlights the necessity of computational simulations, as the possible interaction dynamics could go in either direction.

Summarising the electronic 2T-MD parameterisation for iron and tungsten, iron has the greater electronic specific heat, meaning it will reach lower initial electronic temperatures. Iron also has the stronger electron-phonon coupling, so energy will transfer from the electronic system to the lattice faster in iron. Finally, tungsten has the greater electronic thermal conductivity, meaning electronic energy will be diffuse faster through the electronic system for tungsten. The next step, before running 2T-MD simulations, is to describe the properties

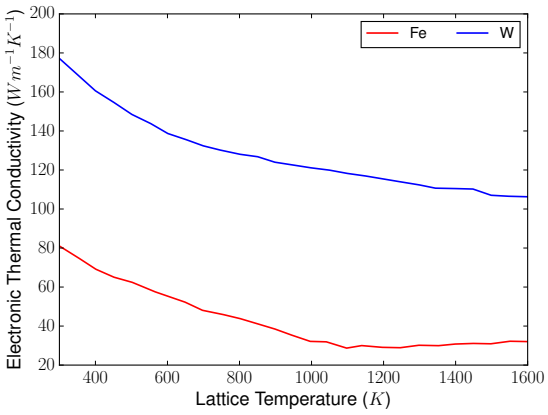

(a) Electronic thermal conductivity vs lattice temperature for bcc metals.

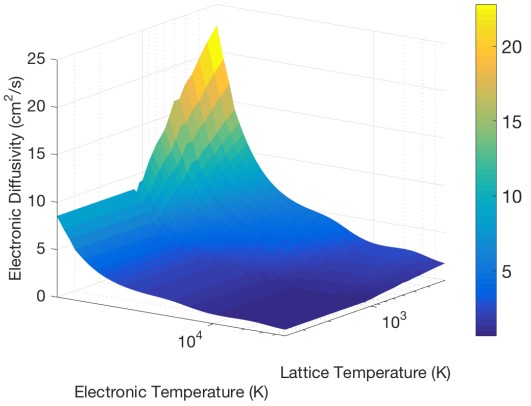

(b) Temperature dependent diffusivity surface of iron.

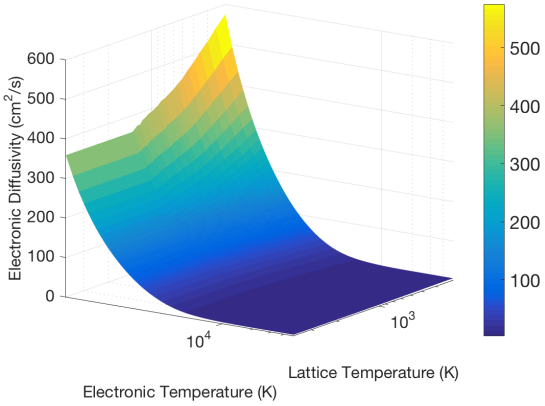

(c) Temperature dependent electronic diffusivity surface of tungsten.

Figure 3.4: Graph of the (a) electronic thermal conductivity vs lattice temperature, (b) electronic diffusivity vs temperature for iron, and (c) the electronic diffusivity vs temperature for tungsten. The data clearly shows that energy will flow significantly more quickly through the electronic system of tungsten.

of the lattice, ie - the properties of the interatomic potentials utilised.

3.1.1.2 Interatomic potential properties

All metals studied in this chapter use the Extended Finnis-Sinclair potential, as described in sections 2.1.3.1. The potential successfully reproduces both bcc and fcc bulk material properties. The bulk properties predicted by the potential for Fe are summarised in table 3.1.

	a (Å)	E_c (eV)	E_v^f(eV)	C_{11} (MBar)	C_{12}	C_{44}	T_m (K)	L_m (kJ mol^{-1})
Pot	2.87	4.273	1.86	2.263	1.406	1.155	2100	17.25
Exp	2.87	4.28	1.79	2.26	1.40	1.16	1811	13.80

Table 3.1: Bulk properties of iron calculated using the extended Finnis-Sinclair potential. a is the lattice parameter, E_c is the cohesive energy, E_v^f is the vacancy formation energy. C_{11}, C_{12}, and C_{44} are elastic constants, T_m is the melting temperature, and L_m is the latent heat of melting. The first line illustrates the bulk properties obtained with the potential, and the second line gives the corresponding experimental results. All values are taken from the original paper [106].

The results obtained using the potential in table 3.1 illustrate that the extended Finnis-Sinclair is an excellent choice for modelling swift heavy ion irradiation. The main inaccuracy comes from an overestimation of the melting temperature and the latent heat of melting, thus any damage distribution obtained with this potential will be slightly underestimated in comparison to experiment. The same properties for tungsten are contained in table 3.2. Again, the bulk properties are in general very good, but now there is a quite a significant overestimation in the melting temperature. Thus defect thresholds obtained with this potential are expected to be higher in experimental samples.

	a (Å)	E_c (eV)	E_v^f(eV)	C_{11} (MBar)	C_{12}	C_{44}	T_m (K)	L_m (kJ mol^{-1})
Pot	3.160	8.916	3.71	5.31	2.06	1.626	4500	29.71
Exp	3.16	8.90	3.95	5.32	2.04	1.631	3700	35.40

Table 3.2: Bulk properties of tungsten calculated using the extended Finnis-Sinclair potential. a is the lattice parameter, E_c is the cohesive energy, E_v^f is the vacancy formation energy. C_{11}, C_{12}, and C_{44} are elastic constants, T_m is the melting temperature, and L_m is the latent heat of melting. The first line illustrates the bulk properties obtained with the potential, and the second line is the corresponding experimental results. All values are taken from the original paper [106].

3.1.2 Swift heavy ion irradiation of body-centred cubic metals

3.1.2.1 Simulation setup

The iron simulation cell was constructed from a two atom basis, and multiplied by 140x140x60 in the x, y, and z directions, resulting in a 2,352,000 atom cell. This cell was initially equilibrated using an NPT ensemble, at 300 K, and 1 atm for 200 ps. This ensured the equilibrium structure was obtained, with resulting cell dimensions of approximately 401x401x172 $Å^3$, with periodic boundary conditions. For the 2T-MD implementation the lattice was discretised into coarsed grained ionic temperature cells (CIT), each with a volume of roughly 1000 $Å^3$, resulting in 40x40x17 CIT cells. The coarse grained electronic temperature cells (CET) had the same dimension, but extended three times further in the x and y directions, thus the number of CETs was 120x120x17. The extension of the CET cells beyond the CIT cells provides a mechanism for the transport of electronic energy out of the central cell. As the swift heavy ion travelled perpendicularly through the centre of the cell, electronic energy was confined via Neumann boundary conditions in the z-direction. The halo region of the extended electronic cells in the x and y direction were governed by Robin's boundary conditions which converged to 300 K. A variable timestep was chosen for the electronic finite difference solver (determined by the Fourier mesh number), and 1 fs timestep was chosen for the molecular dynamics timestep. The simulations were run for between 150 and 200 ps, long enough to ensure the defect distribution had reached a steady state.

The same approach was taken for tungsten, with the exception that the relaxed cell dimensions were approximately 441x 441x189 $Å^3$ and the resulting number of CIT and CET were 44x44x19 and 132x132x19 respectively. Unfortunately due to the extreme computational nature of the simulations (which took more than 8 days on 40 cores with 64 GB of RAM), repeated simulations for accurate statistics was not possible. However, the number of particles (2.4 million), and the dimensions of the cell, mean that each run was similar to doing repeated simulations of a typical 100,000 atom cell. A large cell was chosen (over repeated simulations with a smaller cell) to accurately allow more complex defect distributions (such as dislocation loops) to form.

3.1.2.2 Temperature evolutions

The time evolution of the local lattice and electronic temperatures at the centre of the bcc simulation cells during a 60 keV/nm SHI irradiation are illustrated in figure 3.5.

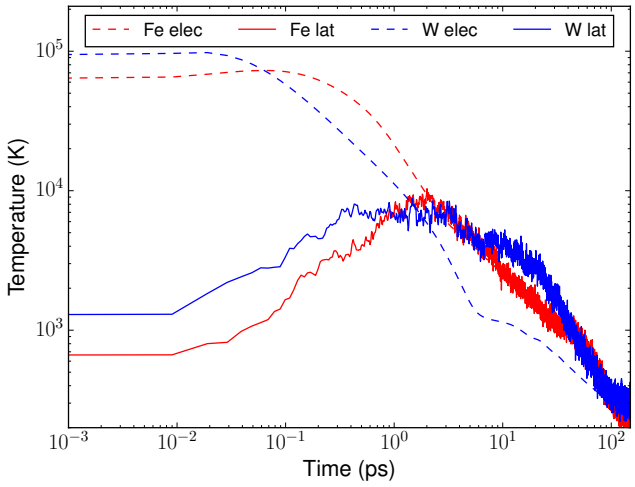

Figure 3.5: Evolution of the electronic and lattice temperatures at the centre of an iron and tungsten cell irradiated by a 60 keV/nm SHI. The electronic temperatures are denoted by a dashed line, and the lattice temperatures by a solid line.

As iron has the larger specific heat, it attains a lower peak electronic temperature compared to tungsten. At these extremely high levels of electronic excitation, both the electron-phonon coupling strength and electronic diffusivity of tungsten is greater than in iron, thus the rate of electronic temperature dissipation is larger in tungsten for the first picosecond. After 1 ps this trend reverses, resulting in a similar time at which the lattice and electronic equilise for both metals. The initial lattice temperatures of tungsten established immediately after the SHI irradiation is higher than in iron (due to the smaller electronic specific heat). It is interesting to note how the interatomic potential properties (notably the interplay of the lattice thermal conductivity and specific heat) result in the rate of change of lattice temperature to be greater in iron than in tungsten. Both metals also reach roughly the same peak lattice temperature. The most pronounced difference between the dynamics of these two metals comes after the lattice and electronic temperatures first equalise. In the

case of iron, once they meet they stay equilibrated, and begin to cool down to the ambient background temperature. Tungsten is significantly different, as the extremely high electronic diffusivity causes the electronic temperature to fall below the lattice temperature, eventually equilibrating after roughly 80 ps.

Figure 3.6 illustrates the signficant differences in the cross sectional electronic temperatures of iron and tungsten at various times during a SHI irradiation event. In both cases an initial electronic temperature spike in the centre begins to spread throughout the cell via diffusion, while energy also transfers to the lattice via electron-phonon coupling. The most striking difference observed is due to the significantly higher electronic diffusivity of tungsten. It is so high that energy diffuses to the edges of the cell quickly, while also resulting in the temperature at the centre of the cell to be lower in comparison to the same region in iron. Interestingly, despite these extreme differences in the electronic temperature profiles, the corresponding lattice temperature cross-sections, shown in figure 3.7 end up being remarkably similar. This is due to a combination of the differences in the thermal properties of the lattice (the specific heat and thermal conductivity) and the electron-phonon coupling. It is clear from figure 3.7 that the difference in the melting temperatures of each material will be a key factor in determining how damaged each cell will be. Despite the similar lattice temperature profiles, a much wider region of the iron cell exceeds this melting temperature, also for a more sustained period of time. At 20 ps about 20 nm of the iron cell is close to the melting temperature, only 5 nm of the corresponding tungsten cell is close to the melting temperature. Thus from these results it is expected that tungsten will be significantly more resistant to SHI radiation damage than iron.

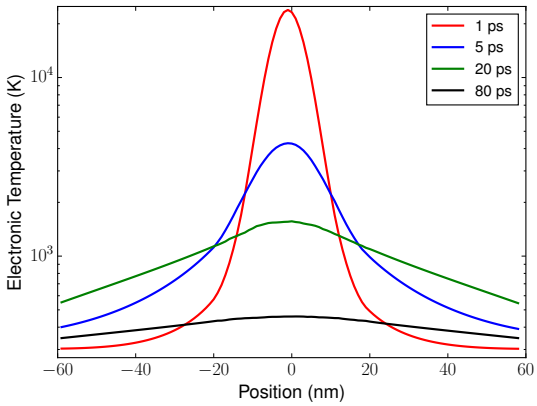

(a) Iron

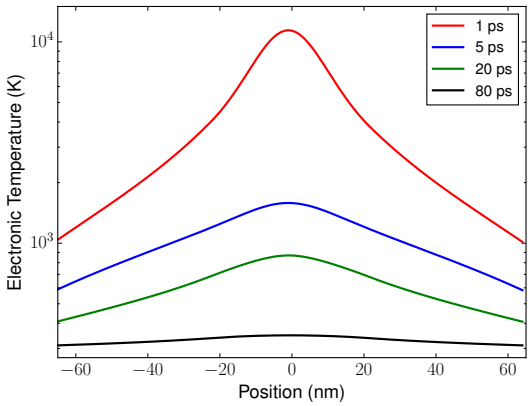

(b) Tungsten

Figure 3.6: Cross-section of electronic temperatures in bcc metals at various times during a 60 keV/nm SHI event.

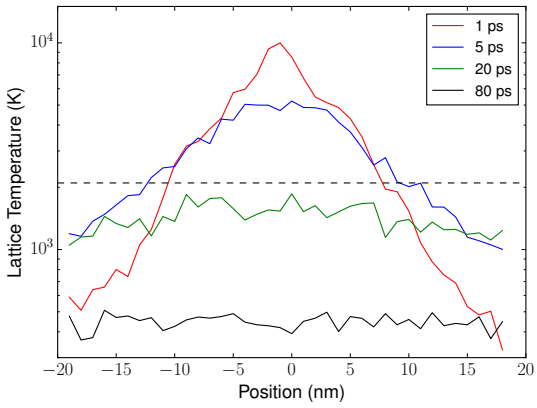

(a) Iron

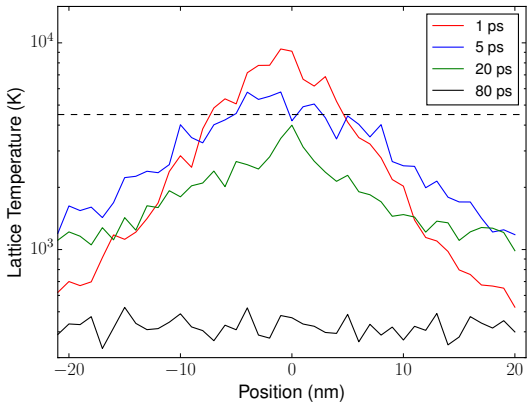

(b) Tungsten

Figure 3.7: Cross-section of lattice temperatures in bcc metals at various times during a 60 keV/nm SHI event. The dashed horizontal line illustrates the melting temperature of each respective interatomic potential.

3.1.2.3 Defect evolutions

A side and top profile view of defect creation and evolution in iron following a 60 keV/nm SHI irradiation event are illustrated in figure 3.8 and figure 3.9, respectively. 10 ps after irradiation a large molten region is established at the centre of the cell. As the melt front in the simulation proceeds to recrystallise, a halo of vacancies form. There are also a small number of isolated interstitial clusters in this halo region. This halo of defects leads to an imbalance in the number of available lattice sites at the central region of the cell, resulting in an excess of atoms, and thus the formation of a column of interstitial clusters. As the lattice begins to cool towards ambient temperatures these interstitial clusters form edge dislocation loops with Burgers vectors of orientation $\mathrm{b} = \frac{1}{2}\langle 111\rangle$ and $\mathrm{b} = \langle 100\rangle$. The total length of dislocations with $\mathrm{b} = \frac{1}{2}\langle 111\rangle$ is 336 Å, and for $\mathrm{b} = \langle 100\rangle$ this length is 106 Å. The most significant deviation between the WS and dislocation images is at 10 ps, there appears to be an anomalous distribution of defects outside of the central cylinder in the WS images. This is due to reflection of a pressure wave created following SHI irradiation. This non-physical artefact significantly skews the WS defect distributions in the beginning period of the simulation. It is discussed in more detail later.

Figure 3.8 and figure 3.9 emphasise a significant property of defect formation due to SHI irradiation in metals. The majority of the initially formed amorphous region in a metal ends up recrystallising, with a few defect clusters and isolated defects remaining. Thus it fair to say that ion tracks formed in metals are totally different to the ion tracks formed in band gap materials, as the defect distribution that remains is not a cylindrical amorphous region adjacent to the ion tracks path. It also stresses a number of significant advantages in employing the 2T-MD model over the regular two-temperature model. The two-temperature model assumes that any region that exceeds the melting temperature forms an ion track. This continuous ion track does not form in Fe. Also, the ability to observe complex defect structures like dislocation loops is impossible without the availability of full atomistic detail.

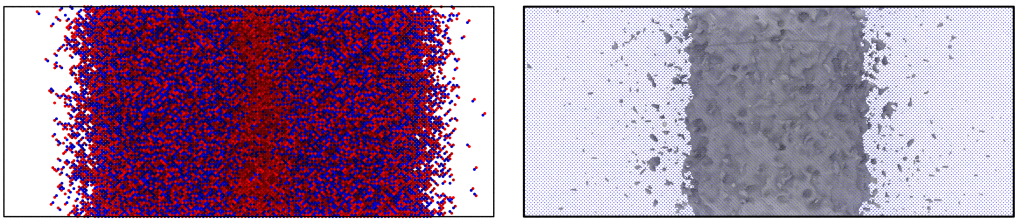

(a) 10 ps (b) 10 ps

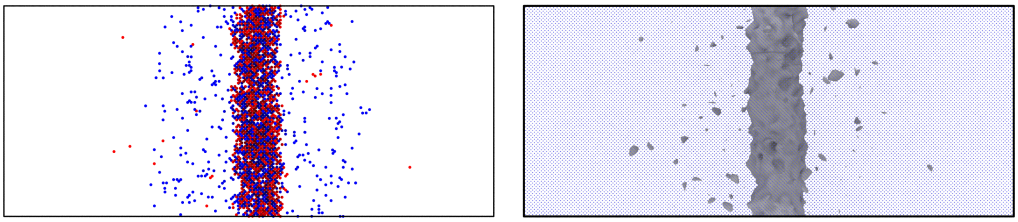

(c) 30 ps (d) 30 ps

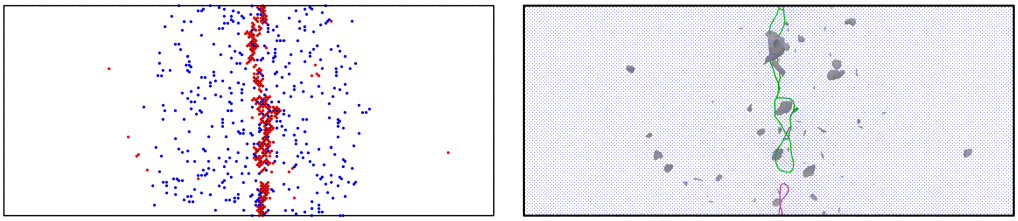

(e) 50 ps (f) 50 ps

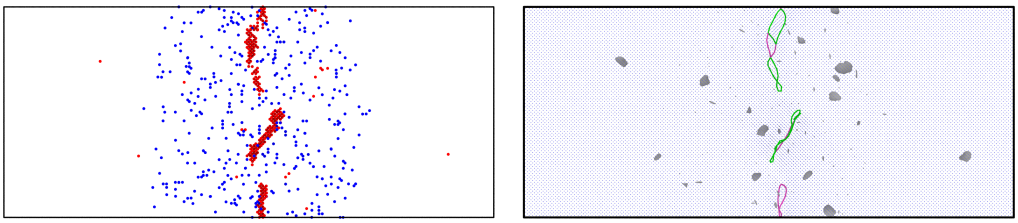

(g) 150 ps (h) 150 ps

Figure 3.8: Side profile of defect evolution in Fe during a 60 keV/nm simulation. The left column illustrates Wigner-Seitz defect evolution, with red particles representing interstitials and blue particles vacancies. The right column shows dislocation loop creation (the green loops are $b = \frac{1}{2}\langle 111 \rangle$ and red are $b = \langle 100 \rangle$). The dark grey regions are a regions which deviate from the perfect lattice. The width and height of these images correspond to 441 Å and 189 Å respectively.

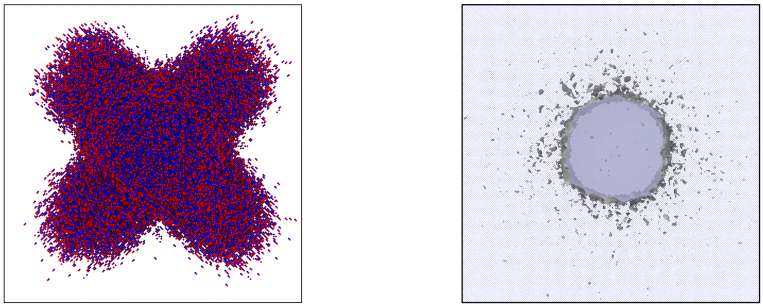

(a) 10 ps

(b) 10 ps

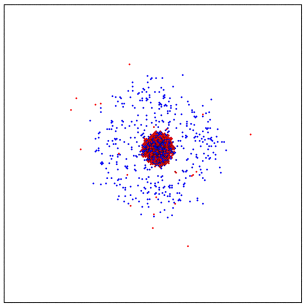

(c) 30 ps

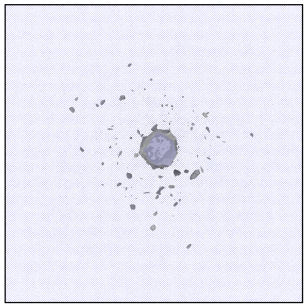

(d) 30 ps

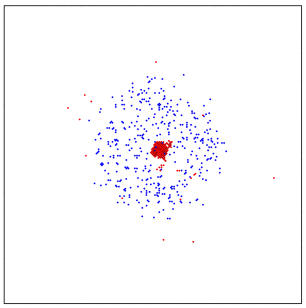

(e) 50 ps

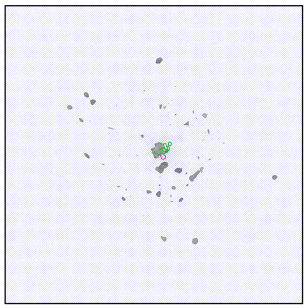

(f) 50 ps

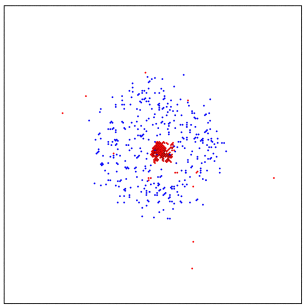

(g) 150 ps

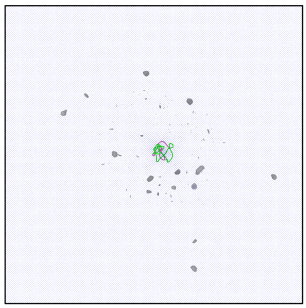

(h) 150 ps

Figure 3.9: Top profile of defect evolution in Fe during a 60 keV/nm simulation. The left column illustrates Wigner-Seitz defect evolution, with red particles representing interstitials and blue particles vacancies. The right column shows dislocation loop creation (the green loops are $\mathrm{b} = \frac{1}{2}\langle 111 \rangle$ and red are $\mathrm{b} = \langle 100 \rangle$). The dark grey regions are a regions which deviate from the perfect lattice. The width and height of these images correspond to 441 Å respectively.

The formation of dislocation loops in iron has been verified in pure polycrystalline Fe irradiated with C60 fullerenes [15]. C60 fullerenes are capable of attaining much higher electronic stopping powers when compared to traditional monatomic swift heavy ions. The work notes that dislocation loops in Fe exhibit several different shapes, including two quasi-parallel dislocation lines joined near the surface. The right hand column of figure 3.8 shows a strikingly similar structure. As the amorphous core begins to recrystallise a number of dislocations loops form, all of which are quasi-parallel to the direction of travel of the SHI. This is an important result, as dislocation loops of this type can, over time, lead to swelling, a loss in ductility, and an increase in hardness. Interestingly, experiments involving cascade damage in iron show similar features. Yao *et al* [123] showed that when thin foils of Fe were bombarded with 150 keV Fe^+ ions at an irradiation temperature of 300 K, interstitial dislocation loops with $b = \frac{1}{2}\langle 111\rangle$ and $b = \langle 100\rangle$ formed. When the irradiation temperature was increased to 500 K, only loops with $b = \langle 100\rangle$ formed. This result has also been validated via other types of radiation damage experiments at various other temperatures [124]. Another piece of research verifies that for electronic stopping powers under 40 keV/nm damage observed in Fe is lower than corresponding cascade experiments, but above this threshold the material begins to undergo significantly more damage than at any other previous stopping power [18].

The next logical question to address is whether or not a similar defect evolution occurs in tungsten. Figure 3.10 highlights the similarities and differences. Both the WS and dislocation analysis show a similar defect geometry, but quite clearly there are significantly fewer defects. Figure 3.10 (c) illustrates the time evolution of WS defects in both bcc metals. Throughout the entire simulation there is an order of magnitude of difference in the number of WS defects created in tungsten. Due to tungsten's much larger diffusivity, the final defect distribution is established 10 ps faster than in iron. This evolution also illustrates how significant defect recombination is in both these metals. Like iron, tungsten also exhibits the creation of both $b = \frac{1}{2}\langle 111\rangle$ and $b = \langle 100\rangle$ loops, although of a smaller length. The total length of dislocations with $b = \frac{1}{2}\langle 111\rangle$ is 135 Å, and for $b = \langle 100\rangle$ this length is 33 Å. The formation of dislocation loops agrees with a cascade experiment carried out by Yi *et al* [125], however that experiment also found that vacancy dislocation loops were also formed (at roughly an equal ratio to interstitial dislocation loops).

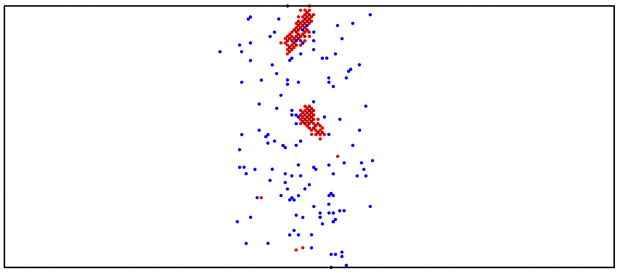

(a) 80 ps WS image

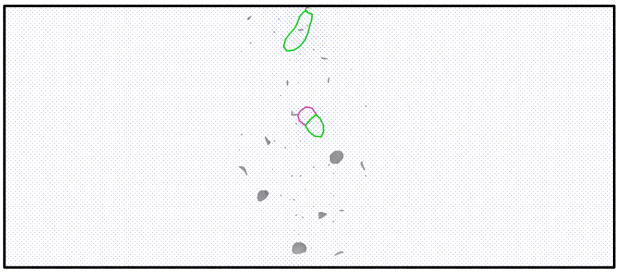

(b) 80 ps dislocation image

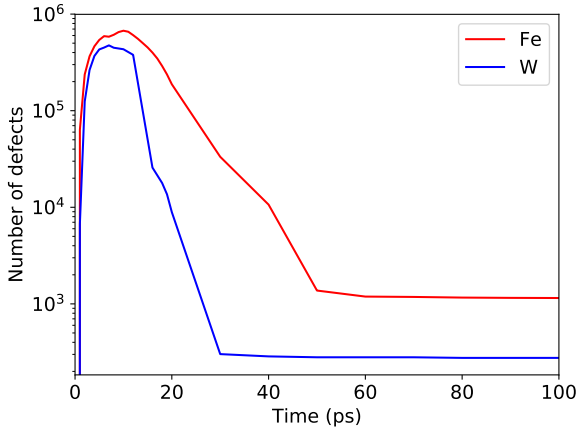

(c) WS defects vs time in both iron and tungsten.

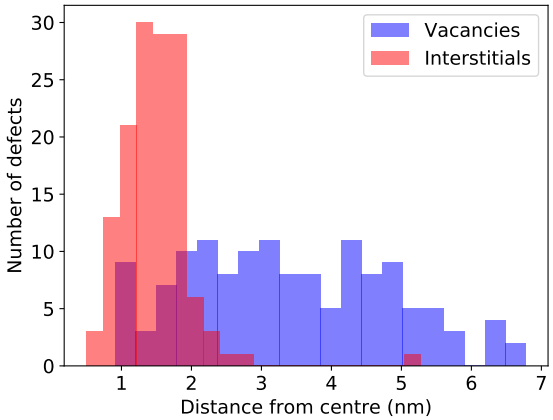

(d) Occupancy vs distance from centre of cell in a 60 keV/nm W simulation.

Figure 3.10: (a) and (b) demonstrate the final defect distribution in tungsten following a 60 keV/nm SHI simulation. (a) illustrates Wigner-Seitz defect evolution, with red particles representing interstitials and blue particles vacancies. (b) shows dislocation loop creation (the green loops are b = $\frac{1}{2}\langle 111\rangle$, red are b = $\langle 100\rangle$). The dark grey regions are a regions which deviate from the perfect lattice. (c) illustrates the time evolution of WS defects in both bcc metals. (d) emphasises the defect morphology in bcc metals, a halo of isolated vacancies surrounding clusters of interstitials.

Unfortuntately, there simulated defect distributions observed in figure 3.10 do not agree quite as well with one SHI experiment in W. This recent work by Dube *et al* [17] found that the defect clusters formed in pure polycrystalline W when irradiated by 120 MeV Au^{+7} ions, however the clusters formed were vacancies. This was achieved by measuring positron

annihilation times, a time which will strongly depend on the local electron density. After irradiation this annihilation time increased, indicating that the electron density decreased, ie - vacancy defects formed. However, it is worth nothing that the pure polycrystalline tungsten did have significant vacancy defects present before irradiation. Thus it is possible that the defects present significantly influenced the creation of vacancy clusters after irradiation.

Older work carried out by Dunlop *et al* [16] found tungsten to be completely defect free following irradiation by 4.9 GeV lead ions (corresponding to an electronic stopping power of approximately 70 keV/nm). However, there was one key difference between this experimental work and the simulations here. The experiment was conducted at temperatures between 15 K and 25 K, and at these low temperatures tungsten has an even higher thermal conductivity. It is approximately 4000 $Wm^{-1}K^{-1}$. Figure 3.11 shows the electronic and lattice temperature evolutions at the centre of a W cell equilibrated at 20 K, and subject to an intense SHI irradition of 100 keV/nm. From this graph it is easy to see why tungsten was resistant to defect formation at this temperature. The huge electronic thermal conductivity forces energy to dissipate so quickly through the electronic system that no significant energy is transferred to the lattice. The peak lattice temperatures are several thousand degrees under the melting temperature, and the system equilibrates within 12 ps (far faster than for the room temperature case).

Thus far it has been observed that both iron and tungsten disorder significantly when irradiated by high energy swift heavy ions. The general distribution is that of a cloud of isolated vacancy defects, and clusters of insterstitials along the trajectory of the SHI. Both show the formation of interstitial loops with Burger's vectors $b = \frac{1}{2}\langle 111\rangle$ and $b = \langle 100\rangle$. Tungsten is significantly more resistant to damage than iron. However a more quantitative analysis and comparison of the defect distributions in both metals at various swift heavy ion irradiation energies is required.

Figure 3.12 highlights the sensitivity of each metal to defect creation at various swift heavy ion irradiation energies. (a) shows the number of Wigner-Seitz defects created in both metals at stopping powers ranging between 10 keV/nm and 100 keV/nm, and clearly demonstrates various consistent features. A small number of defects are created in iron at S_e as low as 10 keV/nm, whereas defects are not created in tungsten until somewhere between 30 keV/nm and 40 keV/nm. In both metals the number of WS defects increases linearly with increasing

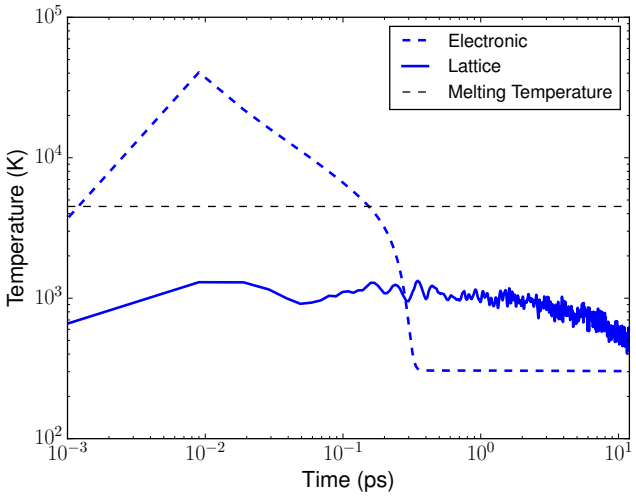

Figure 3.11: Graph of temperature evolutions at the centre of a tungsten cell at 20 K, following irradiation by a SHI with an electronic stopping power of 100 keV/nm. The blacked dashed line represents the melting temperature for the interatomic potential.

S_e.

Figure 3.12 (b) and (c) show the evolution of dislocation loop lengths in iron and tungsten, respectively, for the same electronic stopping powers. It is interesting to note in iron, the small amount of damage created in the 10 keV/nm simulation was completely made of point defects, as no dislocation loops are formed. At 20 keV/nm both $b = \frac{1}{2}\langle 111\rangle$ and $b = \langle 100\rangle$ dislocation loops form. In tungsten, the first stopping power where dislocations loops are observed is at 40 keV/nm, and this consists only of a dislocation with Burger's vector $b = \frac{1}{2}\langle 111\rangle$. There appears to be quite a complex dependence on the length of dislocations and electronic stopping power in both metals. However, this is more than likely due to only one simulation being possible for each stopping power. A general trend does emerge though, the total dislocation loop length tends to increase with increasing stopping power, with a larger proportion of $b = \frac{1}{2}\langle 111\rangle$ over $b = \langle 100\rangle$ dislocation loops. This agrees with previous literature studies, where continuum elasticity estimates show that the $b = \frac{1}{2}\langle 111\rangle$ loop is more energetically favourable, explaining its dominance [126].

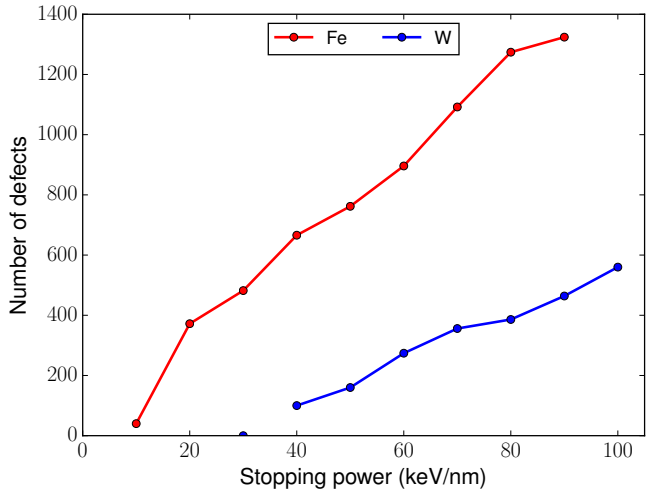

(a) Defect creation sensitive to electronic stopping power for both bcc metals. No defects are created in tungsten at 30 keV/nm.

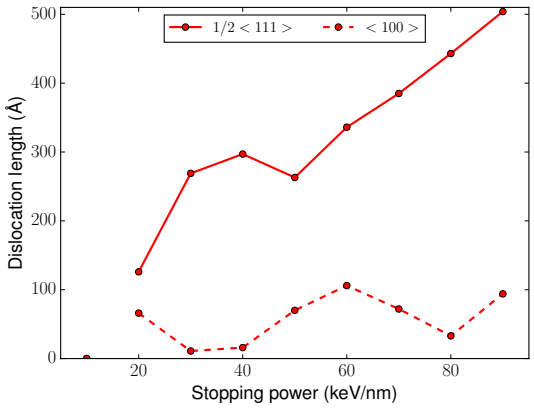

(b) Dislocation loop length in iron vs S_e.

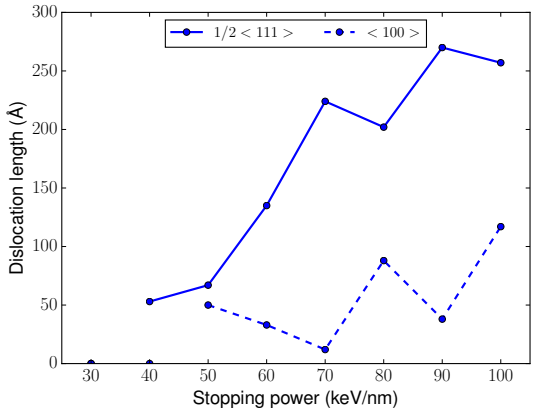

(c) Dislocation loop length in tungsten vs S_e.

Figure 3.12: The sensitivity of defect creation in bcc metals at various electronic stopping powers. (a) shows the number of WS defects vs stopping power for both iron and tungsten. (b) shows the the length of dislocations loops found in iron at various S_e. (c) shows the the length of dislocations loops found in tungsten at various S_e. There is a clear trend for defects to increase with increasing stopping power. The total dislocation loop length in general increases also, but there is a more complex interdependence on the evolution of each type of dislocation loop with increasing stopping power.

This synergy was observed in a number of simulations, as dislocation loops with b = ⟨100⟩ are never observed on their own, they only form in-between two b = $\frac{1}{2}$ ⟨111⟩, or connected to a single b = $\frac{1}{2}$ ⟨111⟩ loop. Similar observations were concluded by Marian *et al* [126], where the formation of ⟨100⟩ only occurs due to the overlap of two $\frac{1}{2}$ ⟨111⟩ loops. The emergence and growth of a ⟨100⟩ between two interacting $\frac{1}{2}$ ⟨111⟩ loops (which subsequently get smaller) is shown in figure 3.13.

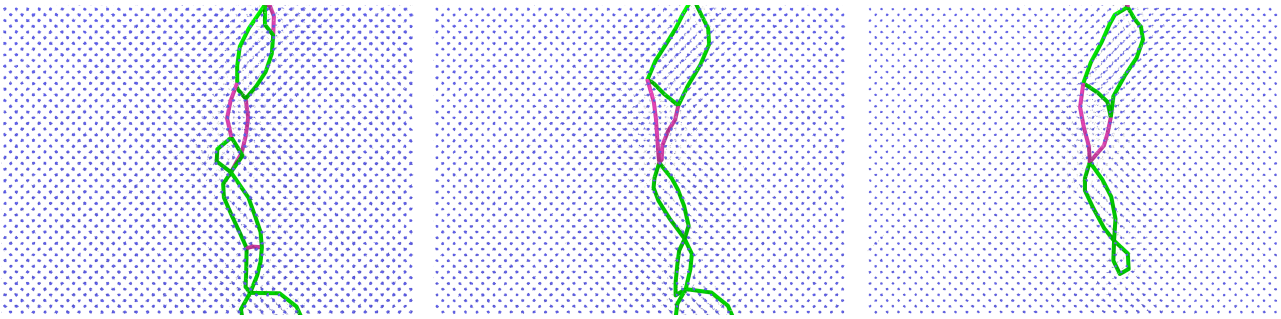

(a) 50 ps (b) 60 ps (c) 150 ps

Figure 3.13: A side profile view of the growth of a ⟨100⟩ (in red) loop at the expense of two $\frac{1}{2}$ ⟨111⟩ (in green) during a SHI irradiation of iron. A small ⟨100⟩ loop is observed at 50 ps, 10 ps later this loop is larger. At 150 ps the ⟨100⟩ is clearly seen to grow even more, while the $\frac{1}{2}$ ⟨111⟩ loop below has significantly reduced in size.

There exists a potentially significant non-physical artefact in all of these simulations due to the lattice cell sizes available for study. As a cell extended in the z-direction in desirable to obtain adequate damage statistics, the lengths in the x and y are somewhat compromised. Thus during a simulation the pressure wave created following irradiation spreads outwards and ends up reflecting back to the centre. In reality this pressure wave would dissipate into the bulk. This reflected pressure wave at the beginning of each simulation causes areas of the simulation cell to undergo larger displacements than usually expected, so defect statistics are exaggerated in the first picoseconds. Figure 3.14 illustrates this effect, a defect distribution in the shape of an 'X' is formed, when in reality only the cylindrical core should be defect rich.

To mitigate this effect, another iron cell was tested containing the same number of atoms, but with dimensions of 802x802x43 $Å^3$. This cell, greatly extended in the x and y-directions,

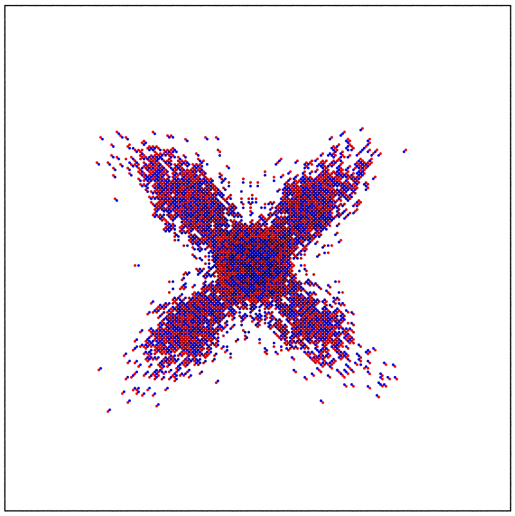

Figure 3.14: Image of the WS defect distribution at 15 ps in a 60 keV/nm irradiation of tungsten. The reflected pressure wave causes an 'X' like distribution of defects to form.

exhibited a similar reflected pressure wave, and also the same defect distributions described so far. Thus with current computational power, this non-physical effect can not be overcome by simply increasing the x and y directions of the simulation cell. However, this may be overcome by applying a pseudo-thermostat/barostat at the lattice boundary, and is something to look into in the future.

3.2 Face-centred cubic metals

The two face-centred cubic metals chosen for investigation are nickel and copper. Nickel has been shown to be extremely resistant to damage formation following swift heavy ion irradiation, and while copper has very similar bulk properties, the electronic systems are significantly different to warrant an in depth comparison.

3.2.0.1 Electronic system

The key parameters that govern the electronic subsystem for nickel and copper are derived in the exact same way as outlined in section 3.1.1.1. The electronic specific heat for both metals

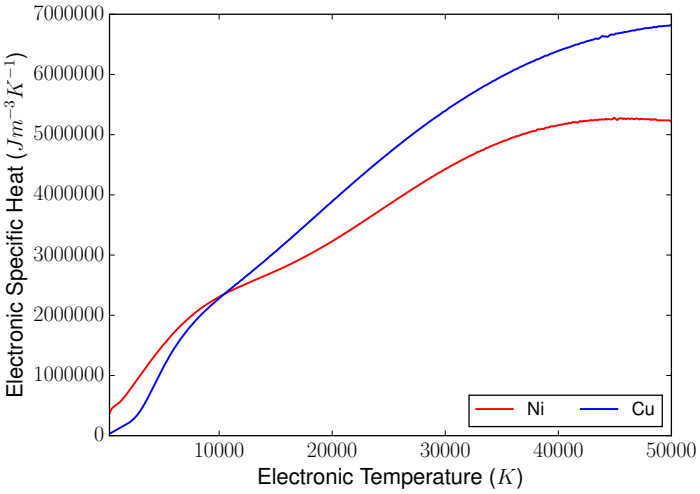

Figure 3.15: Graph of the electronic specific heat capacity vs electronic temperature for nickel and copper. Data reproduced from the work of Lin *et al.* [44]. The electronic specific heat of copper is higher than that of nickel for the majority of the electronic temperatures.

is shown in figure 3.15. At low electronic temperatures the specific heats are comparable, with nickel being slightly greater than copper, convergence occurs at about 10 000 K, and they diverge significantly at higher temperatures, with copper having the greater specific heat. This result implies that the initial temperature reached after irradiation for nickel will be substantially higher than copper. A comparison with the bcc metals also yields interesting differences. The gradient of the electronic specifics heats of the bcc metals is larger than that of the fcc metals for the first 10 000 K, the specific heats at high electronic temperatures are lower (especially if comparing tungsten to copper). Thus for large electronic stopping powers, the initial temperatures reached by fcc metals will in general be lower than their bcc counterparts.

The electron-phonon coupling and electron-phonon coupling strength versus electronic temperature for both fcc metals are shown in figure 3.16. At low temperatures the electron-phonon coupling is more than an order of magnitude greater for nickel than copper, however this decreases quickly, with the values converging at roughly 5000 K. At high temperatures copper has a much higher electron-phonon coupling. The values of these e-p coupling values

are also significantly smaller than the corresponding e-p coupling values for the bcc metals. Thus the electronic and lattice systems of iron and tungsten are more strongly coupled than those of nickel and copper. As mentioned previously, the important quantity for determining the rate of energy exchange between the electrons and lattice is not the e-p coupling, but its ratio with the electronic specific heat. This coupling strength is illustrated in figure 3.16 (b). The most prominent difference is seen in nickel at high electronic temperatures, the coupling strength is an order of magnitude less than any of the other metals studied, such a large contrast would be expected to have a significant impact on the temperature evolution.

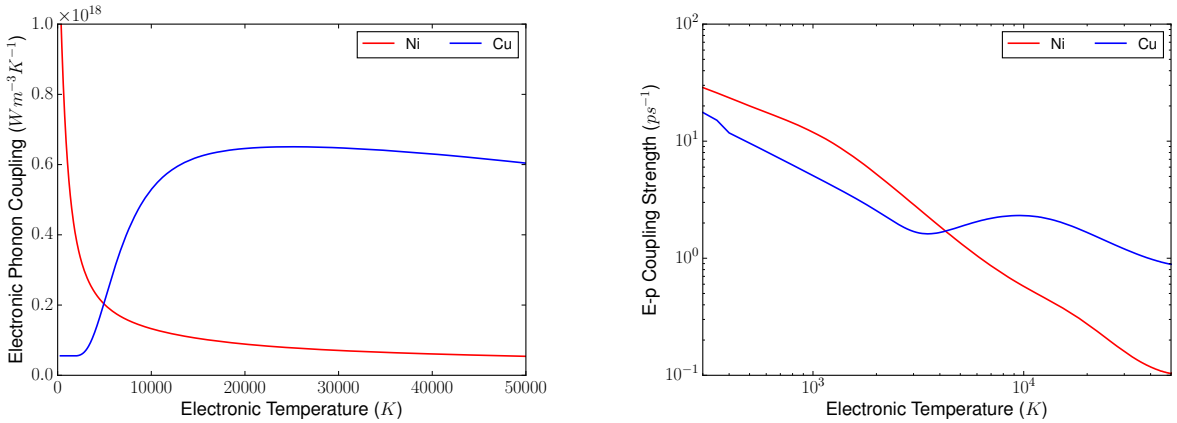

(a) E-p coupling vs electronic temperature for fcc metals. (b) E-p coupling strength vs electronic temperature.

Figure 3.16: Graph of the (a) electronic-phonon coupling vs temperature and (b) e-p coupling strength vs temperature for copper and nickel. The e-p coupling of copper is significantly greater than nickel during significant electron excitation. For the majority of relevant temperatures this is also the case for the inverse relaxation time. At very high temperatures the rate of exchange between the electrons and lattice is greater for nickel.

When the coupling strength is compared with the bcc metals, it is evident that the energy transfer between the two subsystems is much faster for bcc metals than their fcc counterparts (for the relevant electronic temperatures explored during typical SHI irradiations). However it is important to stress again that this does not necessarily indicate whether bcc metals will be more susceptible or resistant to defect creation, as it will depend on the interplay between all of these parameters and the lattice properties.

The final electronic parameters are the thermal conductivity and the analagous diffusivity. Figure 3.17 illustrates the temperature dependences of these quantities. Here copper appears to be special as it has a significantly higher thermal conductivity and diffusivity in comparison to all of the other metals studied. This means that energy will quickly dissipate through the electronic subsystem of copper. Couple this with the smallest initial rise in temperature following irradiation in comparison to the other metals (due to having the largest electronic specific heat), may point towards a resistance to defect creation. This is also dependent on the bulk properties of interatomic potential. It is interesting to note that the rate of energy diffusion in the electronic systems of both nickel and iron are very similar.

3.2.0.2 Interatomic potential properties

The bulk lattice properties of nickel and copper are shown in tables 3.3 and 3.4 respectively, and it is evident that the properties of these fcc metals are more accurate than that of the bcc metals. There is less than a 10% difference the experimental and potential for the majority of the properties. Thus the lattice contribution to defect kinetics is more accurate for these fcc metals. While nickel's associated bulk properties (a higher melting temperature, latent heat of melting, and cohesive energy) suggest it is should be more resistant to defects than copper, the difference is far less prominent than in the case of tungsten and iron. Couple this with the difference in electronic properties : copper having the abnormally high diffusivity, and nickel having an extremely low electron-phonon coupling at excited temperatures, and it is difficult to predict which will be more susceptible to damage.

	a (Å)	E_c (eV)	E_v^f(eV)	C_{11} (MBar)	C_{12}	C_{44}	T_m (K)	L_m (kJ mol^{-1})
Pot	3.520	4.437	1.624	2.450	1.485	1.182	1800	13.74
Exp	3.52	4.44	1.60	2.45	1.40	1.25	1728	17.47

Table 3.3: Bulk properties of nickel using extended Finnis-Sinclair potential. a is the lattice parameter, E_c is the cohesive energy, E_v^f is the vacancy formation energy. C_{11}, C_{12}, and C_{44} are elastic constants, T_m is the melting temperature, and L_m is the latent heat of melting. The first line illustrates the bulk properties obtained with the potential, and the second line is the corresponding experimental results, all values are taken from the original paper [106].

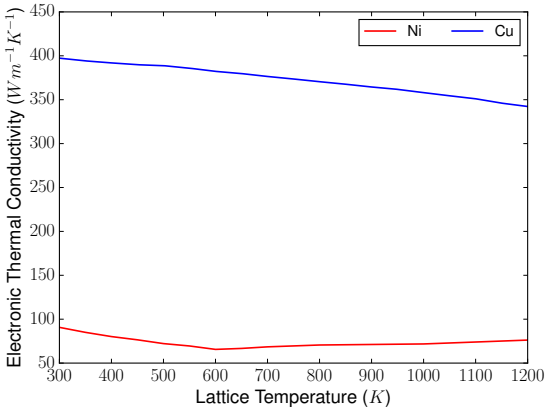

(a) Electronic thermal conductivity vs lattice temperature for fcc metals.

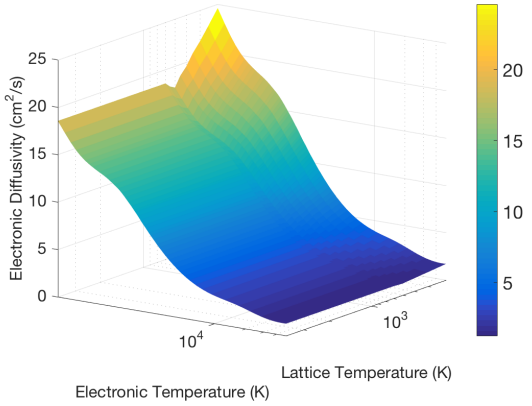

(b) Electronic diffusivity surface vs temperature for nickel.

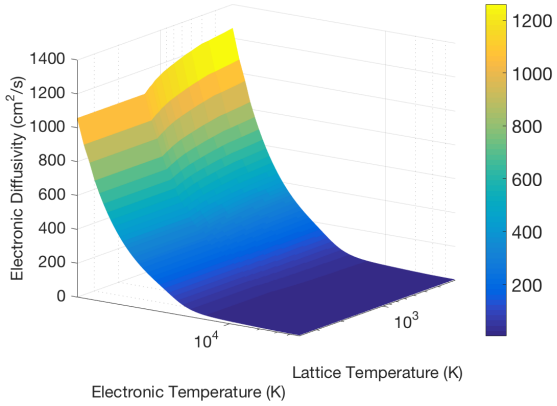

(c) Electronic diffusivity surface vs temperature for copper.

Figure 3.17: Graph of the (a) electronic thermal conductivity vs lattice temperature, (b) electronic diffusivity vs temperature for nickel, and (c) electronic diffusivity vs temperature for copper. The thermal conductiviy and diffusivity of copper for all temperature combinations is significantly larger.

	a (Å)	E_c (eV)	E_v^f(eV)	C_{11} (MBar)	C_{12}	C_{44}	T_m (K)	L_m (kJ mol^{-1})
Pot	3.610	3.490	1.280	1.684	1.214	0.754	1300	9.16
Exp	3.61	3.49	1.28	1.684	1.214	0.754	1358	13.05

Table 3.4: Bulk properties of copper using extended Finnis-Sinclair potential. All parameters are identical to those described in table 3.3.

3.2.1 Swift heavy ion irradiation of face-centred cubic metals

3.2.1.1 Simulation setup

The simulation setup for the fcc metals followed the exact same form as previously described for the bcc metals, with the only differences highlighted in table 3.5.

	Ni	Cu
Number of atoms	2,420,000	2,420,000
MD cell dimension (Å^3)	388x388x176	399x399x181
Number of CIT	39x39x17	40x40x18
Number of CET	117x117x17	120x120x18

Table 3.5: Details of the simulation setup for nickel and copper.

3.2.1.2 Temperature evolutions

The time evolution of the local lattice and electronic temperatures at the centre of the fcc simulation cells during a 100 keV/nm SHI irradiation is illustrated in figure 3.18. Significantly different behaviour is observed when nickel is compared to copper.

Nickel achieves a far higher initial electronic temperature (as it has the lower electronic specific heat), however, at these elevated temperatures the electron-phonon coupling strength is so weak, that none of this energy is transferred from the electrons to the lattice. Thus the energy is allowed to slowly diffuse throughout electronic subsystem (and exit at the boundaries), resulting in the the lattice remaining at ambient temperatures throughout the entirety of the simulation. It takes roughly 40 ps for the electronic and lattice temperatures to first equalise, an order of magnitude greater than in any other metal presented here.

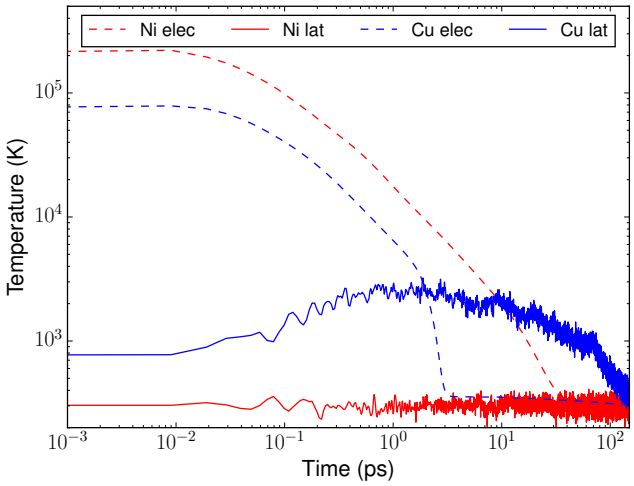

Figure 3.18: Evolution of the electronic and lattice temperatures at the centre of an iron and tungsten cell irradiated by a 100 keV/nm SHI. The electronic temperatures are denoted by a dashed line, and the lattice temperatures by a solid line.

This result ensures that nickel will be completely resistant to SHI damage, even at the most extreme levels of excitation.

Copper, on the other hand, follows a more familiar trajectory. It has the largest electronic specific heat of all the metals studied, so at the extreme electronic stopping powers of 100 keV/nm, it has a peak electronic temperature similar to bcc metals irradiated by 60 keV/nm. The extremely strong diffusivity, alongside an e-p coupling strength comparable with the bcc metals, causes the lattice and electronic temperatures to equalise at roughly 3 ps. The strong diffusivity forces the electron temperature to decrease below the lattice temperature (like in tungsten), and the systems equilibrate after 100 ps. It is worth observing that interatomic properties of copper here cause the peak lattice temperatures to be a few thousand Kelvin lower than the bcc metals. However, copper has a lower melting temperatures (1300 K), so damage may still occur.

Figure 3.19 illustrates the cross-sectional electronic temperature of both metals at various time during a 100 keV/nm irradiation. Nickel has a diffusivity very similar to iron, and a similar electronic temperature distribution is obtained in figure 3.20 (a). In fact, the differences in the electronic distributions between nickel and copper, are extremely similar

to the differences observed between iron and tungsten. The most notable exception is in how quickly the electronic temperature of the copper cell reaches ambient temperature (due to the enormous diffusivity). Figure 3.20 illustrates the corresponding cross-sectional lattice temperatures. Figure 3.20 (a) highlights how the low e-p coupling strength of nickel prevents any transfer of the energy from the electrons to the lattice. Figure 3.20 (b) again looks similar to the temperature distributions in the bcc metals. Thus copper, despite having an extremely large diffusivity, may be susceptible to damage via SHI at extremely large values of electronic stopping power.

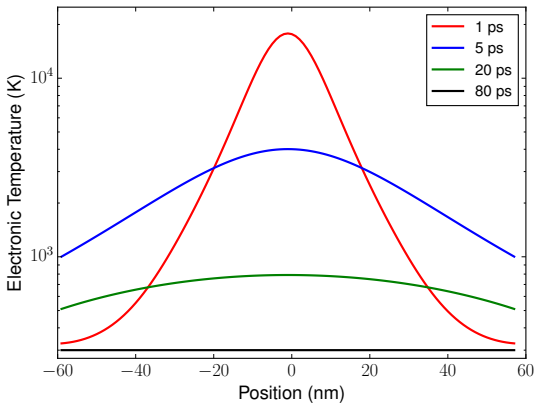

(a) Nickel

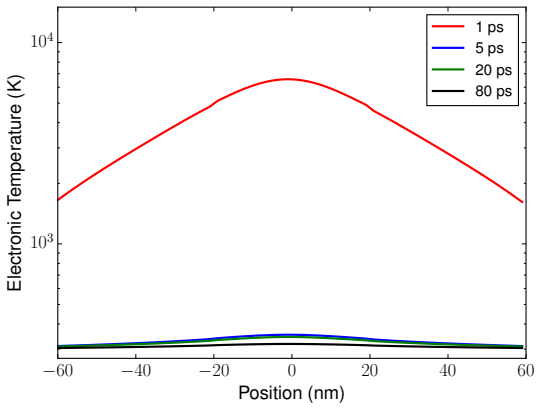

(b) Copper

Figure 3.19: Cross-section of electronic temperatures in fcc metals at various times during a 100 keV/nm SHI event.

3.2.1.3 Defect evolutions

It has already been established that regardless of the energy deposited into the electronic subsystem of nickel, no damage will ensue due to the low rate of transfer between the electrons and the lattice. Thus this section will only focus on defects in copper. Defect formation in copper follows the exact same trajectory as described in the bcc metal section. An initially large molten cylindrical defect distribution is established at the centre of the simulation cell.

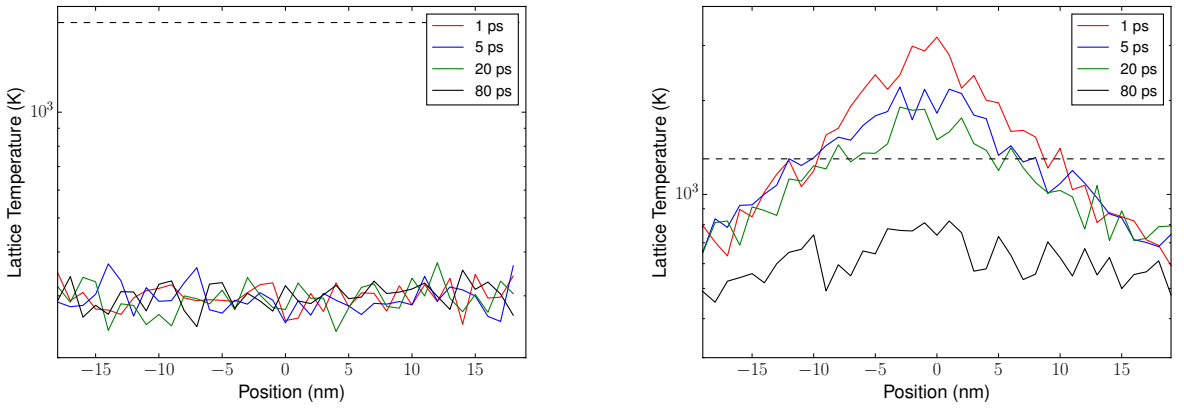

(a) Nickel

(b) Copper

Figure 3.20: Cross-section of lattice temperatures in fcc metals at various times during a 100 keV/nm SHI event. The dashed horizontal line illustrates the melting temperature of each respective interatomic potential.

This begins to cool and recrystallise, during which a number of isolated vacancies form. Thus there are less available lattice sites at the centre of cell, which leads to the formation of small interstitial clusters. These clusters take the form of dislocation loops with various Burger's vectors, including $\frac{1}{6}\langle 112\rangle$ Shockley dislocations, $\frac{1}{6}\langle 100\rangle$ stair-rod dislocations, and $\frac{1}{2}\langle 001\rangle$ Hirth dislocations.

Figure 3.21 illustrates various analyses of this final defect distribution. Figure 3.21 (a) clearly illustrates the halo of isolated vacancy defects, with interstitial clusters at the centre. Figure 3.21 (b) is a dislocation analysis of the same frame, illustrating that the dislocation loops are made up of these interstitial clusters. Figure 3.21 (c) and (d) show a top down view of the same cell. It is obvious that copper is significantly more resistant to radiation damage than either iron and tungsten, as following this 100 keV/nm irradiation only 60 Wigner-Seitz defects remain. An experiment carried out by Paschoud *et al* [127] found the existence of stacking fault tetrahedra, small interstitial clusters and interstitial dislocation loops in copper following irradiation from 230 MeV Ne and 440 MeV Ar ions, however this was due to nuclear stopping, so a comparison is not possible.

The lack of damage observed here in nickel has also agrees well with all experimental data

to date [16, 15]. However, it is worth noting that the reason for this lack of damage disagrees with significant work carried out by Wang *et al* [71]. Wang predicts that copper will be more insensitive to damage than nickel, as nickel has the higher electron-phonon coupling at room temperature. This work proves that this picture is incomplete, as at high levels of electronic excitation the e-p coupling of nickel is so low that it is completely insensitive to any damage.

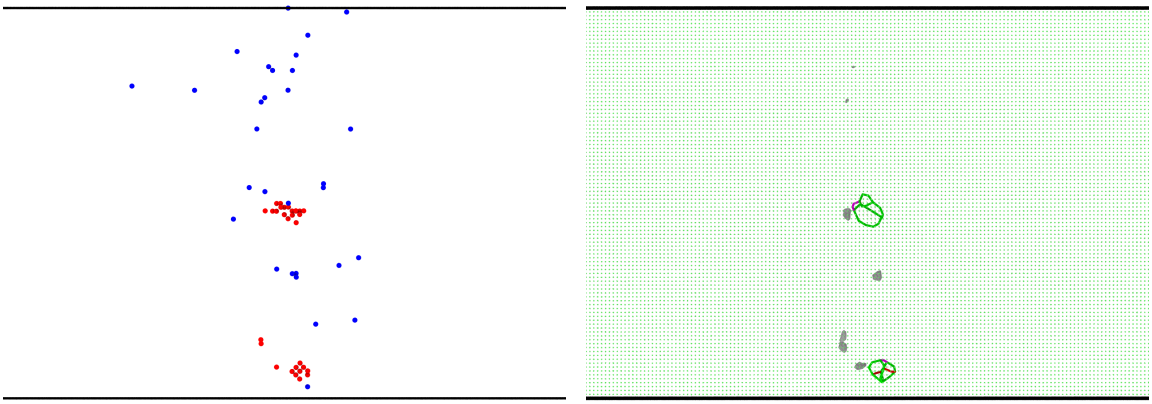

(a) Side profile of Wigner-Seitz defects

(b) Side profile of dislocation loops

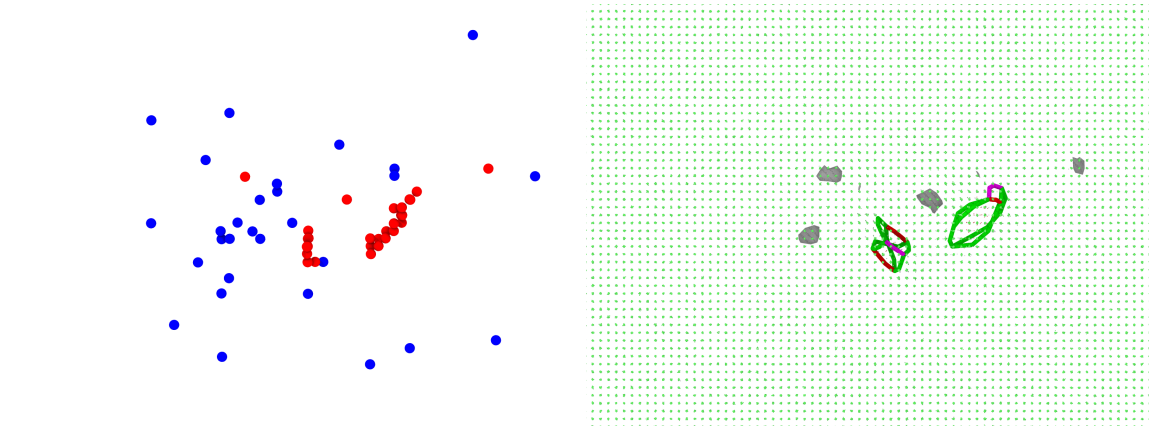

(c) Top view of Wigner-Seitz defects

(d) Top view of dislocation loops

Figure 3.21: Wigner-Seitz images and dislocation loop images of copper after irradiation with a 100 keV/nm SHI. In (a) and (c), the red particles are interstitial defects, and the blue particles are vacancy defects. In (b) and (d), the green represents are Shockley loops, the purple represents Stair-rod loops, and the red represent Hirth loops. The dark grey regions are a regions which deviate from the perfect lattice.

3.2.2 Conclusion and summary

In conclusion, a series of simulations was carried out involving the swift heavy ion irradiation of various bcc and fcc metals. The 2T-MD model was utilised, as the parameterisation of the electronic system is excellent, and access to atomistic detail allows for the visualisation of complex defect kinetics. In the case of the bcc metals, tungsten is far less susceptible to damage than iron, due to the bulk properties of the lattice. However, when damage occurs, it follows the same distribution in both metals. Due to the significant proportion of recrystallisation in metals following swift heavy ion irradiation, damage in bcc metals consisted of a halo of isolated vacancy defects, with multiple clusters of interstitials at the centre. This significant level of recrystallisation also implies a significant deviation in the morphology of ion tracks formed in metals and band gap materials. The interstitial clusters took the form of dislocation loops, and two kinds were observed, those with Burger's vectors b $= \frac{1}{2}\langle 111\rangle$ and b $= \langle 100\rangle$. These dislocation loops have been verified in a previous experiment in which polycrystalline Fe was irradiated by C60 fullerenes [15]. An experiment conducted in tungsten [16] found it to be completely defect free following irradiation. This deviation was also explainable by the model, as the experiment was carrier out at extremely low temperatures. At these temperatures the thermal conductivity was so high that damage was prevented.

Two fcc metals were also investigated, nickel and copper. Both of these metals proved to be far more resistant to damage than either of the bcc metals. Nickel was shown to be completely defect free up to extremely high levels of electronic excitation. This is due to the fact that at high level of electronic excitation, the electron-phonon coupling of the material is so low that energy is essentially prevented from transferring between the electrons and lattice. This was also verified experimentally [15]. Copper was also extremely resistant to damage, albeit less so than nickel. Copper formed a small number of defects at the highest levels of electronic excitations studied. The damage distribution followed a similar geometry to iron and tungsten, a halo of isolated vacancy defects, with small clusters at the centre of the cell. These clusters took the form of dislocation loops with various Burger's vectors, including b $= \frac{1}{6}\langle 112\rangle$ Shockley dislocations, b $= \frac{1}{6}\langle 100\rangle$ stair-rod dislocations, and b $= \frac{1}{2}\langle 001\rangle$ Hirth dislocations.

An important point to take away from this work is that damage in metals is highly com-

plex interdependence of the models electronic and lattice parameters. It is only by running simulations can it be verified that one particular parameter is the driving force behind damage resistance / susceptibility. Also, despite the model reproducing experiments very well, there are still a number of significant improvements to be investigated in the future. The first is in the implementation of a more sophisticated energy deposition distribution. A Gaussian distribution in space, and exponential distribution in time are good initial estimates. However, a more robust and physical description of the excitation of the electronic system directly after swift heavy ion irradiation will ensure more accurate results. A more in depth analysis of the reflected pressure wave is also required. While it is not expected to change the results significantly, it would be important to quantify how big an influence it has on defect creation here. Another improvement on the model could be made by incorporating a more thorough treatment of the electronic thermal conductivity. This will be quite a difficult task, as a physically realistic interpretation will require lattice temperature dependences (up to the thousands of Kelvin), and electronic temperature dependences (up to hundreds of thousands of Kelvin). The final way in which the model could be improved is by incorporating electronic temperature dependent interatomic potentials. However, these have only been parameterised for a few materials, and will be investigated for tungsten later in this thesis.

Despite these limitations, it is not controversial to say that the results presented in this chapter are a significant positive endorsement for the utilisation of the 2T-MD model in describing electronic excitation in metals.

4

Swift heavy ion irradiation of silicon (i)

> "The transistor will almost certainly stimulate greater changes in commerce and industry than reaction motors, synthetic fibres, or even perhaps, atomic energy."
>
> Mervin Kelly

Swift heavy ion (SHI) irradiation of materials is often modelled using the two-temperature model. While the model has been successful in describing SHI damage in metals, it fails to explicitly account for the presence of a bandgap in semiconductors and insulators. The aim of this chapter is to investigate a method which can overcome this limitation. It involves incorporating the influence of the bandgap in the parameterisation of the electronic specific heat for Si. The specific heat as a function of electronic temperature is calculated using finite temperature density functional theory with three different exchange correlation functionals, each with a characteristic bandgap. These electronic temperature dependent specific heats are employed with two temperature molecular dynamics to model ion track creation in Si. The results obtained using a specific heat derived from density functional theory showed dramatically reduced defect creation compared to models that used the free electron gas specific heat. As a consequence, the track radii are smaller and in much better agreement with experimental observations. A correlation is also observed between the width of the band gap and the track radius, arising due to the variation in the temperature dependence

of the electronic specific heat.

4.1 2T-MD model parameters for silicon

Silicon is one of the most obvious choices for a SHI investigation of band gap materials. This is due to it being by far the most studied band gap material, thus a rich literature exists to aid in an accurate parameterisation of the electronic and lattice subsystems.

4.1.1 Electronic system

The key parameters that determine the temperature evolution of the electronic subsystem are the electronic diffusivity (when the material in question is a band gap materials), (D_e), the electronic specific heat capacity, (C_e), the electron-phonon coupling, G_e, and deposition profile of the incoming SHI, A. The biggest hurdle in utilising the 2T-MD model arises from a lack of depth in knowledge about one or many of these parameters. While this parametrisation is far less complete for silicon when compared to the metals investigated previously, it is still the best possibly parameterised band gap material to date. It is again worth recasting the electronic heat diffusion equation in a way that clearly illustrates how the parameters that follow influence electronic temperature evolution.

$$\frac{\partial T_e}{\partial t} = \underbrace{D_e(T_e)}_{(a)} \nabla^2 T_e - \underbrace{\frac{G_e}{C_e(T_e)}}_{(b)} (T_e - T_i) + \underbrace{\frac{A(r,t)}{C_e(T_e)}}_{(c)}, \tag{4.1}$$

The fundamental idea underpinning the physics investigated in this chapter is this ; via an accurate parameterisation of the electronic specific heat capacity of a band gap material, the regular 2T-MD model, which does not contain any explicit terms to account for carrier dynamics, is capable of realistically simulating said material. The electronic temperature dependent electronic specific heat capacity was found via finite temperature DFT using the Vienna Ab-initio Simulation Package software package (VASP) [128]. Simulations employed the semilocal Generalised Gradient Approximation (GGA) functional of Perdew, Burke, Ernzerhof (PBE) [115], and the hybrid Heyd, Scuseria, and Ernzerhof (HSE) [117] and Perdew, Burke, Ernzerhof (PBE0) functionals [116]. Each of these exchange-correlation

functionals has a characteristic band gap, thus it was possible to discern how significantly each characteristic C_e influenced defect creation.

For each exchange-correlation functional a 2 atom diamond silicon cell was chosen. Projector Augmented Wave (PAW) pseudo potentials were employed with the plane wave expansion truncated at 400 eV. This ensured convergence in each case, as the difference in energy between 400 eV and 600 eV was 0.001%, 0.003%, and 0.004% for the PBE, HSE, and PBE0 functionals respectively. A 16x16x16 Monkhorst-Pack [129] k-point grid for the integration of the Brillouin Zone was chosen. This also ensured convergence, the difference in energy between a 16x16x16 and 22x22x22 grid was 0.002%, 0.0025%, and 0.003% for the PBE, HSE, and PBE0 functionals respectively. A 16x16x16 Fock exchange grid was chosen for the HSE and PBE0 functionals and the mixing fraction of the Fock exchange for HSE was set to 0.25, with a screening parameter of 0.2 $Å^{-1}$. Results for the ground state properties of these functionals are summarised in Table 4.1. These values are in good agreement with other published results using these functionals [130].

Functional	Lattice Parameter (Å)	Band Gap (eV)
PBE	5.469	0.71
HSE	5.435	1.14
PBE0	5.430	1.84
Experiment	5.431	1.10

Table 4.1: Ground state DFT results of silicon compared with experiment [131, 132].

The density of states for the various exchange-correlation functionals is shown in figure 4.1. It is evident that the density of states are extremely similar for all three functionals, with the exception occuring around the band gap region. The band gap of PBE0 is signficantly larger than HSE due to the inclusion of the full range HF exchange contribution. From these DOS plots, the most significant factor which will determine differences in the occupancy between these functionals is the size and curvature band gap. The electronic specific heat, C_e, for each functional was calculated using,

$$C_e(T_e) = \frac{\partial U}{\partial T_e}, \tag{4.2}$$

where U is the internal energy, and T_e is the electronic temperature of the system. An electronic temperature was applied to the system using explicit Fermi-Dirac smearing according to the formalism described in section 2.5.3.2, with an upper limit of 25,000 K (which is approximately 2.15 eV). Self consistent field calculations were then carried out from 0 K to 25,000 K in increments of 250 K, and the electronic specific heat was calculated using equation 4.2.

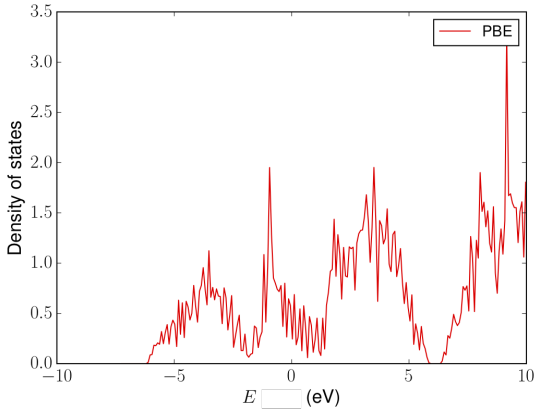

(a) PBE Density of states

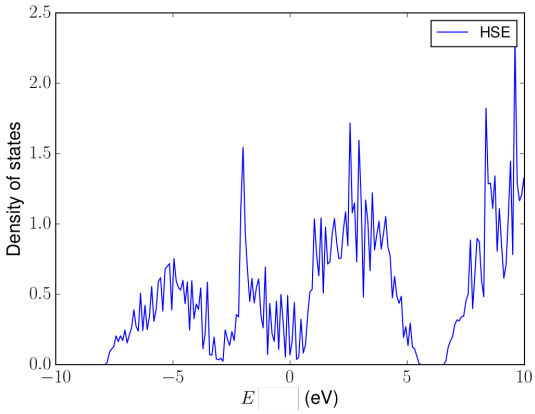

(b) HSE Density of states

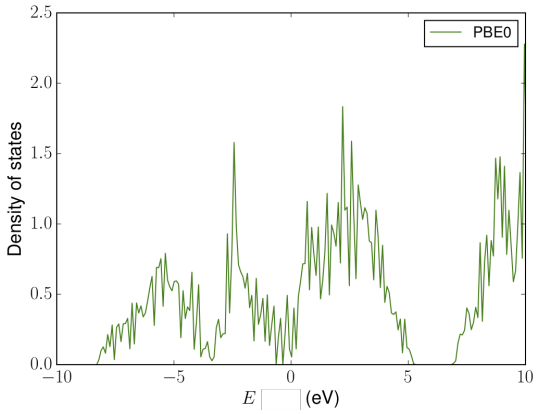

(c) PBE0 Density of states

Figure 4.1: Density of states plots for the various silicon exchange-correlation functionals employed. The density of states was obtained using a fine 21x21x21 k-point grid in each case.

Figure 4.2 shows the temperature dependent electronic specific heat for DFT simulations employing the different exchange-correlation functionals, compared with the free electron gas approximation. This approximation has been by far the most widely used value for the electronic specific heat of band gap materials. It is justified by assuming that hot electrons in a band gap material behave like hot electrons in a metal [50]. For band gap materials this leads to an electronic specific heat $C_e = \frac{3}{2} n_e k_B$, where n_e is the electron number density (taken to be one electron per atom [51], as at least one needs to be excited before contributing kinetically), and k_B is the Boltzmann constant.

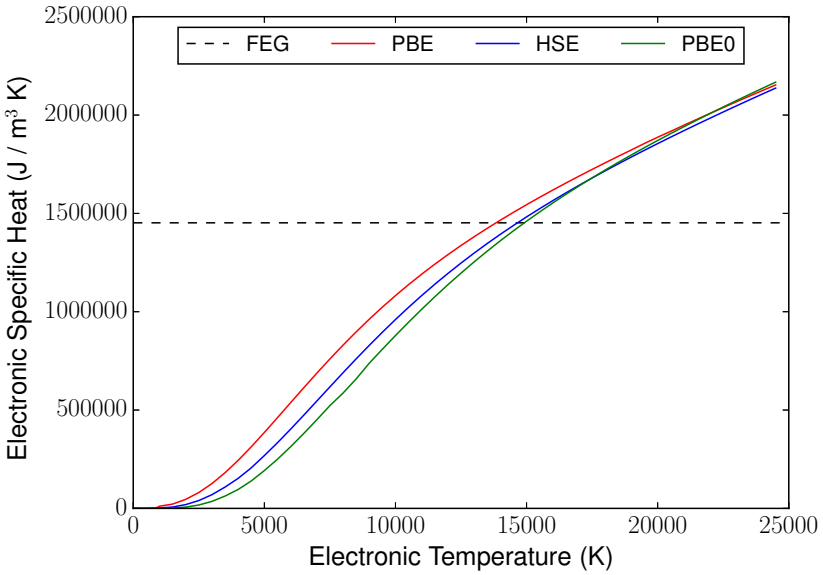

Figure 4.2: Electronic specific heat for Si, calculated using DFT with three different functionals compared to the free electron gas model.

The DFT results show a significant dependence of the specific heat on the choice of exchange correlation functional. As the most significant divergences of the DOS occur around the band gap region, the size of the bandgap is concluded to be the dominant factor determining the specific heat. The larger the band gap, the higher the required electronic temperature for a non-zero heat capacity, as the electrons need to first be excited across the band gap before they can subsequently contribute kinetically. Also, the larger the band gap,

the lower the electronic specific heat. This can be explained by considering the DOS of our system, for a given amount of energy, a larger band gap results in occupancy of higher energy states, and thus a higher electronic temperature is achieved. Interestingly, at high electronic temperatures the electronic specific heats calculated using the three different functionals converge. At these high electronic temperatures the differences in the density of states between all the XC functionals is negligible. These results show band gap contributions can indeed be accounted for within the 2T-MD model. It is also clear that the free electron gas approximation for the electronic specific heat capacity will result in significantly different temperature evolutions, as it is a constant, and completely neglects the presence of a band gap.

The electron-phonon coupling term, G_e, was taken to be a constant in all of these simulations. This is due to the fact no electronic temperature dependent electron-phonon coupling has been achieved for silicon to date. The methods employed by Lin *et al* [44] to extend this temperature dependence in metals cannot be extrapolated to band gap materials, as the equation contains the electron density of states at the Fermi level, which is zero in band gap materials. This constant electron-phonon coupling term, G_e, was calculated using,

$$G = \frac{3Nk_B}{mV\tau_p}, \tag{4.3}$$

where N is the number of atoms in the relevant ionic cell, k_B is the Boltzmann constant, m is the mass of the atomic species, V is the volume of the ionic cell, and τ_p is the electron-phonon relaxation time. τ_p was taken to be 0.26 ps, a value obtained from femtosecond optical pump probe reflectivity experiments [66].

The parameter most difficult to determine within the 2T-MD model for band gap materials is the electronic diffusivity. This is due to the complex dependence that the parameter would have on the highly non-equilibrium local lattice and electronic temperatures. A number of different approximate estimations have been taken in the literature, and here the approach proposed by Dufour *et al* [45] was taken. This is the only temperature dependent diffusivity in the literature that has been successfully applied to band gap materials. This approach assumes that $D_e(T_e) = 300\frac{D_e(300K)}{T_e}$, and saturates at the Fermi temperature. The electronic diffusivity of silicon at room temperature is 33.6 cm^2/s [59]. The spatial variation of the electronic diffusivity and electronic specific heat were ignored.

The parameters of the source term, $A(r,t)$, are based on the properties of a C_{60} cluster with specific energy 0.07 MeV/u. This corresponds to a mean deposition radius calculated using Bohr's principle of adiabatic variance.

$$r_{ion} = \frac{\hbar v_{ion}}{2E_g}, \tag{4.4}$$

where r_{ion} is the mean deposition radius, $\hbar$ is Planck's constant, v_{ion} is the velocity of the imparting ion, and E_g is the band gap of the material it is travelling through. This mean deposition radius was 0.74 nm in silicon. The swift heavy ion was assumed to deposit energy via a spatial Gaussian and temporal exponential distribution with a characteristic deposition time of 1 fs. The source term was normalised so its spatial and temporal integration equates to the energy deposited into the electronic system (the electronic stopping power, S_e).

The diffusivity, $D_e(T_e)$, the electron-phonon coupling, G_e, and the source term, $A(r,t)$, are all identical in the simulations conducted. Any differences in the evolutions of the electronic temperatures are due to the differences in the parameterisation of the electronic specific heat capacities, $C_e(T_e)$. Thus, via (c) in equation 4.1, PBE, which has the highest electronic specific heat capacity for the temperatures investigated, is expected to attain the lowest peak electronic temperature, with PBE0 reaching the highest initial electronic temperature.

Equation 4.1 (b) determines the rate of energy exchange between the electronic and lattice subsystems. As PBE has the lowest specific heat (and all having the same e-p coupling G_e), the rate of energy exchanged between the electrons and lattice will be slowest, followed by HSE, and then PBE0. Despite this information, it is still difficult to predict whether PBE (and by extension a smaller band gap) will be more or less susceptible to damage. If the diffusivity value is high enough PBE could be less prone to damage, as the energy is diffusing throughout the electronic subsystem before it can be transferred to the lattice. If the diffusivity value is low, the slower rate of exchange of energy with the lattice may lead to a wider region of the lattice reaching peak temperatures, causing PBE (and thus the lower band gap) to be more susceptible to damage. As has been mentioned before, it is a complex interdependence on the electronic and lattice parameters. The only way to know is to empirically run the simulations.

4.1.2 Interatomic potential properties

The 2T-MD model also relies critically on an accurate parameterisation of the lattice. In the case of radiation damage simulations, the most important interatomic properties to reproduce would be the melting temperature, the latent heat of melting, and the solid to liquid density change. This ensures that the material is melting in the correct temperature range, and also that the resulting damage distribution is representative of experimental observations. This is particularly important in silicon, as its density increases when it melts. The modified Tersoff (MOD) potential (described in detail in section 2.1.3.3) was chosen as it is by far the best potential at reproducing the above characteristics. It is also a potential that has been parameterised with an explicit electronic temperature dependence (something which will be investigated later in this thesis). Table 5.2 illustrates these thermodynamic properties of the MOD potential and their experimental counterparts.

Property	Unit	MOD	Experiment
Melting temperature	K	1681	1683
Latent heat of melting	kJ mol^{-1}	33.7	50.6
Density change : crystal to amorphous	%	14	10
Amorphous density	g cm^{-3}	2.311	2.05 - 2.52
Crystalline specific heat capacity	J g^{-1} K^{-1}	1.02	1.04
Liquid specific heat capacity	J g^{-1} K^{-1}	1.17	1.04

Table 4.2: Interatomic potential properties of MOD potential [133] compared with experiment [134]

4.2 2T- MD swift heavy ion irradiation of silicon

4.2.1 Simulation setup

The simulations were run using a 200,000 atom supercell measuring 271.99 x 271.99 x 54.4 $Å^3$ dimension (corresponding to an 8 atom cubic unit cell multiplied by 50x50x10). This MD cell was periodic in all directions to simulate a bulk crystal, and was subdivided into a grid of 25x25x5 coarse grained ionic temperature voxels (each $\approx$ 10.86 $Å^3$). A 75x75x5 electronic

temperature voxel grid extends over the MD cell in the xy direction, and this system was solved using a space centred, forward in time Euler method with a timestep of 1 as. Neumann boundary conditions were used to confine the electronic energy in the z-direction. The MD system was pre-equilibrated for 200 ps (with a 1 fs timestep) using an NPT ensemble (300 K) Nosé-Hoover thermo- and barostats. After equilibration the MD cell was connected to the continuum electronic system which was also set to 300 K, and the SHI irradiation was simulated for 20 ps (with a 1 fs timestep), for stopping powers between 5 and 60 keV/nm, repeated five times each for damage statistics.

4.2.2 Temperature evolutions

Figure 4.3 shows the evolution of electronic and lattice temperatures at the centre of a typical SHI simulation for each $C_e(T_e)$. In general the SHI caused the electronic temperature to reach a maximum value in 10 fs. This energy was then transferred to the lattice, which reached its maximum value within 0.1 ps, and both subsystems reached thermal equilibrium after a few ps. The difference between the temperatures predicted using the free electron gas and DFT specific heats was significant throughout. The FEG reached a much higher maximum electronic temperature, cooled at a slow constant rate, and reached a significantly lower equilibrium temperature after a few ps. By contrast, the differences between functionals were less pronounced at the beginning and end of the simulation, but the regions where they diverge had a significant impact on the dynamics of the system. PBE0 reached the highest peak electronic temperature at the beginning of the simulation, however, it was too small of a difference (a few thousand Kelvin) to be noticeable on figure 4.3 (a) due to the temperatures being in the hundreds of thousands of Kelvin.

The most striking differences in the temperature profiles for the different functionals occured when the electronic temperature cools to between 20,000 K and 3,000 K. As PBE had the highest $C_e(T_e)$ in this range, the rate of transfer to the lattice ((b) in equation 4.1) was lower, thus it stayed at a significantly higher electronic temperature throughout this period. The sharp change in shape of electronic temperature at roughly 0.1 ps is due to the saturation of the electronic diffusivity, which has an lower bound of $2\,\mathrm{cm}^2/\mathrm{s}$ at the Fermi temperature.

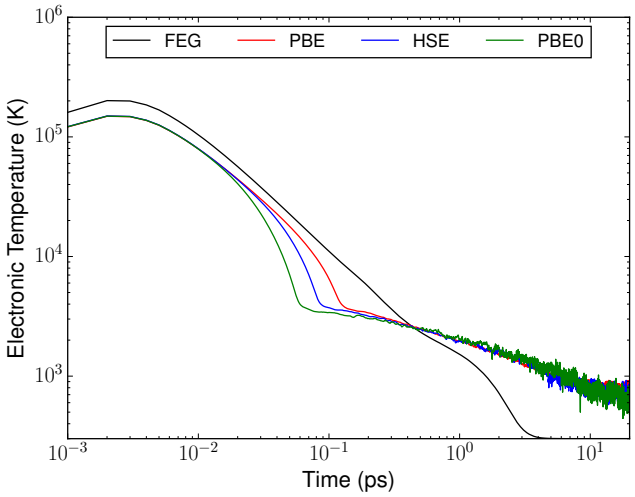

(a) Electronic temperature evolution at centre of cell

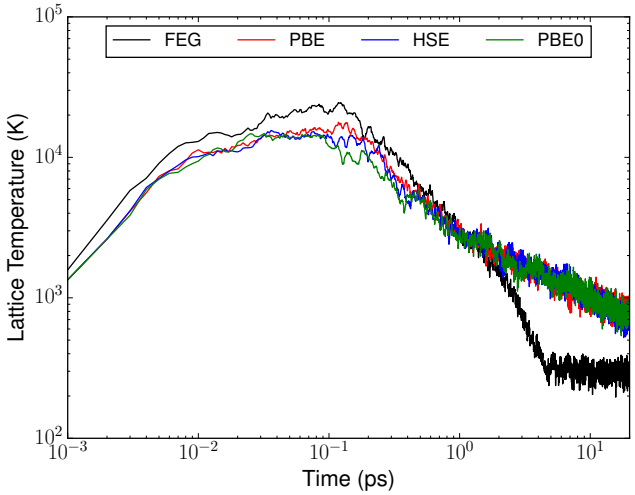

(b) Lattice temperature evolution at centre of cell

Figure 4.3: Temperature evolutions at the centre of the simulation cell using electronic specific heats calculated with different functionals, during a 25 keV/nm SHI event.

Despite PBE having this lower electron-phonon coupling strength, there was no clearly significant observable difference between the lattice temperatures at the centre of the cell when using the specific heat derived via *ab initio* methods. Therefore any significant differences

in track radii were more readily understood by looking at the cross-sectional electronic and lattice temperatures for each $C_e(T_e)$ at various times during these simulations. Figure 4.4 shows these electronic temperature cross-sections.

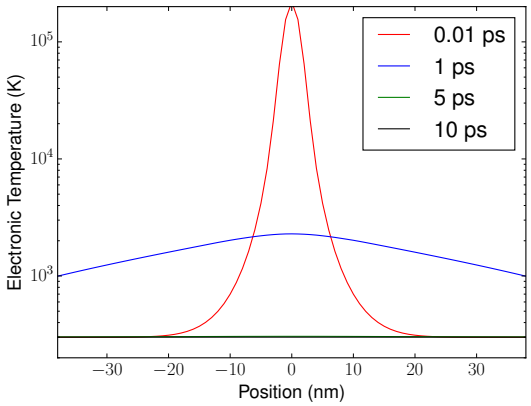

(a) Electronic temperatures using the FEG $C_e(T_e)$.

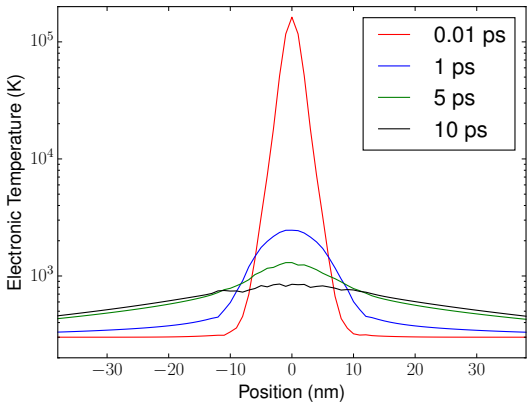

(b) Electronic temperatures using the PBE $C_e(T_e)$.

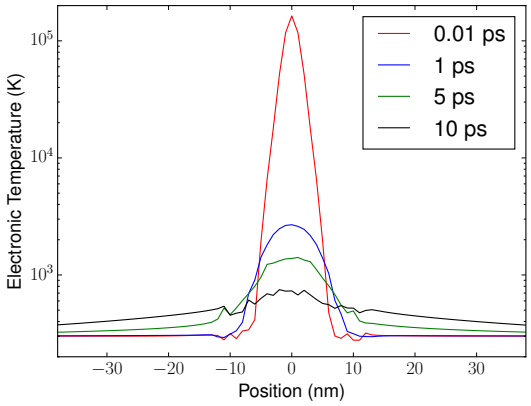

(c) Electronic temperatures using the HSE $C_e(T_e)$.

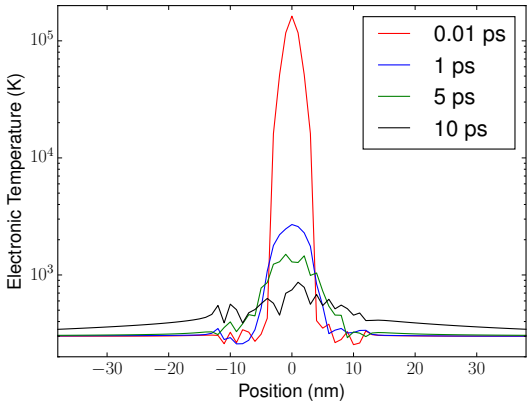

(d) Electronic temperatures using the PBE0 $C_e(T_e)$.

Figure 4.4: Cross-sectional electronic temperatures with various electronic specific heat during a 25 keV/nm SHI event.

Once again the FEG approximation showed the most disparate behaviour when compared to the DFT functionals. It reached the highest electronic temperature at the beginning of the simulation (consistent with figure 4.3 (a)) However, due to the constant electron-phonon coupling strength, energy diffused very quickly (spatially and temporally), resulting in the electronic system being at thermal equilibrium at 5 ps. It was clear from figure 4.4 that the electronic temperatures between the various functionals at each time shown were not significantly different. The key difference was due to the electron-phonon coupling strength confining energy in the electronic system for the functionals with a higher specific heat for longer. So PBE had a wider area of its cell at a higher electronic temperature than HSE (and correspondingly HSE had a wider area of its cell at a high temperature compared to PBE0).

Figure 4.5 shows the corresponding cross-sectional lattice temperatures. A similar pattern emerges, as the peak lattice temperatures that occured at each time-step were the same for the various $C_e(T_e)$ (consistent with figure 4.3 (b)), but the area over which each exceeded the melting temperature was significantly different. For a large electronic specific heat, the electron-phonon coupling strength was reduced, meaning energy diffused more widely in the electronic system before being deposited into the lattice. Thus when energy was exchanged to the lattice a wider area ended up reaching these high temperatures, leading to a larger ion track. From these data it was expected that the larger the band gap of a material, the more resistant that material was to damage (assuming the other parameters in the model remained constant). Conversely, a larger band gap led to a lower $C_e(T_e)$, thus the rate of transfer of energy to the lattice was higher, and thus the spatial region where the lattice temperature exceeded the melting threshold was more localised, leading to smaller track radii.

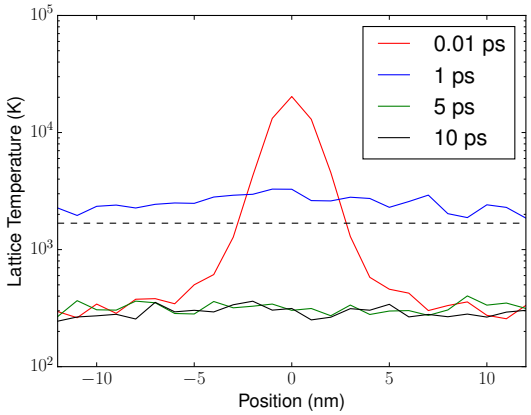

(a) Lattice temperatures using the FEG $C_e(T_e)$.

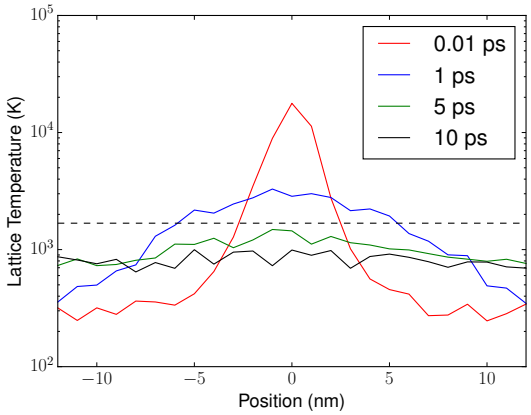

(b) Lattice temperatures using the PBE $C_e(T_e)$.

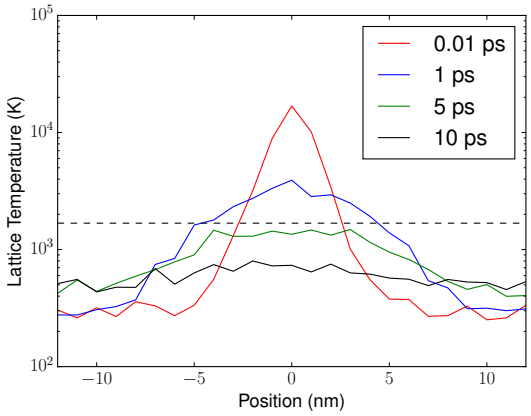

(c) Lattice temperatures using the HSE $C_e(T_e)$.

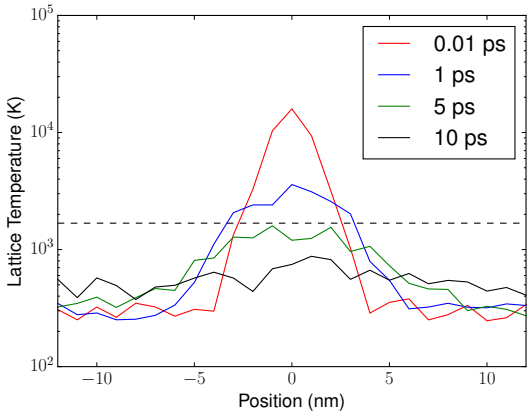

(d) Lattice temperatures using the PBE0 $C_e(T_e)$.

Figure 4.5: Cross sectional lattice temperatures with various electronic specific heat during a 25 keV/nm SHI event. The dashed line represents the melting temperature of the interatomic potential. The dashed line in each plot corresponds to the melting temperature of the interatomic potential.

4.2.3 Defect evolutions

In a typical simulation a defect population was established within 0.1 ps. The number of defects increased as energy diffused through the cell, reaching a maximum value at 1 ps.

The lattice then cooled, recrystallised, and a final defect distribution was established within 5 ps. Figure 4.6 (a) - (d) shows the evolution of local structure following SHI irradiation. Initially all atoms exhibited a perfect diamond structure (light blue), however, 0.1 ps after initialisation of the SHI there was a localised amorphous region at the centre of the simulation cell. The darker blue represents a denser region of cubic diamond which was due to the rapid expansion of the cylinder of atoms at the core. The black region is a small halo where diamond structure only extended out to the 1st and 2nd nearest neighbours. After 1 ps these compressed regions relaxed, and by 5 ps the final defect distribution was observed. The Wigner-Seitz defect evolution at the corresponding times are shown in figure 4.6 (e) - (h). The Wigner-Seitz defects were calculated using Voronoi cell analysis [120]. If an atom moved from its original Voronoi cell a vacancy was formed, and if an atom moved into an occupied Voronoi cell an interstitial defect was formed.

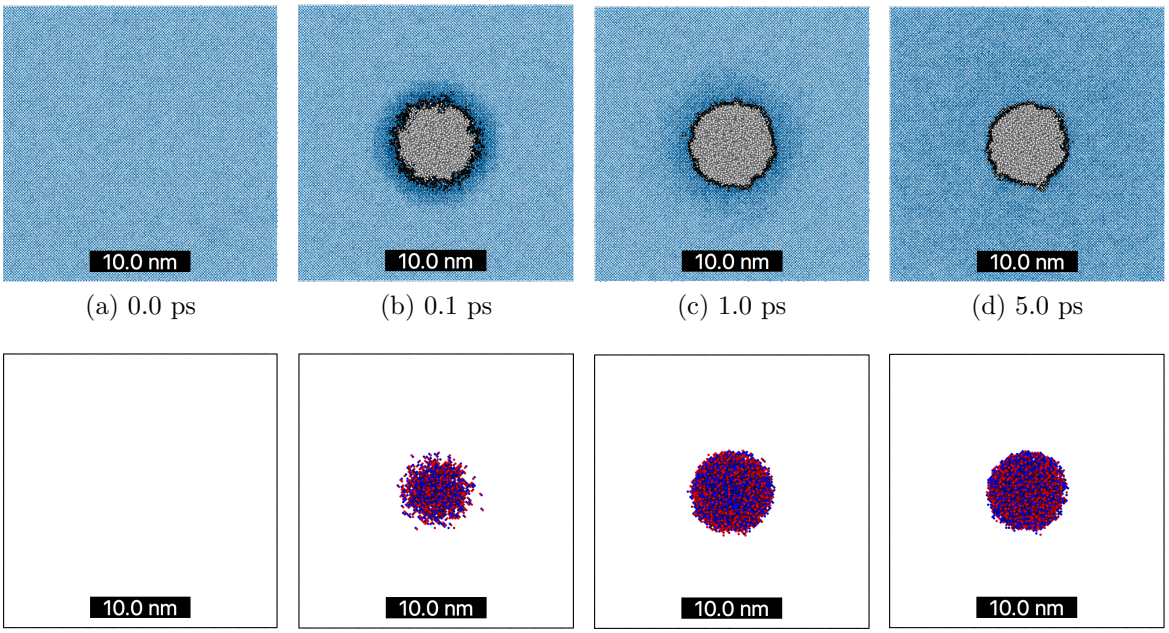

(a) 0.0 ps (b) 0.1 ps (c) 1.0 ps (d) 5.0 ps

(e) 0.0 ps (f) 0.1 ps (g) 1.0 ps (h) 5.0 ps

Figure 4.6: [001] ion track morphology at various times during a 25 keV/nm SHI simulation using the HSE functional. (a) - (d) are coloured according to local structure : light blue represents diamond structure, the darker blue is a region of compressed cubic diamond, black is 1st and 2nd neighbour diamond, and grey amorphous structure, determined via common neighbour analysis. (e) - (h) are Wigner-Seitz defects, blue representing vacancies and red representing interstitials. Both sets of images were created using OVITO [119].

Figure 4.7 shows the typical evolution of Wigner-Seitz defects for a low, middle, and high value of electronic stopping power. Each case displays the same qualitative behaviour, the number of defects reached a maximum within 1 ps, after which about 10 % of the defects recombined, and the final defect distribution was formed within 5 ps. This highlights a significant difference in the behaviour of defect formation between metals and silicon. In a metal, the most of the defects that are initially formed by the SHI end up recombining, whereas a very small fraction recombine in silicon. Thus one could arguably say that ion tracks only form in band gap materials, as the defect distributions formed in metals can not be easily described as a cylindrical amorphous region adjacent to the swift heavy ions path.

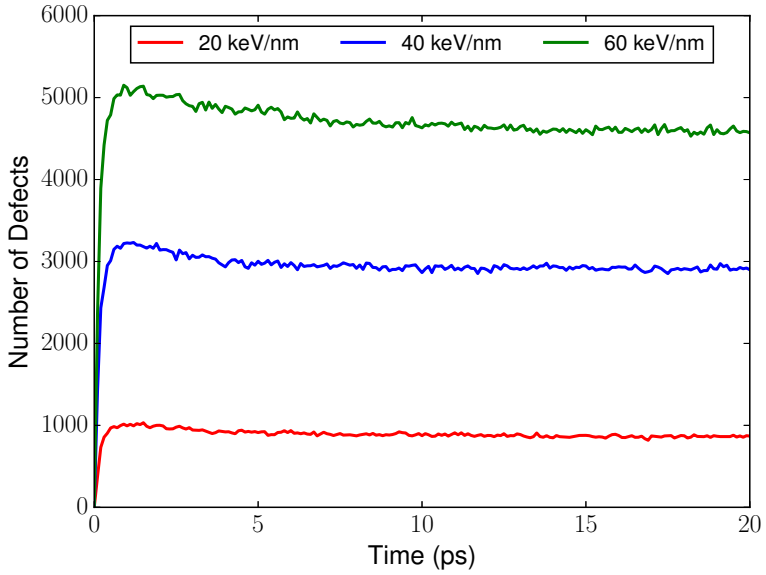

Figure 4.7: Evolution of Wigner-Seitz defects with time for various stopping powers using the electronic specific heat derived with the HSE functional

A number of simulations were performed to determine the relationship between the size of the ion track and the energy deposited by the SHI (quantified by the electronic stopping power, S_e) for each $C_e(T_e)$. The track distributions were analysed in two different ways, via track radius, and number of Wigner-Seitz defects. The track radius was determined by calculating the atomic density of each particle as a function of distance from the centre of cell using Voronoi cell analysis. Two distinct track radii profiles were observed, depending on the amount of energy deposited. At relatively low stopping powers the track consisted of an overly dense amorphous region, corresponding to the blue line, which is an ion track of $\approx 18\,\text{Å}$. This is consistent with a mechanism whereby an overdense liquid core is created and subsequently quenched to form overdense amorphous Si. By contrast, at higher stopping powers the energy deposition was large enough to eject atoms from the centre of the core. This resulted in an underdense core, surrounded by an overdense amorphous outer track region (shown by the red line in figure 4.8, which is an ion track of $\approx 50\,\text{Å}$). These different track signatures may be observable in future small angle X-ray scattering (SAXS) experiments on crystalline silicon. Previous SAXS experiments, and the corresponding MD

simulations, that have characterised the damage resulting from SHI irradiation of amorphous Si [13] show an overdense core similar to our low stopping power result in figure 4.8.

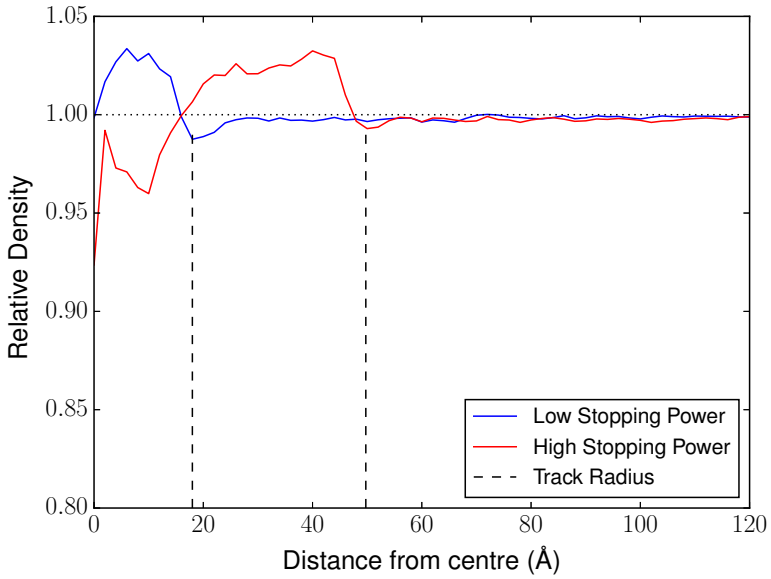

Figure 4.8: Relative atomic density as a function of distance from the centre of the simulation cell. The black dotted line corresponds to the ion track radius. Blue and red lines show the results from a 10 keV/nm and 25 keV/nm SHI simulations, using the PBE0 and PBE electronic specific heats respectively. The dotted vertical line marks the track radius of 18 Å for the low stopping power and 50 Å for the high stopping power.

Figure 4.9 shows how the electronic specific heat leads to significantly different final defect distributions and track radii. At 5 keV/nm an ion track with a radius of 16.9 Å was predicted using the specific heat determined by the free electron gas model. By contrast, no continuous ion tracks were formed when the specific heats from DFT were used, but there were some isolated vacancy and interstitial defects. Simulations using the free electron gas approximation were only carried out to an S_e of 25 keV/nm as higher stopping powers resulted in defect distributions that approached the boundary of our MD cell. For all stopping powers tested the number of defects and the resulting track radii calculated using $C_e(T_e)$ from the free electron gas model are substantially greater than when using $C_e(T_e)$ determined via DFT.

Figure 4.9b suggests that when DFT is used to parameterise the specific heat, the change in the track radius as a function of stopping power is consistent with the profiles observed in experimental studies of other semiconductors [8, 135, 13] and insulators [136, 5, 58]. Traditionally, this effect was explained by the velocity effect [70], where ions with a greater velocity deposit more localised energy into the electronic subsystem. These simulations neglect the velocity effect completely, but show a similar relationship. Thus both the electronic specific heat, and the profile of the deposited energy contribute to the experimentally observed correlation. The free electron model, on the other hand, showed a linear relationship between track radius and electronic stopping power. This is because the rate of energy transfer from the electrons to the lattice was constant regardless of electronic temperature, thus the spatial region of atoms which had a temperature higher than the melting threshold increased proportionally to the electronic stopping power.

A clear relationship was observed between the sensitivity of ion track radii with different electronic specific heats, each with a characteristic density of states (and hence band gap). The larger the band gap, the more resistant the material was to damage (assuming all the other parameters in the model remained the same). An apparent relationship between the threshold stopping powers and the band gap of a semiconductor has been noted previously from experimental observations [59]. This was attributed to an inverse relationship between the electron mean free path and the band gap, although no physical justification was offered. These results suggest it was the electronic specific heat, as opposed to the mean free path, that was related to the band gap, and the modified relaxation time for the electron ion energy transfer affected the track radii.

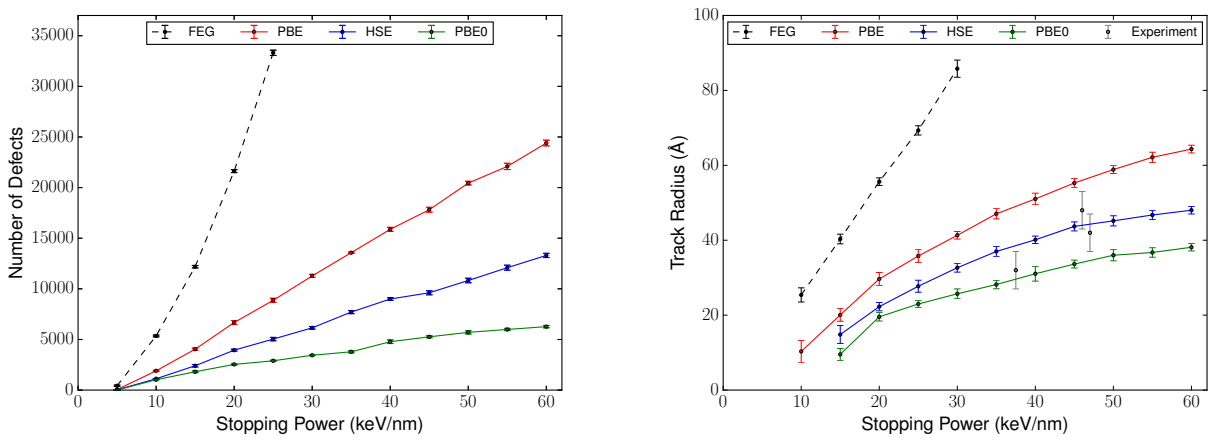

(a) (b)

Figure 4.9: Defects vs electron stopping power. (a) is the total number of Wigner-Seitz defects as a function of stopping power. (b) is the track radius as a function of stopping power. Each data point is the mean value of five repeated simulations, and the error bars correspond to the standard error.

The HSE functional predicted a bandgap in excellent agreement with the experimental value of 1.11eV [132]. The track results with this functional also agreed well with experimental tracks observed via the irradiation of silicon using C_{60} fullerenes [137, 138]. The threshold for track creation was lower than experimental observations [9, 139], but this may be explained by the fact that fast monatomic ions deposit energy more widely amongst the targets electrons (the so called velocity effect, which is analagous to increasing the mean absorption radius of the source term in equation 1.17), leading to less damage. It is also worth noting that the inclusion of changes in the interatomic interactions due to electronic excitation [39, 111, 38], which may influence the results were also not investigated. The effects of these modified interactions will be investigated, using electronic temperature dependent potentials, in the final chapter of this thesis.

4.3 Conclusion and summary

Ion track formation resulting from swift heavy ion irradiation in silicon was modelled, using the two-temperature molecular dynamics model, for a range of stopping powers. The defect distribution formed in all these silicon simulations show distinct behaviour to the defects presented in the preceding chapter on metals. The vast majority of initial defects formed in metals ended up recombining, whereas in silicon only 10% of the initially formed damage recrystallises. Thus ion tracks, classified as cylindrical defect rich regions formed around the path of a SHI, formed in silicon, but not in any of the metals investigated.

A clear difference in track morphology for low stopping powers was observed, where the track had an overdense core, and high stopping powers, where the tracks had a core shell structure with an underdense core and an overdense shell. This may be an important signature to look out for in future SAXS experiments. The temperature dependence of the electronic specific heat was calculated, an important parameter of the 2T-MD model, using DFT with different functionals. The most significant divergence in the density of states of each of these functionals was due to the characteristic band gap. This in turn lead to distinct temperature dependent specific heats. The lower specific heat associated with larger band gaps resulted in a shorter relaxation time for the electron lattice energy transfer and corresponding smaller track radii. The higher specific heat associated with the smaller band gap functions resulted in energy spreading more widely in the electronic system. This in turn caused a larger area of the lattice to exceed the melting temperature, resulting in larger track radii. This provides an explanation for the observed dependence of threshold stopping power on the band gap, which had previously been attributed to the mean free path. Simulations using the specific heat with the most accurate band gap give track radii closest to the those observed in experiment.

While these results highlight a significant advance for the 2T-MD model in band gap materials, it is worth discussing a number of limitations that still exist in the model. Firstly, the parameterisation of the electronic subsystem is nowhere near as comprehensive as what is possible for metals. An electronic temperature dependent electron-phonon coupling will have a huge influence on the final defect distributions formed. Also, a more accurate electronic diffusivity and energy deposition profile [73] are paramount to the model's success. However, despite these short comings in the model, the results presented in the chapter do highlight

that bandgap effects can be introduced into the two temperature model by an accurate representation of the temperature dependence of the electronic specific heat. These results also highlight an important consideration for all future and past work in applying the 2T-MD model to band gap materials; not only is it important to utilise a $C_e(T_e)$ derived via *ab initio* methods, it is also important to highlight how far from experimental values the DFT functional deviates from experimental band gap values. It is easy to underestimate the band gaps of semi-conductors and insulators by 20 - 30 % or more using the most common exchange-correlation functionals, and these differences will significantly skew track radii when comparing to real experimental results.

5

Swift heavy ion irradiation of silicon (ii)

"Nothing happens until
something moves."

Albert Einstein

This chapter investigates ion track creation in silicon using the extended two-temperature molecular dynamics model, the atomistic version of the extended inelastic thermal spike (eiTS) model. Similarly to the regular 2T-MD model, the atoms evolve according to an augmented version of molecular dynamics. However, the difference arises in modelling the carriers (as now electrons and holes are considered). These carriers evolve according to Boltzmann transport equations. The model has significantly more parameters than the traditional formulation of the two-temperature model. Thus silicon was chosen as it is the most studied band gap material, with good equilibrium data for most parameters in the model. While the original model tracked the evolution of electronic temperature, this model tracks the evolution of carriers (and their associated energy), with temperature being calculated afterwards. This marks a significant departure from the original formalism, thus this chapter aims to achieve detailed comparison between 2T-MD and extended 2T-MD for ion track creation in silicon. The most important conclusion from this analysis is whether the added complexity of the extended model (while sacrificing temperature dependent parameterisations) leads to physics that cannot be explained by the regular model. As the majority of materials that are sensitive to ion track creation are band gap materials, any advance in the accuracy of methods to model these interactions will be beneficial to the wider community.

5.1 Extended 2T-MD model parameters for silicon

5.1.1 Carrier System

The carrier system in the extended implementation of the 2T-MD model is significantly more complex than the conventional model. The parameters include the recombination terms (Auger and impact ionisation coefficients), electron and hole thermal conductivities, electron and hole mobilities, the electron-phonon coupling, ambipolar diffusivity, the source term, and electron-hole specific heat capacity. Like the conventional two-temperature model, a number of these parameters will have complicated lattice and carrier temperature dependencies.

The model was assumed to be charge neutral, by constraining the electrons and holes to exist as bound pairs. Thus the individual carrier thermal mobilities, and thermal conductivities, were simplified to effective bound electron-hole contributions, respectively. Based on the Wiedemann-Franz law, the thermal conductivity of this bound electron-hole pair has the form,

$$\kappa_{e-h}(T_e) = \left(\frac{5}{2} - p\right)\left(\frac{k_B}{q}\right)^2 q\,\mu_{e-h}\,N\,T_e \tag{5.1}$$

T_e is the carrier temperature (assumed to be the same for both electrons and holes), q is the charge, p is a correction factor to account for the non-parabolic relationship between the carrier energy and carrier momentum, μ_{e-h} is the electron-hole mobility, and N is the carrier density. It is worth noting this formulation was based on method developed for metals, however no better formulation currently exists for band gap materials. The reduced electron-hole mobility is,

$$\mu_{e-h} = \frac{1}{2}(\mu_e + \mu_h) \tag{5.2}$$

Here μ_e and μ_h are the individual electron and hole mobilities for silicon. These values are well characterised at room temperature and lower [140, 86], however no data exists for large temperatures (especially not for different lattice and carrier temperatures). The temperature

dependence proposed by Baccarani *et al* [89], which equates the thermal conductivity in equation 5.1 to the thermal conductivity term in the Einstein–Smoluchowski relation, was used,

$$\mu_{e-h}(T_e) = \mu_0 \frac{T_i}{T_e}, \tag{5.3}$$

where μ_0 is the bound electron-hole carrier mobility at room temperature, and T_i is the lattice temperature. The ambipolar diffusivity (the diffusivity of a bound electron-hole pair), is also known at room temperature [141] ($19\,\mathrm{cm}^2/\mathrm{s}$), and has been observed to decrease with increasing carrier concentration and lattice temperatures [141, 142]. The same temperature dependence as the conventional 2T-MD model was assumed [45] : $D(T_e) = 300K\frac{D(300K)}{T_e}$, where D is the ambipolar diffusivity, saturating at the Fermi temperature.

The electron-phonon coupling term used in the model was also the same as the regular 2T-MD model, a constant value of 0.26 ps, based on femtosecond optical pump probe reflectivity experiments [66]. The impact ionisation and Auger recombination coefficients have been well characterised for silicon [143, 144]. Due to the nature of the extended model's implementation, a prior knowledge of the electron-hole specific heat capacity, C_{e-h}, is not required. It can be derived from the fundamental equation governing how energy is distributed amongst the carriers,

$$U = NE_g + 3Nk_BT_e, \tag{5.4}$$

Here U is the total energy, and E_g is the band gap. The electron-hole specific heat is thus,

$$C_{e-h} = \frac{\partial U}{\partial T_e} = N\frac{\partial E_g}{\partial T_e} + 3Nk_B \tag{5.5}$$

Spatial variations in the band gap were neglected, as this quantity is highly dependent on the local atomic configuration, and thus the complexity involved is beyond the scope of this thesis. Electronic temperature variations were also neglected, thus $C_{e-h} \approx 3Nk_B$. Thus a linear relationship between carrier density and the electron-hole specific heat was assumed, similar to the linear approximation used in the 2T-MD model by Dufour *et al* [45]. The pa-

rameters of the source term, $A(r,t)$, were also the same as described in the previous chapter. Table 5.1 contains a summary of the relevant parameters for the carrier subsystem in the extended 2T-MD model, including their respective temperature dependencies if relevant.

Quantity	Unit	Symbol	Value
Auger coefficient [144]	cm^6/s	δ	$3.8x10^{-31}$
Impact ionisation coefficient [143]	s^{-1}	γ	$3.6x10^{10}\ \exp(\frac{-1.5E_g}{k_B T_e})$
Electron mobility [140]	$cm^2/\ Vs$	μ_e	1400
Hole mobility [140]	cm^2/Vs	μ_h	450
Ambipolar diffusivity [141]	cm^6/s	D	$19\ (300/T_e)$
Electron-phonon relaxation time [66]	ps	τ_{ep}	0.26

Table 5.1: Parameters characterising the carrier subsystem for silicon in the extended two-temperature molecular dynamics model.

5.1.2 Interatomic potential properties

The interatomic potential used for the augmented molecular dynamics portion of the extended 2T-MD was also the same as described in the preceding chapter. Table 5.2 illustrates the most important properties of this MOD potential, and compares them to the relevant experimental values.

Property	Unit	MOD	Experiment
Melting temperature	K	1681	1683
Latent heat of melting	kJ mol^{-1}	33.7	50.6
Density change : crystal to amorphous	%	14	10
Amorphous density	g cm^{-3}	2.311	2.05 - 2.52
Crystalline specific heat capacity	J g^{-1} K^{-1}	1.02	1.04
Liquid specific heat capacity	J g^{-1} K^{-1}	1.17	1.04

Table 5.2: Interatomic potential properties of MOD potential [133] compared with experiment [134]

5.2 Extended 2T- MD swift heavy ion irradiation of silicon

5.2.1 Simulation setup

The simulations were run using a 200,000 atom supercell measuring 272 x 272 x 54 $Å^3$ dimension (corresponding to an 8 atom cubic unit cell repeated 50x50x10 times). This MD cell was periodic in all directions to simulate a bulk crystal, and was subdivided into a grid of 25x25x5 coarse grained ionic temperature voxels (each $\approx$ 10.86 $Å^3$). A 50x50x5 electronic temperature voxel grid extends over the MD cell in the xy direction, and this system was solved using a space centred, forward in time Euler method with a timestep of 1 as. The reduction in the size of the electronic temperature cells compared to the regular 2T-MD implementation was due to the added complexity in the solver for the carrier subsystem. Neumann boundary conditions were used to confine the electronic energy in the z-direction. The MD system was pre-equilibrated for 200 ps (with a 1 fs timestep) using an NPT ensemble (300 K) Nosé-Hoover thermo- and barostats. After equilibration the MD cell was connected to the continuum electronic system which was also set to 300 K, and the SHI irradiation was simulated for 40 ps (with a 1 fs timestep). Due to the complexity of the solver, the MD cell and the carrier continuum system were disconnected after a period of time which ensured most of the energy was transferred from the carriers to the lattice. After 3.5 ps, 99.99% of energy had been transferred in the case of a high energy swift heavy ion. Thus 4.0 ps was chosen as the decoupling time. After this decoupling, energy had no means of leaving the lattice (as this traditionally happened in the electrons). Thus a number of different Langevin thermostats were added to the boundaries (with a thermostat relaxation time of 1 ps, 2 ps, and 3 ps investigated). There were no significant differences in the defect evolutions between either of these three thermostats, and all results presented in this thesis utilised this 2 ps pseudo-Langevin thermostat at the lattice boundaries.

5.2.2 Carrier and temperature evolutions

The key difference between the extended and regular implementation of the 2T-MD model is that the extended model tracks carrier dynamics, and the regular model tracks the evolution

of electronic temperature. Thus the evolution of carriers in silicon following swift heavy ion irradiation is as follows : a proportion of the SHI's energy excites electrons across the band gap, with the remaining energy going into the kinetic energy of the excited electron-hole pairs. These excited carriers combine via Auger recombination, and can be further generated via impact ionisation. The temperature gradient in the carrier system causes the carriers to diffuse into regions of lower temperature, and energy from the carriers is transferred to lattice in a manner that is proportional to both the temperature difference between the two subsystems, and the number of excited carriers in that local region.

Thus the first important aspect of the model investigated was how the carrier conservation terms (the Auger and impact ionisation coefficients) influenced defect creation in silicon. This is important as these key physical processes can not be accounted for within the regular implementation of the two-temperature model. Impact ionisation did not have any significant influence on the carrier evolution, as is shown in Figure 5.1(a). Thus throughout the rest of the simulations this effect was neglected, in order to simplify the differential solver.

Figure 5.1 (b) illustrates how the inclusion of Auger recombination affects the evolution of carrier concentration and temperature following swift heavy ion irradiation. Figure 5.1 shows the evolution of carrier concentration in a typical extended 2T-MD simulation. All regions other than the centre of the cell had an initial increase in carrier concentration immediately following SHI irradiation, implying carriers diffused from the excited centre of the cell into the bulk at the edges of the carrier system. Although less significant than diffusion, Auger recombination also contributes to a decrease in carrier concentration. For both cases, the carrier concentration tends to decrease to equilibrium values between 2 ps and 3 ps (a longer value was observed without Auger recombination, as more carriers needed to diffuse). Figure 5.2 (a) illustrates the respective evolution of carrier temperature in the model. Here the impact of Auger recombination was clearly evident, as when an electron and hole recombine, energy is transferred to an already excited electron, increasing the overall kinetic energy in the carrier subsystem (demonstated by larger carrier temperatures). This difference in temperature is most pronounced between 20 fs and 100 fs, however it remained significantly different throughout the time that the carrier system is connected to the lattice. Both scenarios reach room temperature in under 2 ps. This difference in carrier temperature did not translate into a significant effect on the evolution of corresponding lattice temperatures, as

shown in figure 5.2 (b). For all simulations tested, the lattice temperatures with and without Auger recombination were roughly the same, and in turn ion track radii had no discernible differences.

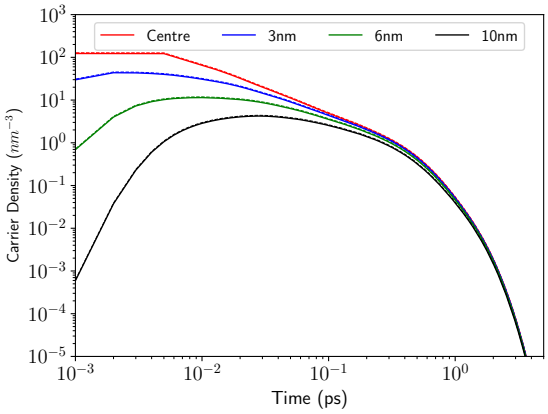

(a) Carrier concentrations without (solid) and with (dashed) impact ionisation 35 keV/nm swift heavy ion.

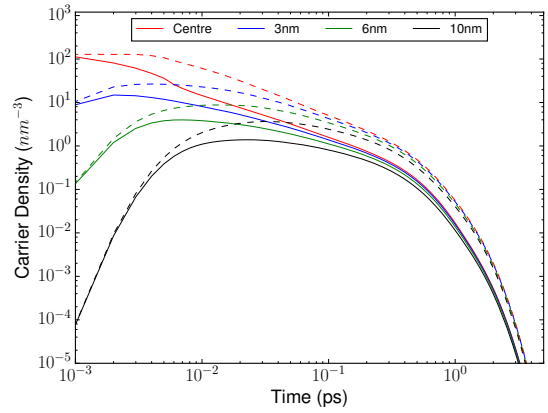

(b) Carrier concentrations with (solid) and without (dashed) Auger recombination following a 30 keV/nm swift heavy ion.

Figure 5.1: The influence of impact ionisation and Auger recombination on carrier concentration in Si using the extended 2T-MD model. The influence of impact ionisation is so insignificant that it is difficult to discern between the solid and dashed lines. The corresponding influence of Auger recombination on the carrier concentrations is far more pronounced.

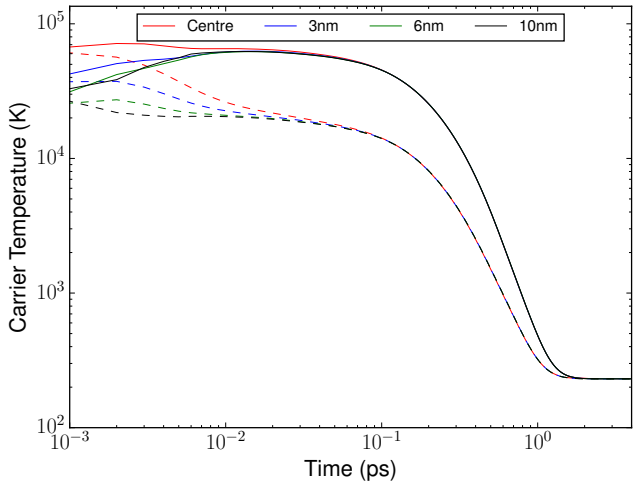

(a) Electronic temperatures with and without Auger recombination

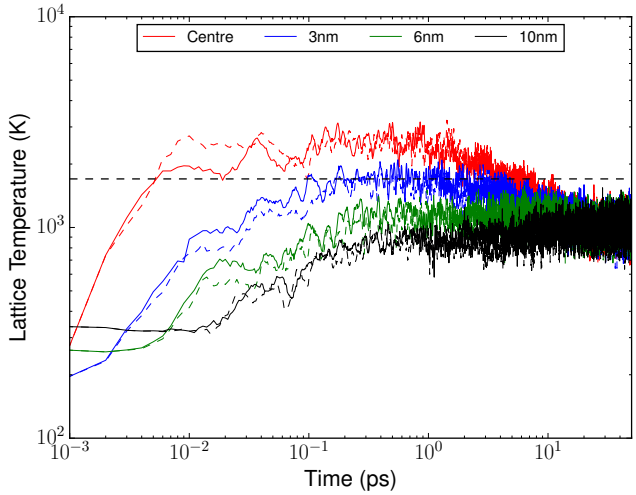

(b) Lattice temperatures with (solid) and without (dashed) Auger recombination

Figure 5.2: The influence of Auger recombination on carrier and lattice temperature in Si using the extended 2T-MD model, following irradiation by a 30 keV/nm swift heavy ion. The dashed lines in (b) correspond to simulations neglecting Auger recombination, and the solid lines correspond to its inclusion. The horizontal line corresponds to the melting temperature of Si using the MOD interatomic potential. No ion tracks were formed by this SHI.

This is due to the fact that the electron-phonon coupling in the extended model is not only proportional to the temperature difference between both the subsystems, but also the local carrier concentration, so this excess carrier temperature is negated by the lower number of carriers due to recombination. It is worth stressing that this does not mean Auger recombination will not have a significant impact on ion track formation within the context of this extended 2T-MD implementation. In fact, it is quite likely that when incorporating an electronic temperature dependent electron-phonon coupling (which should increase in strength with increasing electronic temperature), these increased carrier temperatures due to Auger recombination will lead to greater lattice temperatures, and subsequently larger ion tracks. Figure 5.2 (b) also demonstrates the benefit in utilising a hybrid continuum-atomistic approach, namely that despite the central of the MD exceeding the interatomic potential's melting point, no ion tracks were observed. This physics is impossible to simulate with a continuum model alone.

Now that the characteristics of the model are established, the next important area to address is whether the vastly more complicated solver leads to significantly different thermodynamic evolutions when compared with the regular 2T-MD implementation. All regular 2T-MD model results presented utilised an electronic specific heat derived using the HSE hybrid functional (as this band gap is closest to the experimental value in silicon), and the same choices for the other parameters as described in the previous chapter. Figure 5.3 illustrates the temperature evolutions in both the extended and regular 2T-MD model at the centre of the MD cell following irradiation by a 30 keV/nm swift heavy ion. The regular model achieved much higher electronic and therefore lattice temperatures, with both subsystems coming into thermal equilibrium within 1 ps, and cooling towards room temperature much more rapidly. The corresponding carrier temperature at the centre of cell was nearly an order of magnitude lower than the regular model initially, but carrier diffusion and electron-phonon coupling drove the carriers to room temperature much more rapidly (within 1 ps). The lattice also cooled more gradually. After 50 ps the lattice was still about 900 K. These thermodynamic evolutions resulted in the observation of significantly different defect distributions, the extended model was defect free, and the regular model had an ion track radius of 37 Å.

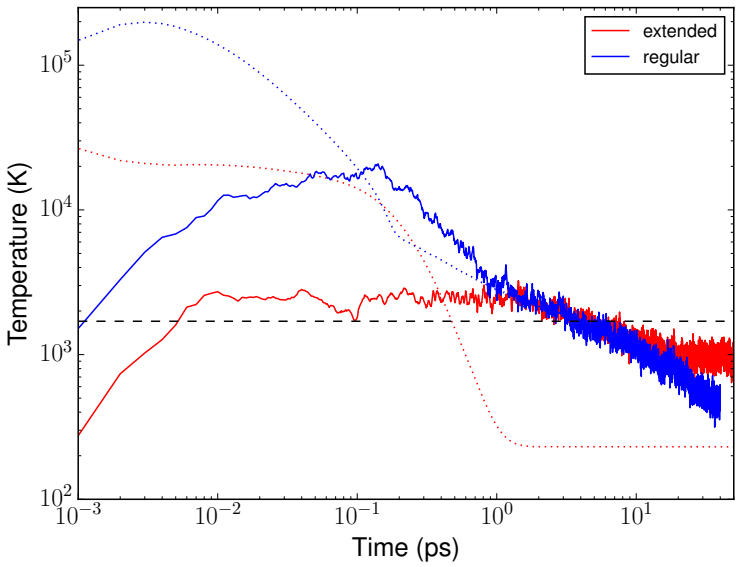

Figure 5.3: Comparison of temperature evolutions in the extended and regular 2T-MD model when irradiatied by a 30 keV/nm SHI. The dotted line represents the electronic (or carrier) subsystem, and the solid line represents the respective lattice subsystems. The horizontal black dashed line is the melting temperature for Si using the MOD interatomic potential.

Figure 5.4 illustrates the key difference between the extended and regular two-temperature model, namely that electronic temperature is the key quantity in the regular model, while carrier density is key in the extended model. Figure 5.4 (b) shows the carrier temperature at various distances from the centre of the MD cell. The carriers all converge to the same excited temperature rapidly (within tens of fs), regardless of the location in the cell. This high temperature only applies to the carriers that have been excited, and figure 5.4 (a) shows that the further away from the centre of the cell, a smaller concentration of carriers were excited, so despite these carriers having extremely high temperatures, there were not enough present to significantly transfer energy to the lattice. As the electronic temperature is the key parameter in the regular 2T-MD model, the T_e evolutions in figure 5.4 (b) (described by the dashed lines) evolved similarly to carrier concentration in the extended model : they decreased as the distance from the centre of the cell increased.

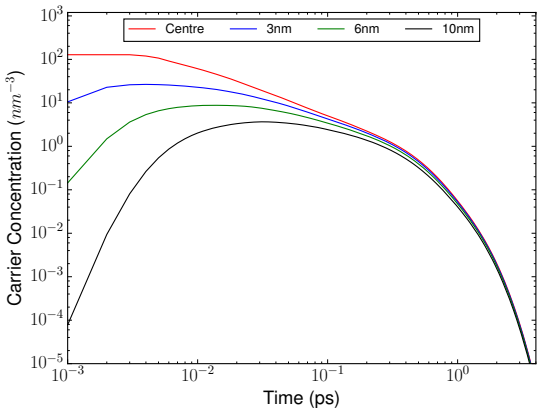

(a) Evolution of carrier concentration in extended 2T-MD model at various distances from the centre of the cell.

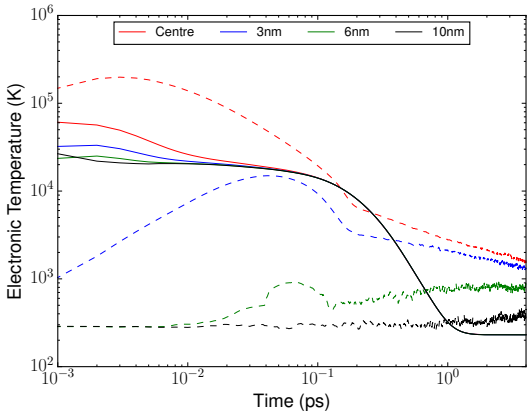

(b) Comparison of carrier temperatures in regular and extended 2T-MD models at various distances from the centre of the cell.

Figure 5.4: Comparison of carrier dynamics in regular and extended 2T-MD models, at various distances, following irradiation by a 30 keV/nm swift heavy ion. The dashed lines correspond to simulations using the regular model, and solid lines correspond to the extended model.

The complementary lattice temperature evolutions are shown in figure 5.5. As described previously, the lattice temperature towards the centre of the cell was much higher in the regular model (an order of magnitude greater), which was the most significant contributor to the defect creation. The extended model had much lower temperatures towards the centre of the cell. This may be due to the fact that the electron-phonon coupling was proportional to the carrier concentration, and as this concentration quickly diffused throughout the cell, the energy transferred from the carriers to the lattice was more spatially homogeneous (while also being lower in overall magnitude). This also results in higher lattice temperatures at the edges of the cell during the very initial stages of temperature evolution (0.5 ps). The lower amount of energy transferred from the carriers to lattice was the most significant reason for a lack of observed damage at 30 keV/nm using the extended model. This result is further highlighted in figure 5.6, which contains the cross sectional lattice temperatures at various times in both models. Thus it is clear to see that the extended model will lead to significantly less defects when compared to the regular model.

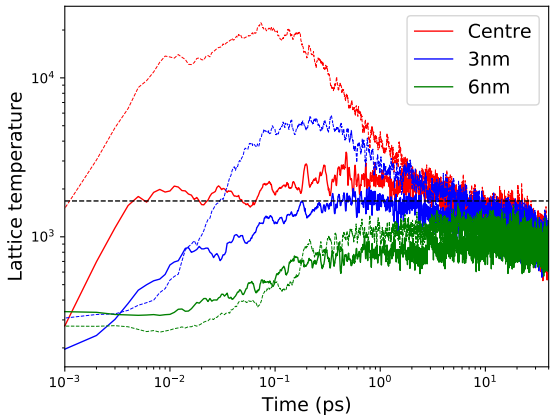

Figure 5.5: Comparison of lattice temperature evolutions in the extended and regular 2T-MD model when irradiatied by a 30 keV/nm SHI. The dotted line represents the regular model, and the solid line represents the extended model. The horizontal black dashed line is the melting temperature for Si using the MOD interatomic potential.

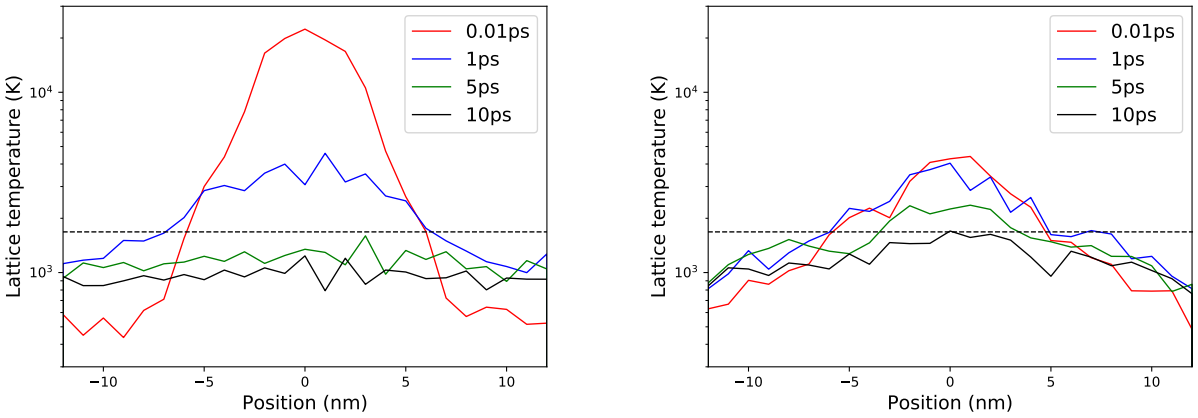

(a) Regular 2T-MD lattice temperature cross-sections at various times.

(b) Extended 2T-MD lattice temperature cross-sections at various times.

Figure 5.6: Comparison of the lattice temperature cross-sections in the regular and extended two-temperature MD model. A wider region of the lattice exceeded the melting temperature in the regular model, however temperature across the extended cell remained higher for a more sustained period of time (facilitating recrystallisation). The horizontal dashed line corresponds to the melting temperature of the Si potential.

5.2.3 Defect evolutions

In addition to the evolution of carrier and lattice temperatures being significantly different in the regular and extended models, ion track formation was also strongly modified when explicit carrier dynamics were taken into account. In the regular model, the ion track was established extremely quickly, this process takes significantly longer in the extended model. This is illustrated in figure 5.7 (b), where the initial disorder did not quickly amorphise the centre, but first disordered the structure to short ranged diamond structure. Comparing figure 5.7 (c) and (d) to the corresponding plots in the previous chapter also strongly suggests that there is a more significant proportion of recrystallisation in the extended model.

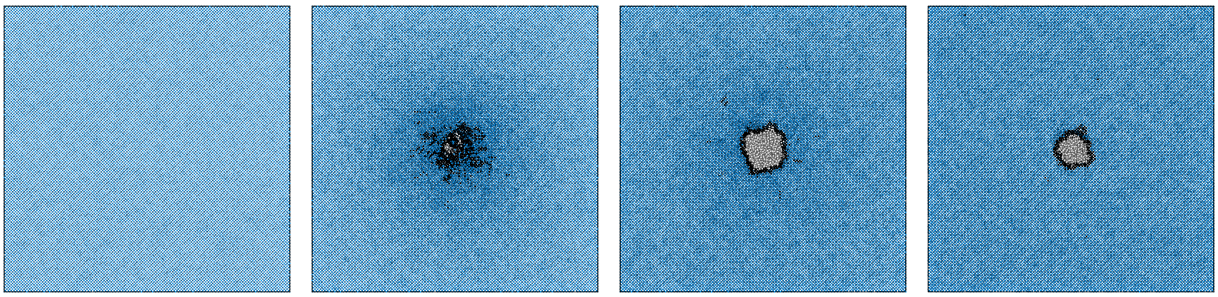

(a) 0.0ps (b) 0.5ps (c) 5ps (d) 50ps

Figure 5.7: [001] ion track morphology at various times during a 35 keV/nm SHI simulation using the extended 2T-MD model. Atoms are coloured according to local structure : blue atoms represent perfect diamond, black are 1st or 2nd nearest neighbours to diamond, and grey represents unstructured amorphous regions.

Figure 5.8 quantifies this defect evolution. Defects were identified according to a Wigner-Seitz analysis of the MD cell (described in detail in the previous chapter). In the regular model, the maximum defect distribution was established within a picosecond, in the extended model, this occured around 5 ps. Also, while only 10% of defects recombined in the regular model, over 50% recombined with the extended implementation. The rate at which this final distribution was established also differed. This happened within 5 ps for the regular model, but was closer to 40 ps for the extended model. These discrepancies are extremely significant, and emphasise another key difference between the extended and regular 2T-MD model when applied to the study of band gap materials. This high level of recombination

(compared to the regular model) may be explained by the more homogeneously distributed lattice temperature profile. These homogeneously distributed temperatures may have more easily facilitated the recrystallisation of defects back to their original diamond structure. It is also interesting to note that the differences in the number of residual defects observed with and without a boundary thermostat (Langevin thermostat with 2 ps relaxation time) applied to the lattice system was minimal, implying the thermostat is not significantly driving the creation or recombination of defects.

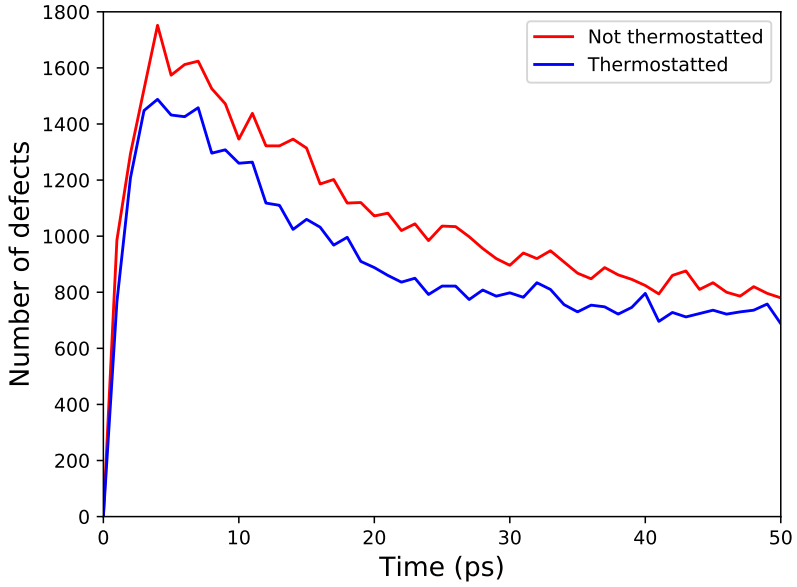

Figure 5.8: Evolution of Wigner-Seitz defects in silicon when irradiated by a 35 keV/nm SHI using the extended 2T-MD model with and without applying a thermostat to the boundary of the lattice. Over 50% of the defects created end up recombining by the end of the simulation in both cases, with a similar final distribution observed.

One area where both implementations of the model did agree, was on the profile of the track created after irradiation. Two distinct track profiles emerged, at low electronic stopping powers, the track consisted of an overly dense amorphous region. As this deposited energy increased, the track profile was an initially overdense region, with an underdense core. This is consistent with the melting properties of silicon, whose amorphous density is greater than its diamond structure (see previous chapter).

The final comparative analysis between the two incarnations of the two-temperature model was the determination of ion track formation for a variety of electronic stopping powers. The values presented for the extended model utilised the pseudo-thermostat described previously (however the differences in the final track radii observed in both were negligible). All of the evidence presented thus far predicts that fewer defects are produced by extended model simulations. However, the results did not turn out to be so simple. Figure 5.9 reveals the differences in ion track formation between both models. Ion track formation did not occur at 30 keV/nm with the extended model, and at 35 keV/nm, the extended model produced an ion track radius more than three times smaller than its regular counterpart. This difference decreases with increasing stopping power, and at 60 keV/nm the extended model generated a larger ion track. This linear increase in the track radii in the extended model differs from both the regular 2T-MD (when a specific heat derived from density functional theory is utilised), and experiment observations of track radii in band gap materials [8, 135, 13, 136, 5, 58].

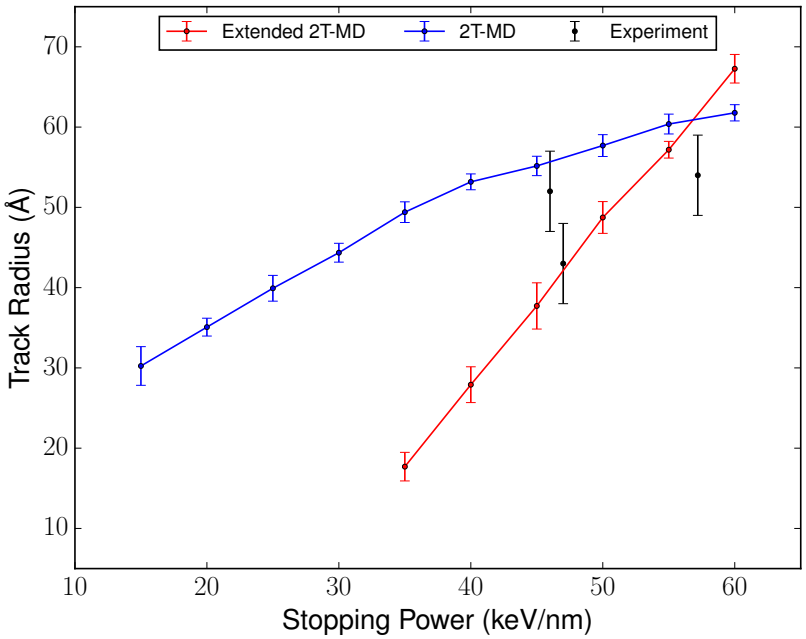

Figure 5.9: Sensitivity of ion track formation vs electronic stopping power in the regular and extended two-temperature molecular dynamics model.

This discrepancy lies in how this implementation of the extended model treats the carrier-specific heat capacity, $C_{e-h} \approx 3Nk_B$ (as $\frac{dE_g}{dT_e}$ is assumed to be zero in the first iteration of this model implementation for simplicity), a linear proportionality with carrier concentration. In contrast, the electronic-specific heat derived with DFT is far from linear (see previous chapter). So as the electronic stopping power increases (ie - more energy deposited into the electronic subsystem), the translated temperature increase of the electrons saturates, causing a non linear relationship between stopping power and track radii. A way of improving the model would be to relate this carrier specific heat, with the previously derived specific heat from DFT. This will impose a limit on the generation of carriers following irradiation, and is described by Shokeen *et al* [99]. Thus in utilising the extended 2T-MD model, a number of significant differences are observed when simulating band gap materials.

5.3 Conclusions and summary

In this chapter the analysis of ion track formation in silicon was examined, within the context of a hybrid atomistic-continuum extended two-temperature model formalism. A comparison with the regular 2T-MD model was highlighted throughout, as this version of the model is by far the most widely adopted within the swift heavy ion community. The extended implementation expands on the regular two-temperature model by explicitly accounting for carrier generation (and subsequent conservation). First, the influence of the carrier recombination terms, impact ionisation, and Auger recombination were investigated. Impact ionisation was observed to have no influence on the number of carriers in a simulation, thus it had no impact on the formation of ion tracks. Auger recombination was shown to influence the carrier concentration (decreasing the total number of carriers), this translated to an increase in the kinetic energy of the carrier system. This increase in carrier energy did not translate to an appreciable difference in lattice temperature, as the electron-phonon strength is determined by both the local temperature of carriers and their concentration. Thus it appeared that a significant part of the extended model (processes that produce and destroy excited carriers), plays no part in the formation of ion tracks. This does not negate their importance though, as it is plausible that an accurate temperature (or specifically carrier density) dependent electron-phonon coupling will make these processes more pronounced.

Next the key dynamics that drive both models were explored. This highlighted the central difference between the models, namely that the extended model is concerned with tracking the evolution of carriers. This is manifested in a comparison of the carrier (or electronic) temperatures. In the regular model, the energy of the electrons (described by T_e) is the evolved quantity. However when this is compared to the extended model, the corresponding carrier temperatures seem too high. This is because the carrier temperatures in the extended model only describe carriers that have already been excited, not the entire local cell. Thus an excited carrier temperature of 10 000 K at the edges of the MD cell correspond to such a low carrier density that they do not transfer any appreciable amount of energy to the lattice via electron-phonon coupling, and thus are exempt of contributing to track formation. This was verified in the corresponding lattice temperatures at the edges of the cells, they never reached anomalously high values.

Finally the morphologies and creation of tracks were compared in both models. While the final ion track morphologies in both models are the same (a characteristic that may be identified in future SAXS experiments), the path to formation differed significantly. In the extended model, the track takes five times longer to reach a maximum number of defects, and also nearly five times longer to relax to a final distribution. Over 50% of the defects also annihilated in this time frame. For low and medium range electronic stopping powers, the track radii formed in the extended model are appreciably lower than their regular analogue. However, due to the linear relation of the carrier-specific heat and carrier concentration ($C_{e-h} \approx 3Nk_B$), at higher stopping powers the extended model predicts larger track radii. This also contradicts experimentally observed track radii measurements, but can be rectified via the incorporation of a carrier-specific heat derived from density functional theory [99].

Following this summary, and the main research motivation behind studying this more complicated model, poses the question : does the use of this extended model lead to significantly different physics that cannot be captured by the regular model? The answer is yes, however there is a big caveat, and that is the model requires further development. The disadvantages include all of the same disadvantages as the regular model, namely that the parameterisation is difficult, as all the parameters (of which there are now significantly more) will have a complex temperature dependence. This work also showed that the terms which contributed to carrier concentration had no impact on the track formation. The implemen-

tation of the solver for the carrier subsystem is also significantly more complicated, as there are two conserved differential equations. This computational complexity meant the carrier subsystem and lattice being disconnected after 4 ps. This is another key difference with the regular model, as a pseudo-thermostat (an extra tunable hyperparameter) had to be applied to the boundaries of the lattice so as to not confine energy indefinitely. Finally, and possibly most significantly, it is highly unlikely that even the ground state parameters of the model will be available for a wide array of band gap materials in the near future, so the possibility of applying the model to the most easily damaged insulators is unlikely for now. The main advantage of the model is that it is a physically realistic representation of the dynamics that occur following electronic excitation in band gap materials. In theory, it makes no naive approximation of how carriers behave. This work also shows that despite the numerous approximations in the parameterisation, there is a significant difference between the track sizes found using both models, which is an important result.

Ultimately the answer to the question will be highly material dependent. If one is researching a well characterised semiconductor (eg - silicon or germanium), the extended model's ability to capture more accurate swift heavy ion physics means it is more physically realistic. For other materials, the less complicated regular 2T-MD model, with well characterised electronic-specific heats, and electron-phonon couplings may capture enough of the essential dynamics to provide an important simulation tool in the modelling of swift heavy ion irradiation of band gap materials.

6

The influence of T_e dependent interatomic potentials

> "Physics is actually too hard for physicists."
>
> David Hilbert

Recent ultrafast laser irradiation experiments have shown that certain materials undergo significant structural modifications in regions of high electronic excitation, on timescales which cannot be accounted for by electron-phonon coupling in the two-temperature model. This is due to the change (softening or hardening) of phonon modes in a material, caused by a modified electron density. These non-adiabatic forces may prove important in swift heavy ion simulations, and while they can be accounted for in *ab initio* simulations, the dimensions required for meaningful results are impossible to simulate with current computational resources. While these may still suffer from the same shortcomings as other high temperature DFT methods, their inclusion has never investigated in the context of swift heavy ion simulations. The most natural way to account for these effects would be in the creation of a dynamic empirical MD potential, which is parameterised according to electronic temperature, instead of utilising the ground state potential.

The vast majority of published research on radiation damage simulations that cause significant levels of electronic excitation (including all studies on swift heavy ions), within the context of molecular dynamics, completely neglect how these interatomic forces are modified due to this excitation. This oversight is due to the difficulty in deriving electronic temperature dependent interatomic potentials. In fact only a handful exist today [39, 38, 40, 41]. This chapter hopes to address how significantly these non-adiabatic forces modify the ther-

modynamics of swift heavy ion irradiation, and whether they contribute to track formation in two materials : tungsten and silicon.

Tungsten was the first material chosen for investigation. Firstly this was motivated by past research which predicted the possiblity of a solid-solid phase transition (bcc to fcc) in Tungsten for an electron temperature between 1.7 eV and 4.3 eV [145]. This prediction was based on the calculation of phonon modes for various tungsten structures (fcc, bbc, and hcp) at a range of electronic temperatures. Fcc tungsten was found to be more stable in the previously mentioned temperature range than bcc, hence the prediction of an adiabatic phase change. These electronic temperatures are easily achieved in swift heavy ion simulations. The second important motivation was that these T_e-dependent interatomic potentials actually exist for tungsten [40, 38]. Finally, previous work in this thesis addressed the how the regular 2T-MD capably accounted for the defects observed in metallic systems, the incorporation of these dynamic interatomic potentials will mark another significant step forward, at least in the context of the two-temperature formalism. The graphs produced for tungsten in this chapter were produced by Oscar Knagg, an undergraduate student that I supervised for his final year research project.

Silicon was the other material investigated. Recently electronic temperature dependent potentials [39] were implemented using the ground state MOD potential [109], a potential that reproduces the bulk properties of silicon most relevant to SHI irradiation well. This allowed for a thorough exploration of how significantly these dynamic potentials contribute to, not only a band gap material, but a band gap material that increases in density as it melts. This latter point is important, as recent research suggests that the influence of these non-adiabatic forces resulting from strong electronic excitation are only able to be physically manifested in materials that adhere to this density increase on melting [146]. Thus the study of a metal and semi-conductor, both with distinct melting characteristics, allows for an analysis of how critical these non-adiabatic forces are to defect formation following high levels of electronic excitation. A number of studies have shown that the melting temperature of certain materials is hugely decreased by electronic excitation, whether this proves to be the case on the timescales relevant for SHI irradiation could prove important for future materials engineering.

6.0.1 Electronic system

The key parameters that determine the temperature evolution of the electronic subsystem in metals are the electronic thermal conductivity, κ_e, the electronic specific heat capacity, C_e, the electron-phonon coupling, G_e, and deposition profile of the incoming SHI, A. The thermal conductivity was taken to be a constant, and the electron-phonon coupling and electronic specifc heat capacity have an explicit electronic temperature dependence. The spatial variation of the thermal conductivity and electronic specific heat in equation 6.1 were ignored.

$$\frac{\partial T_e}{\partial t} = \underbrace{\frac{\kappa_e(T_i)}{C_e(T_e)}}_{(a)} \nabla^2 T_e - \underbrace{\frac{G_e(T_e)}{C_e(T_e)}}_{(b)}(T_e - T_i) + \underbrace{\frac{A(r,t)}{C_e(T_e)}}_{(c)}, \tag{6.1}$$

(a) in equation 6.1 dictates how quickly temperature diffuses throughout the electronic subsystem, (b) is the electron-phonon strength, and dictates the rate of energy exchanged with the lattice subsystem, and (c) dictates how excited the electronic subsystem becomes subsequent to SHI irradiation. The electronic temperature dependence of C_e and G_e n W was obtained from previous work carried out by Lin *et al* [44]. The constant electronic thermal conductivity was taken to be $106\,\mathrm{Wm^{-1}K^{-1}}$ from experimental value of material at 1600 K [122]. This experimental value corresponds to the total thermal conductivity (made up of a lattice and electronic component), however, in metals the electronic component dominates, so this was a reasonable assumption. The source term, $A(r,t)$, had a characteristic spatial Gaussian deposition with a standard deviation of 1 nm, and temporally decaying exponential with a decay time of 1 fs. The source term was normalised so its spatial and temporal integration equates to the energy deposited into the electronic system (the electronic stopping power, $\mathrm{S_e}$).

The parameters governing the silicon simulations were also described previously in chapter 5, and are summarised below.

$$\frac{\partial T_e}{\partial t} = \underbrace{D_e(T_e)}_{(a)} \nabla^2 T_e - \underbrace{\frac{G_e}{C_e(T_e)}}_{(b)}(T_e - T_i) + \underbrace{\frac{A(r,t)}{C_e(T_e)}}_{(c)}, \tag{6.2}$$

The parameterisation of the electronic system for silicon was the same as described in chap-

ter 4. The electronic temperature dependent specific heat capacity was derived from finite temperature density functional theory, and utilised the HSE hybrid functional. The electron-phonon relaxation time (the key parameter in governing the electron-phonon coupling) was taken to be 0.26 ps, a value obtained from femtosecond optical pump probe reflectivity experiments [66]. This quantity was assumed to remain constant throughout the simulations. The temperature dependent diffusivity also followed the previously described model by Dufour *et al* [45]. the source term was based on the properties of a C_{60} cluster with specific energy 0.07 MeV/u : a Gaussian deposition with a standard deviation of 0.74 nm, and temporally decaying exponential with a standard deviation of 1 fs.

6.0.2 Interatomic potential properties

Up until this point, all of the swift heavy ion irradiation results presented in this thesis utilised a ground state interatomic potential, which remained fixed regardless of the level of electronic excitation. This chapter aims to investigate how signficantly structural dynamics are affected by T_e dependent MD potentials. Electronic temperature dependence was built into the tungsten cell via the method described by Murphy *et al* [38] and was achieved by modifying the embedding term in the extended Finnis-Sinclair [106].

$$F(\rho_i, T_e) = A^{DFT}(\rho_i, T_e) + dE(T_e) - \frac{1}{2}\sum_{i=1}^{N}\sum_{j\neq i}^{N} V_{ij}(r_{ij}) \tag{6.3}$$

$F(\rho_i, T_e)$ is new embedding term, dependent on the local density, ρ_i, and the electronic temperature, T_e. A^{DFT} is the free energy calculated via DFT, dE is the constant energy shift at each electronic temperature so the energy splines to zero at infinity, and V_{ij} is the repulsive potential between atoms i and j. Thus, via the use of finite temperature density functional theory, a temperature dependent embedding term is fit to the free energy volume curves, yielding a T_e dependent potential. As the electronic temperature is increased, tungsten exhibits a number of structural modifications, the lattice parameter increases, and the melting temperature decreases. The potential turns completely repulsive at 30 000 K [38]. The decrease in melting temperature is highlighted in figure 6.1.

The silicon T_e dependent potentials [39] are constructed such that the functional form of

the empirical potentials reproduce the DFT cohesive free-energies for the diamond, fcc, bcc and simple cubic structures at several different volumes. The functional form of the potential is assumed to remain unchanged under this electronic excitation, with each constituent parameter varying as a sixth order polynomial;

$$\Psi(T_e) = \sum_{n=0}^{6} a_n (k_B T_e)^n \tag{6.4}$$

Here Ψ represents any of the default MOD parameters, and a_n is the polynomial coefficient. Silicon, similarly to tungsten, exhibits a gradual decrease in melting point when subjected to significant levels of electronic excitation. This is highlighted in figure 6.1.

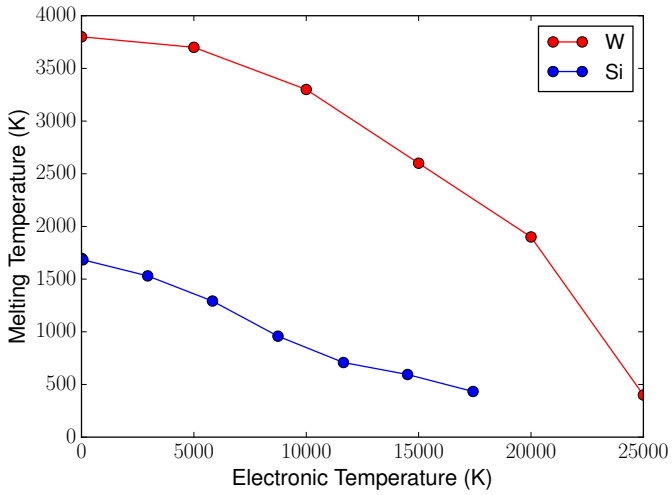

Figure 6.1: Melting point of W and Si as a function of the electronic temperature [38, 111], calculated using the moving interface method [147].

6.0.3 Simulation setup

Two different tungsten cells were constructed, one for lower stopping powers ($\leq 60\,\mathrm{keV/nm}$), and one for high stopping powers. Both were constructed from a two atom basis, the small consisted of 204,800 atoms (made of 80x80x16 repetitions of the basis), and the large con-

sisted of 460,800 atoms (120x120x16). These cells were initially equilibrated using an NPT ensemble, at 300 K and 1 atm for 200 ps. This ensured the equilibrium structure was obtained, with resulting cell dimensions of approximately 250x250x50 Å^3 and 370x370x50 Å^3, with periodic boundary conditions. For the 2T-MD implementation the lattice was discretised into coarsed grained ionic temperature cells (CIT), each with a volume of roughly 1000 Å^3, resulting in 25x25x5 and 37x37x5 CIT cells for the small and large cell respectively. The coarse grained electronic temperature cells (CET) had the same dimension, but extended three times further in the x and y directions, thus the number of CETs were 75x75x5 and 111x111x5. The extension of the CET cells beyond the CIT cells provides a mechanism for the transport of electronic energy out of the central cell. As the swift heavy ion travelled perpendicularly through the centre of the cell, electronic energy was confined via Neumann boundary conditions in the z-direction. The halo region of the extended electronic cells in the x and y direction were governed by Robin's boundary conditions which converged to 300 K. A variable timestep was chosen for the electronic finite difference solver, and 1 fs timestep was chosen for the molecular dynamics timestep. No thermostat was placed at the boundary of the MD cell, thus energy could only escape through the electronic subsystem. Simulations were run for 60 ps. The silicon cell contained the exact same number of atoms as the small tungsten cell (and thus same number of CIT and CET), resulting in a supercell measuring 271.99 x 271.99 x 54.4 Å^3.

One significant issue that was not resolved in this work was energy conservation. While utilising the ground state potential, the electrons and lattice form a closed system. However, the interatomic forces change during the initial stages of electronic excitation when utilising T_e dependent potentials. This was not resolved for the work presented in this chapter, but recent research has overcome this limitation via the derivation of a modified electron-phonon coupling from a Hamiltonian that explicitly includes a T_e dependent potential energy function. However, despite this limitation, the forces are unaffected, so the proceeding results do capture new physics.

6.0.4 Temperature evolutions

The first areas investigated were the temperature evolutions of the respective simulation cells, with and without temperature dependent potentials, of which the results are presented

in figure 6.2. Both materials, using the ground state potential, and T_e dependent potentials, obey the typically established trends described already. The SHI deposited energy into the electrons, causing an initial dramatic increase in the electronic temperature, followed by energy flow to the lattice by electron-phonon coupling. In tungsten the electronic temperature dipped significantly below the lattice, for tens of picoseconds, until both systems reach ambient levels after roughly 50 ps. The electrons and lattice reached thermal equilibrium much faster in silicon, cooling to ambient temperatures together. Figure 6.2 clearly shows that there was no significant differences between the ground state and T_e dependent potential in tungsten, as both the electrons and lattice follow a seemingly identical trajectory. However, the case is dissimilar for silicon, where the T_e dependent potential attains a slightly larger lattice temperature, subsequently causing the cell to cool to a higher temperature after 40 ps. This can be explained by considering the change in interatomic forces proceeding electronic excitation, as the bonds weaken, the atoms are more excited than in comparison to the ground state potential. The electronic temperatures reached by tungsten (which are much lower than in silicon) result in significantly smaller changes in the interatomic forces. This may imply T_e dependent potentials are less influential in W than Si.

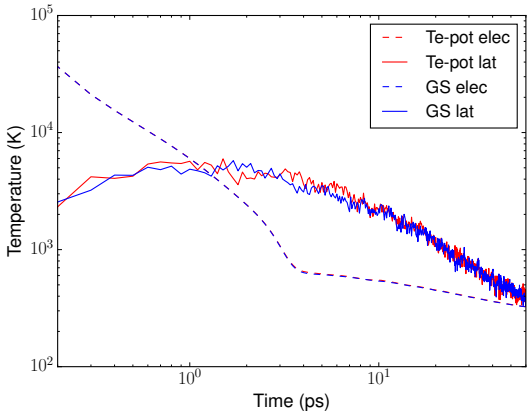

(a) Temperature evolution at the centre of a W cell.

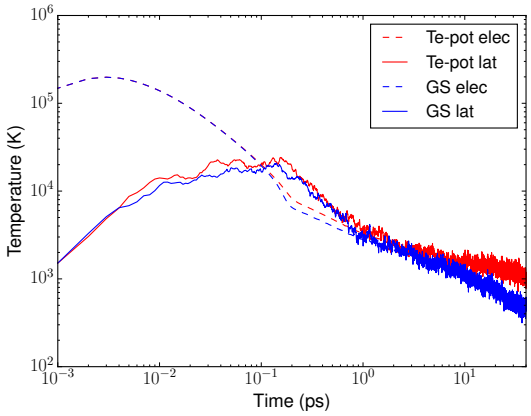

(b) Temperature evolution at the centre of a Si cell.

Figure 6.2: Comparison of temperature evolutions at the centre of a Si and W cell using both the standard ground state potential, and T_e dependent potentials, following irradiation by a 30 keV/nm swift heavy ion.

While it is not obvious from figure 6.2 whether the T_e dependent potential will significantly alter defect creation in tungsten, it appears probably that the same effect will be important in silicon. A look into the cross sectional temperatures (electronic and lattice) showed no noticeable difference between the ground state and temperature dependent case at any moment in the tungsten simulations. There is a much clearer difference is observed for silicon, with figure 6.3 highlighting that although there seems to be a negligible difference in the electronic temperatures with and without the temperature dependent potentials at the beginning of the simulation, the width of excitation is greater in the T_e dependent case. As the simulation runs on, the electronic temperatures at the centre of the T_e dependent simulation also end up exceeding those of the ground state case. This is a very significant difference between the ground state and T_e dependent case. The corresponding lattice temperature cross sections are highlighted in figure 6.4, with same key trends were observed : a wider region of the MD cell is excited. A similar trend verified in the atomic displacements, at the start of the simulation the atoms under the influence of the T_e dependent potentials experienced a far larger proportion of displacements. Thus there is a clear difference in the temperature profiles and lattice displacements of silicon when taking into account these non-adiabatic forces. This indicates that non-adiabatic forces will play a major role when irradiating silicon with SHIs (when using this potential).

After 20 ps, when each lattice is roughly homogenously excited, the T_e dependent lattice temperature is about a thousand Kelvin, whereas the ground state simulation has already cooled to ambient temperatures. These cross sections again highlight that non-adiabatic forces will definitely contribute significantly to defect formation in silicon when it is irradiated by swift heavy ions.

Plots of temperature evolutions on their own are limited, as the melting characteristic of each material (when utilising T_e dependent potentials) is significantly influenced by the local electronic temperature. Thus a good method of highlighting the differences of the ground state and T_e dependent potential, is to plot the degree of overheating (T_i/T_m), for a one dimensional slice of the ionic grid, where T_i is the lattice temperature of the grid point, and T_m is the melting temperature (which will dynamically vary for the T_e dependent case). Figure 6.5 illustrates this degree of overheating for tungsten. Initially there was a clear

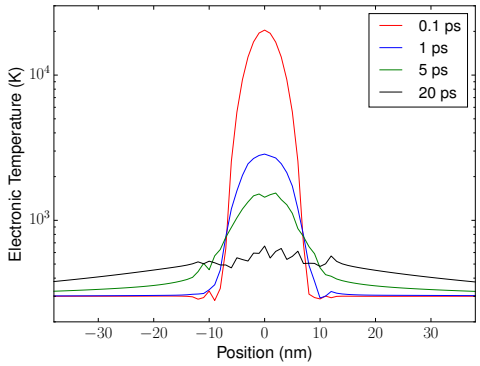

(a) Electronic temperature cross section in silicon with the ground state potential.

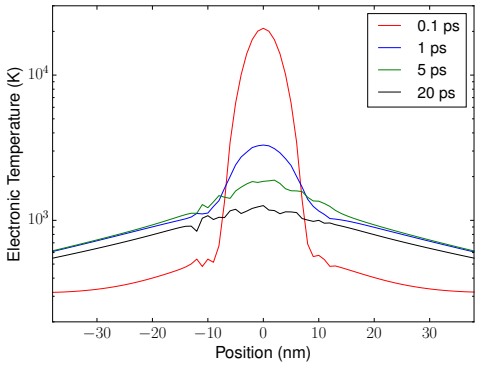

(b) Electronic temperature cross section in silicon with the T_e dependent potential.

Figure 6.3: Comparison of electronic temperature cross section at various times during a 30 keV/nm swift heavy ion irradiation.

difference between the two types of interatomic potential, as after 0.1 ps, a 6 nm region of the T_e dependent lattice exceeded the melting temperature, contrasted with only 1 nm for the ground state. However, as the simulation proceeded, this larger level of overheating begins to decrease, and from 1.0 ps onwards, there is very little difference between both cases.

The equivalent plots for silicon are shown in figure 6.6. Firstly the rate at which the lattice exceeded the melting temperature is much faster in silicon when compared to tungsten. This has been highlighted in previous results chapters for the ground state case, but this trend is accentuated in the T_e dependent case. There is also the same initial wider region of melting when comparing the T_e potential to the ground state (15 nm vs 12 nm after 0.1 ps). However, as the simulations proceeded, this degree of overheating actually begins to increase for the T_e dependent silicon case. In both materials, at the very early stages of the simulation, the electronic temperatures at the core of SHI track become sufficiently high that the potentials become completely repulsive and the melting points decrease to zero. This overall repulsion is somewhat reminiscent of the Coulomb explosion model, except that the atoms remain neutral. The reduction in the melting point means that the T_i/T_m exceeds unity more quickly at the heart of the ion track, hastening the disorder. However, as the simulation proceeds this degree of overheating becomes indistinguishable between both types of potential in

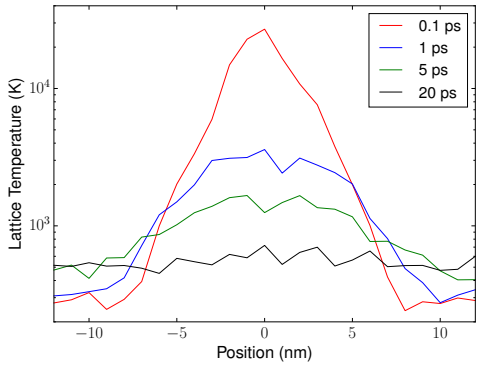

(a) Lattice temperature cross section in silicon with the ground state potential.

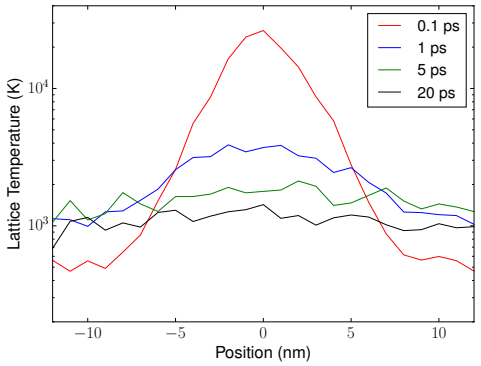

(b) Lattice temperature cross section in silicon with the T_e dependent potential.

Figure 6.4: Comparison of lattice temperature cross section at various times during a 30 keV/nm swift heavy ion irradiation.

tungsten, whereas there are huge differences in silicon throughout the simulation. These results imply that T_e dependent potentials will have a pronounced effect in silicon, while being less noticeable in tungsten.

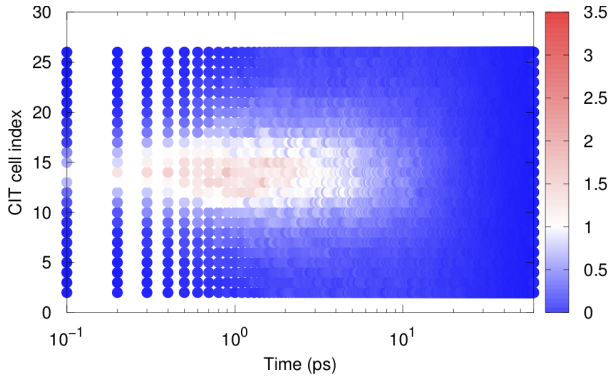

(a) Degree of overheating using the ground state potential for W.

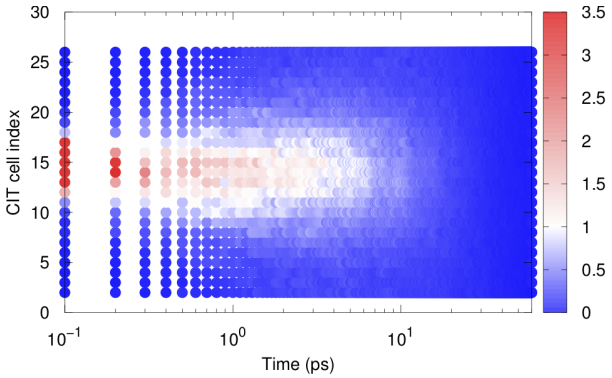

(b) Degree of overheating using the T_e dependent potential for W.

Figure 6.5: Comparison of degree of overheating as a function of time following a 30 keV/nm swift heavy ion irradiation in tungsten. Each coarse grained ionic voxcell (CIT) has a 10 Å diameter.

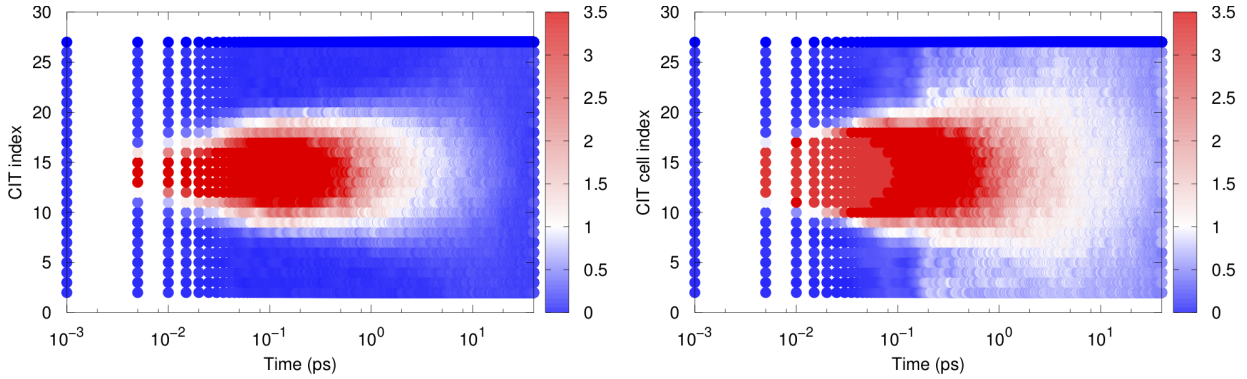

(a) Degree of overheating using the ground state potential for Si.

(b) Degree of overheating using the T_e dependent potential for Si.

Figure 6.6: Comparison of degree of overheating as a function of time following a 30 keV/nm swift heavy ion irradiation in silicon. Each coarse grained ionic voxcell (CIT) has a 10 Å diameter.

6.0.5 Defect evolutions

While the temperature evolutions, and extent to which overheating occurs in the lattice are good indicators of the dynamics of the cell, the explicit defect evolutions are the most important measure of whether these T_e dependent potentials modify ion track formation. Figure 6.7 illustrates how ion track formation in tungsten evolved for both types of potentials by tracking radius of the molten region. This molten radius was calculated as follows, the local structural environment of each atom at every recorded timestep was determined by common neighbour analysis in OVITO [119, 148], resulting in a categorisation of either bcc or molten. Secondly, the fraction of molten atoms in cylindrical shells at various radial distances from the ionic trajectory was counted and the outer radius of the outermost shell containing greater than 90% molten atoms was taken to be the radius of the defect region. The same trend was observed when irradiating the ground state and T_e dependent potential in W : immediately proceeding irradiation a highly disordered region at the centre of the MD cell was observed, and as time evolved the majority of this disorder recrystallised.

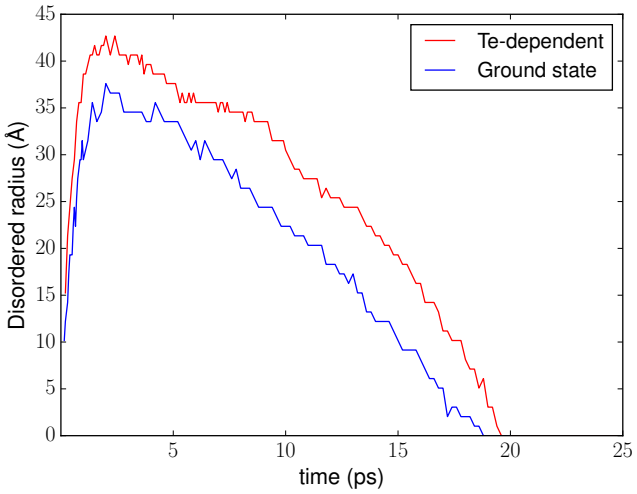

Figure 6.7: Evolution of disordered radius in tungsten when irradiated by a 60 keV/nm SHI. Significant levels of recrystallisation were observed in both. The level of disorder is consistently greater for the T_e potentials, but over 99% of the defects recrystallise, no difference is observed by the end of the simulation.

While the radius of the T_e dependent case is greater, by the end of the simulation the recrystallisation resulted in no discernible difference in the number of residual defects. This result implies that while there are modifications to the bonding characteristic in tungsten by these non-adiabatic forces, but they do not end up contributing to the residual defects formed over tens of picoseconds. This may be due to the shape of the interatomic potentials at these elevated electronic temperatues, where for the majority of the simulation the potential well has not changed significantly enough to impact on the defects created. The morphology of the residual defect distribution was also the same when utilising T_e dependent potentials in tungsten : an outer halo of mainly isolated vacancies (with a few vacancy clusters), surrounding a core made up of interstitial clusters. At stopping powers of 50 keV/nm these interstitial clusters formed dislocation loops with Burger's vectors b = $\frac{1}{2}\langle 111\rangle$ and b = $\langle 100\rangle$. The sensitivity of tungsten to form Wigner-Seitz defects for a variety of electronic stopping powers is highlighted in figure 6.8. The data clearly illustrates that there is no discernible difference in the residual defect distributions formed in tungsten for the ground state extended Finnis Sinclair potential, and the T_e dependent potential. This suggests that

non-thermal effects are effectively negligible for tungsten. This agrees with recent findings by Hu *et al* [146], in which these non-adiabatic forces are unable to manifest themselves significantly in materials which decrease in density upon melting.

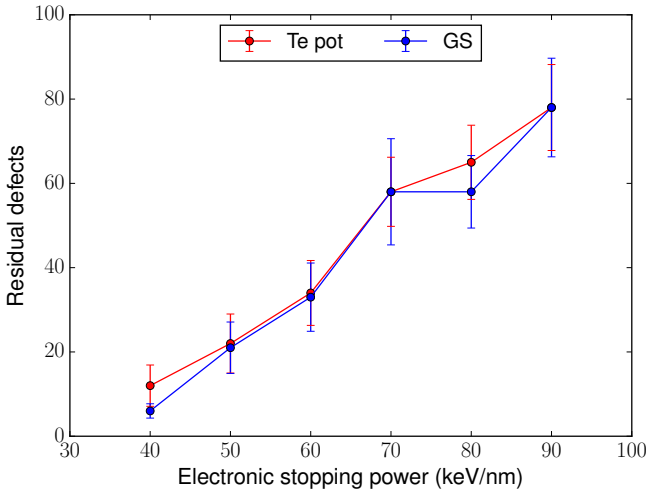

Figure 6.8: The sensitivity of defect creation in tungsten at various electronic stopping powers. The red points highlight defects formed with the T_e dependent potential, and the blue shows results from the ground state potential.

The scenario for silicon is entirely different. Figure 6.9 demonstrates the evolution of Wigner-Seitz defects in a 30 keV/nm SHI simulation in silicon. Firstly there was a huge increase in the overall damage when comparing the T_e dependent potential to the ground state (between 4x and 5x the number of defects depending on where in the simulation you compare). This emphasises the T_e dependent potential causes the bonds to break more easily. The other deviation was in the level of recrystallisation. Earlier it was shown that for the ground state MOD potential, regardless of the energy deposited by the SHI, the same level of recrystallisation occurs in a simulation (roughly 10%). This was again observed for the ground state in figure 6.9. However, there is a much more significant level of recrystallisation for the T_e dependent potential, roughly 25%. This added proportion of recrystallisation can be explained by a wider spatial region of the lattice reaching high temperatures, similarly to the results presented for the extended model.

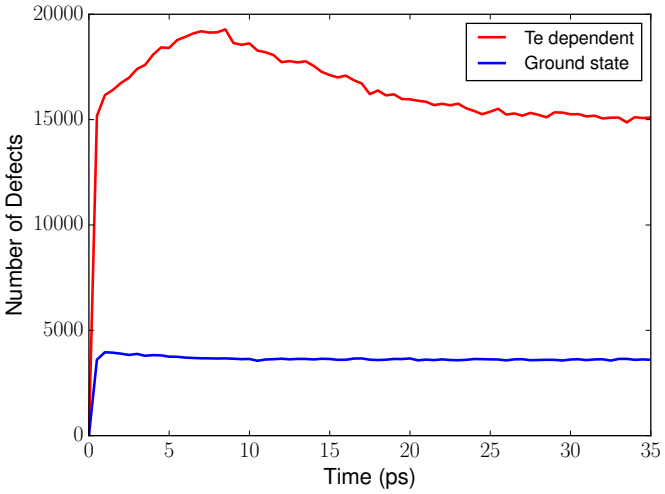

Figure 6.9: Evolution of WS defects in silicon when irradiated by a 30 keV/nm SHI. Significant levels of recrystallisation were only in the T_e dependent case. The level of disorder is also far greater for the T_e potentials. This highlights how significantly the bonding characteristics of silicon are modified in region of high electronic excitation.

Thus the influence of a T_e dependent potential potential in silicon has two key influences following SHI irradiation (when compared to the ground state), firstly, the temperature evolution of the material is highly altered due to the weakened interatomic forces. Secondly, although silicon will be more susceptible to damage overall, during the cooling phase there is also a higher proportion of recrystallisation. The fact that these non-adiabatic forces have such a significant effect in silicon is due to its phase diagram, as silicon contracts when it melts, this effective inward pressure is not inhibited by the lattice, allowing the material to melt (in contrast to W). This postulate has been verified for a number of other materials with this phase behaviour, and is summarised well by Hu *et al* [146].

The final step was to quantify how much more susceptible silicon was to damage with these non-adiabatic forces, for a variety of electronic stopping powers. Figure 6.10 summarises these findings. Both plots illustrate how significantly more residual defects are created when non-adiabatic forces are accounted for in silicon. The number of Wigner-Seitz defects created were up to 10x greater at the low stopping powers, and up to 4x times greater for the higher stopping powers. The corresponding track radii are 3x larger for low stopping powers, and

1.75x for high stopping powers. While the results from T_e dependent potentials overestimate track radii in comparison to experiment, it is important to remember that there are still a number of simplifications in the models, with the most important being a constant electron-phonon coupling. The inclusion of more sophisticated temperature dependent electronic parameters may affect these results significantly.

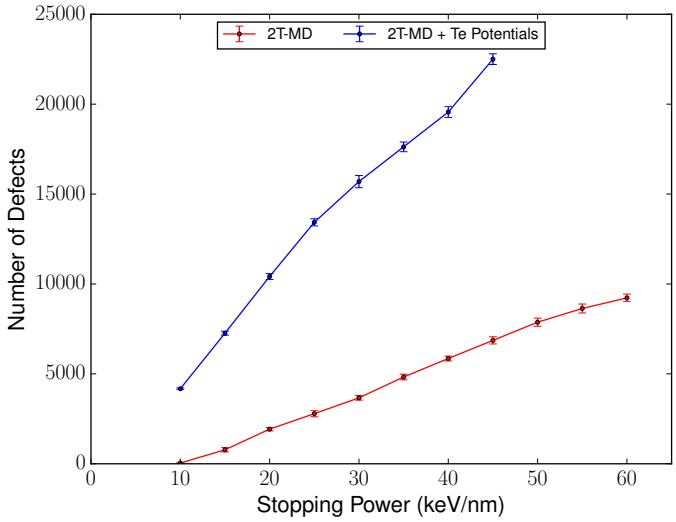

(a) Degree of overheating using the ground state potential for Si.

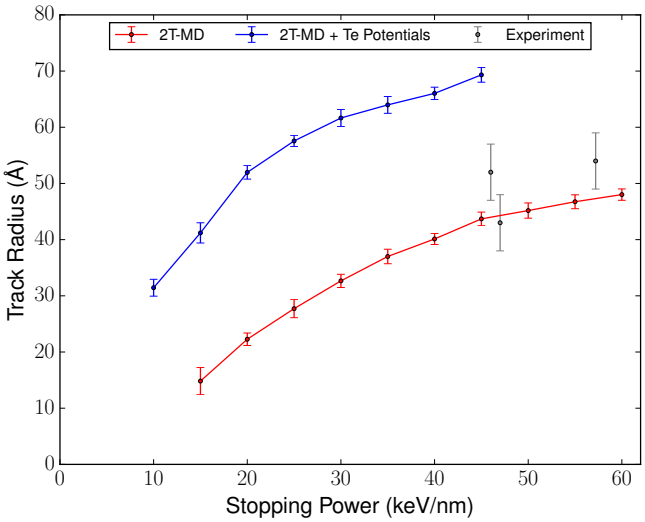

(b) Track radius as a function of stopping power.

Figure 6.10: The sensitivity of defect creation in silicon for a variety of stopping powers. The influence on non-adiabatic forces hugely influenced the residual defect observed.

6.1 Conclusion and summary

Ion track formation resulting from swift heavy ion irradiation in tungsten and silicon was modelled, using the two-temperature molecular dynamics model, including the effects of non adiabatic forces (via the incoporation of T_e dependent interatomic potentials), for a range of stopping powers. The influence of T_e dependent potentials in tungsten was negligible. Some added disorder was observed during the initial stages of irradiation (manifested by a larger track radius in figure 6.7), but over the course of a whole simulation this all recrystallised. While non-adiabatic forces do lead to differences in defect (and temperature) evolutions over the course of a SHI irradiation simulation, they did not manifest in a difference in final observed residual defect morphology.

The evolution of ion track formation in silicon is far more distinct when accounting for non-adiabatic forces. Two properties are observed, with both stemming from the softening of phonon modes in regions of high electronic excitation. Firstly, these non-thermal effects cause a greater number of lattice displacements at the very beginning of the simulations, something that cannot be explained by thermal energy transfer from the electrons to the lattice. Secondly, as the simulations evolve, a much wider region of the electronic system attains high temperature values, which causes the lattice to be more homogeneously excited. These non-adiabatic forces in turn cause much higher levels of residual defects to form. However, there is also a higher level of recrystallisation of defects throughout the cooling phase of the irradiation, which is more than likely due to the more homogeneously excited lattice.

The major conclusion from this work is that when simulating swift heavy ion irradiation, non-adiabatic effects can be ignored in tungsten, but not in silicon. However, this work is still incomplete, as energy was not properly conserved during the application of these non-adiabatic forces. This is left to future research, as a solution is now known.

7

Concluding remarks

> "Nor must we forget that in science there are no final truths."
>
> Clause Levi-Strauss

In summary, via the use of various different implementations of the two-temperature model, swift heavy ion irradiation of metals and band gap materials was investigated in numerous ways. Chapter 3 specifically deals modelling in binary metallic systems. This is an area where the overlap between simulations and real experimental results are closer than for any other materials. This is due to the fact that the 2T-MD model contains accurate non-equilibrium parameterisations for the electronic subsystem. Two bcc metals (iron and tungsten) and two fcc metals (copper and iron) were considered. Distinct dynamics occur in each case, with the underlying causes highlighting the strengths of having accurate computational simulations. In both bcc metals, damage resulted in the formation of interstitial dislocation loops at the centre of the cell, surrounded by a cloud of isolated vacancies. In both cases experimental and simulation results agreed extremely well. This was also true for the fcc metals, which remained defect free, but for two different explainable reasons (due to signficantly different electronic parameterisations). The most exciting result from this research was not necessarily the discovery of novel structures after irradiating bcc metals, but the fact that this formalism of the two-temperature model was capable of accurately describing a variety of different physical effects. The two-temperature model still has its critics, but the results in this chapter are a significant positive endorsement for its ability to model SHI irradiation (and more generally electronic excitation) in metals. Looking towards the future, the most exciting prospect is the application of the model to more exotic alloy structures,

which could lead to the engineering of metals that exhibit invaluable physical characteristics. The main obstacle in this research is the accurate parameterisations of the electronic and lattice system. Robust DFT pseudopotentials for these complex metallic mixtures would be the first step in aiding this progression.

Chapter 4 aimed to explore how well the initial 2T-MD model (developed for metals) could explain SHI excitations in band gap materials. This is important as the vast majority of materials irradiated with SHI for engineering and industrial applications are materials with band gaps. Si was chosen as it is the most accurately parameterised semi-conductor. The fundamental premise of the work is that band gap effects can be incorporated if using a robust temperature dependent electronic specific heat. The current most accurate methods of calculating these are emplot DFT, however traditional DFT pseudopotentials are notorious for over or under predicting the band gap of Si. Thus three pseudopotentials (one that overestimated, one that underestimated, and one that accurately estimated) the band gap of Si were used to derive the electronic-specific heat. The defect distribution observed using the most accurate C_e agreed well with the little experimental data that exists. However, these did not include rigorous non-equilibrium parameterisations of the diffusivity, electron-phonon coupling, and interatomic potential. The two most significant findings of the work were, firstly, that the incorporation of well parameterised C_e does indeed capture band gap effects (whether this is sufficient to be accurate is a question for the future). The trend being that the larger the band gap, the more resistant the material is to defect creation (given the other parameters remain the same). Secondly, as this relationship between band gap and defect creation is observed, caution must be exercised when using a C_e derived from DFT. The over or underestimation of the band gap will cause a significant deviation from the real physical results.

Chapter 5 attempted a similar evaluation for Si, this time using the extended 2T-MD model. This model expands on the original formalism to account for the band gap and carrier dynamics explicitly. However, this is accounted for by the addition of a significant amount of extra complexity, both from a parameterisation and computational stand point. The inclusion of this extra physics led to different results when compared to the regular model, namely that for most stopping powers, the extended model resulted in less residual defects. However, a like for like comparison is difficult to make, as the extended model has

much less well established non-equilibrium parameters. Short term beneficial research should centre on making the model more computationally efficient, followed by attempts at more robust parameterisations in the longer term. Before beginning this research, a key question centred on whether the extended model is actually better than the regular version for band gap materials. Unfortunately there is no satisfying definitive answer to this question. It all comes down to what is needed (and expected). While the extended model explicitly captures carrier physics, in the near future it is hard to imagine a well parameterised band gap material other than the most conventional. However, with further development, it may be able to overcome the criticisms levelled at the regular 2T-MD.

Chapter 6 dealt with a phenomena not yet explored within the SHI community, the effects non-equilibrium conditions have on MD interatomic potentials. Past experiments have established that a change electronic density following excitation can lead to significant structural changes in the lattice of materials. This effect was explored for a metal (tungsten) and a semiconductor (silicon), as these are some of the few materials in which T_e dependent interatomic potentials actually exist. While slightly different defect evolutions were observed in tungsten over the duration of a simulation, the final residual defect structures were indistinguishable. The effects were much more pronounced in silicon, with larger atomic displacements observed at the start of the simulation (due to weakening of the interatomic forces), and a more homogeneously excited lattice overall. This, in turn, led to a significantly higher level of residual defects, and a higher proportion of recrystallisation, proving that non-adiabatic forces are non-negligible for silicon. The most immediate future step would be to fix the energy conservation problem as the interatomic forces changes. This has been solved by colleagues, and will be published shortly. However, from a more general stand point, the most important result from this research is that these non-adiabatic forces can play a signficant influence in SHI irradiation, something the community needs to consider when employing ground state potentials.

While models have attempted to capture the non-equilibrium physics of SHI irradiation for decades, it is only recently that they have become mature enough to not require fitting to experimental ion track results. This marks a significant paradigm shift across the boundary where enough realistic physics is baked into the models. As this progression leads to more sophisticated models, specifically in the coming years, the 2T-MD (and it's extended model)

represents the best balance between capturing quantum mechanical effects accurately, and computationally being able to simulate millions of particles over hundreds of picoseconds. Until the expense of *ab initio* methods becomes tractable over this spatiotemporal range, the 2T-MD model will play a crucial role in furthering our understanding of SHI irradiation (and more generally any form of radiation that causes electronic excitation).

Bibliography

[1] D. A. Young. Etching of radiation damage in lithium fluoride. *Nature*, 182(4632):375, 1958.

[2] A. Meftah, F. Brisard, J. M. Costantini, M. Hage-Ali, J. P. Stoquert, F. Studer, and M. Toulemonde. Swift heavy ions in magnetic insulators: A damage-cross-section velocity effect. *Physical Review B*, 48(2):920, 1993.

[3] P. Kluth, C. S. Schnohr, O. H. Pakarinen, F. Djurabekova, D. J. Sprouster, R. Giulian, M. C. Ridgway, A. P. Byrne, C. Trautmann, D. J. Cookson, K. Nordlund, and M. Toulemonde. Fine structure in swift heavy ion tracks in amorphous SiO2. *Physical Review Letters*, 101(17):175503, 2008.

[4] M. Toulemonde, S. Bouffard, and F. Studer. Swift heavy ions in insulating and conducting oxides: tracks and physical properties. *Nuclear Instruments and Methods in Physics Research Section B: Beam Interactions with Materials and Atoms*, 91(1):108, 1994.

[5] B. Afra, M. D. Rodriguez, C. Trautmann, O. H. Pakarinen, F. Djurabekova, K. Nordlund, T. Bierschenk, R. Giulian, M. C. Ridgway, G. Rizza, N. Kirby, M. Toulemonde, and P. Kluth. SAXS investigations of the morphology of swift heavy ion tracks in α-quartz. *Journal of Physics: Condensed Matter*, 25(4):045006, 2013.

[6] G. Szenes, Z. E. Horváth, B. Pécz, F. Pászti, and L. Tóth. Tracks induced by swift heavy ions in semiconductors. *Physical Review B*, 65(4):045206, 2002.

[7] F. F. Komarov, P. I. Gaiduk, L. A. Vlasukova, A .J. Didyk, and V .N. Yuvchenko. Track formation in germanium crystals irradiated with superhigh-energy ions. *Vacuum*, 70(2):75, 2003.

[8] A. Colder, B. Canut, M. Levalois, P. Marie, X. Portier, and S. M. M. Ramos. Latent track formation in GaAs irradiated with 20, 30, and 40 MeV fullerenes. *Journal of Applied Physics*, 91(9):5853, 2002.

[9] M. Toulemonde, J. Dural, G. Nouet, P. Mary, J. F. Hamet, M. F. Beaufort, J. C. Desoyer, C. Blanchard, and J. Auleytner. High energy heavy ion irradiation of silicon. *Physica Status Solidi (a)*, 114(2):467, 1989.

[10] M. Karlušić, S. Bernstorff, Z. Siketić, and B. Šantić. Formation of swift heavy ion tracks on a rutile TiO2 (001) surface. *Journal of Applied Crystallography*, 49(5):1704, 2016.

[11] M. Levalois, P. Bogdanski, and M. Toulemonde. Induced damage by high energy heavy ion irradiation at the GANIL accelerator in semiconductor materials. *Nuclear Instruments and Methods in Physics Research*, 63, 1992.

[12] W. Wesch, A. Kamarou, and E. Wendler. Effect of high electronic energy deposition in semiconductors. *Nuclear Instruments and Methods in Physics Research Section B: Beam Interactions with Materials and Atoms*, 225(1):111, 2004.

[13] T. Bierschenk, R. Giulian, B. Afra, M. D. Rodriguez, D. Schauries, S. Mudie, O. H. Pakarinen, F. Djurabekova, K. Nordlund, O. Osmani, N. Medvedev, B. Rethfeld, M. C. Ridgway, and P. Kluth. Latent ion tracks in amorphous silicon. *Physical Review B*, 88(17):174111, 2013.

[14] J. Vetter, R. Scholz, D. Dobrev, and L. Nistor. HREM investigation of latent tracks in GeS and mica induced by high energy ions. *Nuclear Instruments and Methods in Physics Research Section B: Beam Interactions with Materials and Atoms*, 141(1):747, 1998.

[15] H. Dammak and A. Dunlop. TEM observations of iron and nickel foils irradiated by MeV fullerenes at room temperature. *Nuclear Instruments & Methods in Physics Research Section B-Beam Interactions with Materials and Atoms*, 146(1-4):285, 1998.

[16] A. Dunlop, P. Legrand, D. Lesueur, N. Lorenzelli, J. Morillo, and A. Barbu. Phonon soft modes and damage production by high electronic excitations in pure metals. *Europhysics Letters (EPL)*, 15(7):765, 1991.

[17] C. L. Dube, P. K. Kulriya, D. Dutta, P. K. Pujari, Y. Patil, M. Mehta, P. Patel, and S. S. Khirwadkar. Positron annihilation lifetime measurement and X-ray analysis

on 120 MeV Au+7 irradiated polycrystalline tungsten. *Journal of Nuclear Materials*, 467:406, 2015.

[18] A. Dunlop, D. Lesueur, P. Legrand, H. Dammak, and J. Dural. Effects induced by high electronic excitations in pure metals: a detailed study in iron. *Nuclear Instruments and Methods in Physics Research B*, 90:330, 1994.

[19] A. Iwase, S. Sasaki, T. Iwata, and T. Nihira. Anomalous reduction of stage-I recovery in nickel irradiated with heavy ions in the energy range 100–120 MeV. *Physical Review Letters*, 58(23):2450, 1987.

[20] P. Apel. Swift ion effects in polymers: industrial applications. *Nuclear Instruments and Methods in Physics Research Section B: Beam Interactions with Materials and Atoms*, 208:11, 2003.

[21] N. Choudhury, F. Singh, and B. K. Sarma. Effect of swift heavy ion irradiation on lead sulfide quantum dots embedded in polyvinyl alcohol. *Radiation Effects and Defects in Solids*, 168(7-8):498, 2013.

[22] G. Devaraju, N. Sathish, A. P. Pathak, A. Turos, M. Bazzan, E. Trave, P. Mazzoldi, and B. M. Arora. Effects of swift heavy ion irradiation on band gap of strained AlGaN/GaN Multi Quantum Wells. *Nuclear Instruments and Methods in Physics Research Section B: Beam Interactions with Materials and Atoms*, 268(19):3001, 2010.

[23] J. Wiesner, H. Fueβ, G. Wirth, E. Jäger, E. Schimpf, P. Wagner, F. Hillmer, and H. Adrian. Heavy-ion-induced effects on the transport critical current density in epitaxial 2212-BSCCO thin films. *Physica C: Superconductivity*, 235:2971, 1994.

[24] G. Rizza. From ion-hammering to ion-shaping: an historical overview. *Journal of Physics: Conference Series*, 629(1):012005, 2015.

[25] K. H. Bennemann. Ultrafast dynamics in solids. *Journal of Physics: Condensed Matter*, 16(30):R995, 2004.

[26] J. F. Ziegler, M. D. Ziegler, and J. P. Biersack. SRIM – The stopping and range of ions in matter. *Nuclear Instruments and Methods in Physics Research Section B: Beam Interactions with Materials and Atoms*, 268(11-12):1818, 2010.

[27] R. L. Fleischer, P. B. Price, and R. M. Walker. Ion explosion spike mechanism for formation of charged-particle tracks in solids. *Journal of Applied Physics*, 36(11):3645, 1965.

[28] Y. Cherednikov, S. N. Sun, and H. M. Urbassek. Hybrid particle-in-cell molecular dynamics simulation of swift-ion tracks in LiF. *Physical Review B*, 87(24):245424, 2013.

[29] D. A. Young. Molecular dynamics simulation of swift ion damage in lithium fluoride. *Nuclear Instruments and Methods in Physics Research Section B: Beam Interactions with Materials and Atoms*, 225(3):231, 2004.

[30] D. A Young. Evolution of a model ion explosion spike in potassium chloride by molecular dynamics. *Europhysics Letters (EPL)*, 59(4):540, 2002.

[31] M. Tona, S. Takahashi, K. Nagata, N. Yoshiyasu, C. Yamada, N. Nakamura, S. Ohtani, and M. Sakurai. Coulomb explosion potential sputtering induced by slow highly charged ion impact. *Applied Physics Letters*, 87(22):224102, 2005.

[32] R. Stoian, D. Ashkenasi, A. Rosenfeld, and E. E. B. Campbell. Coulomb explosion in ultrashort pulsed laser ablation of Al2O3. *Physical Review B*, 62(19):13167, 2000.

[33] A. A. Correa, J. Kohanoff, E. Artacho, D. Sánchez-Portal, and A. Caro. Nonadiabatic Forces in Ion-Solid Interactions: The Initial Stages of Radiation Damage. *Physical Review Letters*, 108(21):213201, 2012.

[34] N. Itoh, D. M. Duffy, S. Khakshouri, and A. M. Stoneham. Making tracks: electronic excitation roles in forming swift heavy ion tracks. *Journal of Physics: Condensed Matter*, 21(47):474205, 2009.

[35] G. Sciaini, M. Harb, S. G. Kruglik, T. Payer, and C. T. Hebeisen. Electronic acceleration of atomic motions and disordering in bismuth. *Nature*, 458(7234):56, 2009.

[36] T. Zier, E. S. Zijlstra, and M. E. Garcia. Silicon before the bonds break. *Applied Physics A*, 117(1):1, 2014.

[37] V. Recoules, J. Clérouin, G. Zérah, P. M. Anglade, and S. Mazevet. Effect of Intense Laser Irradiation on the Lattice Stability of Semiconductors and Metals. *Physical Review Letters*, 96(5):055503, 2006.

[38] S. T. Murphy, S. L. Daraszewicz, Y. Giret, M. Watkins, A. L. Shluger, K. Tanimura, and D. M. Duffy. Dynamical simulations of an electronically induced solid-solid phase transformation in tungsten. *Physical Review B*, 92(13):134110, 2015.

[39] L. Shokeen and P. K. Schelling. An empirical potential for silicon under conditions of strong electronic excitation. *Applied Physics Letters*, 97(15):151907, 2010.

[40] S. Khakshouri, D. Alfè, and D. M. Duffy. Development of an electron-temperature-dependent interatomic potential for molecular dynamics simulation of tungsten under electronic excitation. *Physical Review B*, 78(22):224304, 2008.

[41] G. E. Norman, S. V. Starikov, and V. V. Stegailov. Atomistic simulation of laser ablation of gold: Effect of pressure relaxation. *Journal of Experimental and Theoretical Physics*, 114(5):792–800, 2012.

[42] F. Dessauer. Point Heat Theory. *Z Physik*, 20:288, 1923.

[43] I. M. Lifshits, M. I. Kaganov, and L. V. Tanatarov. On the theory of radiation-induced changes in metals. *Journal of Nuclear Energy. Part A. Reactor Science*, 12(1):69, 1960.

[44] Z. Lin, L. V. Zhigilei, and V. Celli. Electron-phonon coupling and electron heat capacity of metals under conditions of strong electron-phonon nonequilibrium. *Physical Review B*, 77(7):075133, 2008.

[45] C. Dufour, V. Khomenkov, G. Rizza, and M. Toulemonde. Ion-matter interaction: the three dimensional version of the thermal spike model. Application to nanoparticle irradiation with swift heavy ions. *Journal of Physics D: Applied Physics*, 2011.

[46] P. Drude. Zur Elektronentheorie der Metalle. *Annalen der Physik*, 306(3):566, 1900.

[47] P. Drude. Zur Elektronentheorie der Metalle 2. *Annalen der Physik*, 312(3):687, 1902.

[48] A. Sommerfeld. Zur Elektronentheorie der Metalle. *Die Naturwissenschaften*, 15(41):825, 1927.

[49] A. Sommerfeld. Zur Elektronentheorie der Metalle 2. *Die Naturwissenschaften*, 16(21):374, 1928.

[50] I. A. Baranov, Y. V. Martynenko, S. O. Tsepelevich, Yu. N. Yavlinskii, and R. Behrisch. Inelastic sputtering of solids by ions. *Soviet Physics Uspekhi*, 31(11):1015, 1988.

[51] M. Toulemonde, W. Assmann, C. Dufour, A. Meftah, F. Studer, and C. Trautmann. *Experimental phenomena and thermal spike model description of ion tracks in amorphisable inorganic insulators*, volume 52. The Royal Danish Academy of Sciences and Letters, 2006.

[52] K. Awazu, X. Wang, M. Fujimaki, J. Tominaga, H. Aiba, Y. Ohki, and T. Komatsubara. Elongation of gold nanoparticles in silica glass by irradiation with swift heavy ions. *Phys. Rev. B*, 78(5):54102, 2008.

[53] M. Toulemonde, J.M. Costantini, Ch. Dufour, A. Meftah, E. Paumier, and F. Studer. Track creation in SiO2 and BaFe12O19 by swift heavy ions: a thermal spike description. *Nuclear Instruments and Methods in Physics Research Section B: Beam Interactions with Materials and Atoms*, 116(1):37, 1996.

[54] A. A. Leino, S. L. Daraszewicz, O. H. Pakarinen, K. Nordlund, and F. Djurabekova. Atomistic two-temperature modelling of ion track formation in silicon dioxide. *EPL (Europhysics Letters)*, 110(1):16004, 2015.

[55] Xi Zhang, Blazej Grabowski, Fritz Kormann, Christoph Freysoldt, and Jorg Neugebauer. Accurate electronic free energies of the 3d, 4d, and 5d transition metals at high temperatures. *Physical Review B*, 95:165126, Apr 2017.

[56] B. Huttner. Thermodynamics and transport properties in the transient regime. *Journal of Physics: Condensed Matter*, 11(35):313, 1999.

[57] D. S. Ivanov and L. Zhigilei. Combined atomistic-continuum modeling of short-pulse laser melting and disintegration of metal films. *Physical Review B*, 68(6):064114, 2003.

[58] M. Toulemonde, C. Dufour, A. Meftah, and E. Paumier. Transient thermal processes in heavy ion irradiation of crystalline inorganic insulators. *Nuclear Instruments and Methods in Physics Research Section B: Beam Interactions with Materials and Atoms*, 166:903, 2000.

[59] A. Akkerman and M. Murat. Electron–phonon interactions in silicon: Mean free paths, related distributions and transport characteristics. *Nuclear Instruments and Methods in Physics Research Section B: Beam Interactions with Materials and Atoms*, 350:49, 2015.

[60] E. Pop, R. W. Dutton, and K. E. Goodson. Analytic band Monte Carlo model for electron transport in Si including acoustic and optical phonon dispersion. *Journal of Applied Physics*, 96(9):4998, 2004.

[61] E. Pop, S. Sinha, and K. E. Goodson. Monte Carlo modeling of heat generation in electronic nanostructures. *ASME International Mechanical Engineering Congress and Exposition, Proceedings*, 7:85, 2002.

[62] J. M. Ziman. *Electrons and phonons : the theory of transport phenomena in solids*. Clarendon Press, 2001.

[63] M. Born and R. Oppenheimer. Zur quantentheorie der molekeln. *Annalen der Physik*, 389(20):457, 1927.

[64] S. D. Brorson, A. Kazeroonian, J. S. Moodera, D. W. Face, T. K. Cheng, E. P. Ippen, M. S. Dresselhaus, and G. Dresselhaus. Femtosecond room-temperature measurement of the electron-phonon coupling constant γ in metallic superconductors. *Physical Review Letters*, 64(18):2172, 1990.

[65] S. L. Daraszewicz, Y. L. Giret, D. M. Tanimura, H. Dorothy, A. L. Shluger, and K. Tanimura. Determination of the electron–phonon coupling constant in tungsten. *Applied Physics Letters*, 105(2):023112, 2014.

[66] A. J. Sabbah and D. M. Riffe. Femtosecond pump-probe reflectivity study of silicon carrier dynamics. *Physical Review B*, 66(16):165217, 2002.

[67] P. B. Allen. Theory of thermal relaxation of electrons in metals. *Physical Review Letters*, 59(13):1460, 1987.

[68] B. Arnaud and Y. Giret. Electron cooling and Debye-Waller effect in photoexcited bismuth. *Physical Review Letters*, 2012.

[69] Y. Giret, N. Naruse, S. L. Daraszewicz, Y. Murooka, J. Yang, D. M. Duffy, A. L. Shluger, and K. Tanimura. Determination of transient atomic structure of laser-excited materials from time-resolved diffraction data. *Applied Physics Letters*, 103(25):253107, 2013.

[70] B. Gervais and S. Bouffard. Simulation of the primary stage of the interaction of swift heavy ions with condensed matter. *Nuclear Instruments and Methods in Physics Research Section B: Beam Interactions with Materials and Atoms*, 88(4):355, 1994.

[71] Z. G. Wang, C. Dufour, E. Paumier, and M. Toulemonde. The Se sensitivity of metals under swift-heavy-ion irradiation: a transient thermal process. *Journal of Physics: Condensed Matter*, 6(34):6733, 1994.

[72] S. Klaumunzer. Thermal-spike models for ion track physics: a critical examination. *Matematisk-fysiske Meddelelser*, 52:293, 2006.

[73] M. P. R. Waligórski, R. N. Hamm, and R. Katz. The radial distribution of dose around the path of a heavy ion in liquid water. *International Journal of Radiation Applications and Instrumentation. Part D. Nuclear Tracks and Radiation Measurements*, 11(6):309, 1986.

[74] A. Caro and M. Victoria. Ion-electron interaction in molecular-dynamics cascades. *Physical Review A*, 40(5):2287, 1989.

[75] M. W. Finnis, P. Agnew, and A. J. E. Foreman. Thermal excitation of electrons in energetic displacement cascades. *Physical Review B*, 44(2):567, 1991.

[76] D. M. Duffy and A. M. Rutherford. Including the effects of electronic stopping and electron–ion interactions in radiation damage simulations. *Journal of Physics: Condensed Matter*, 19(1):016207, 2007.

[77] D. M. Duffy, S. Khakshouri, and A. M. Rutherford. Electronic effects in radiation damage simulations. *Nuclear Instruments and Methods in Physics Research Section B: Beam Interactions with Materials and Atoms*, 267(18):3050, 2009.

[78] G. S. Khara, S. T. Murphy, S. L. Daraszewicz, and D. M. Duffy. The influence of the electronic specific heat on swift heavy ion irradiation simulations of silicon. *Journal of Physics: Condensed Matter*, 28(39):395201, 2016.

[79] V. V. Pisarev and S. V. Starikov. Atomistic simulation of ion track formation in UO2. *Journal of Physics: Condensed Matter*, 26(47):475401, 2014.

[80] C. L. Phillips, R. J. Magyar, and P. S. Crozier. A two-temperature model of radiation damage in alpha-quartz. *The Journal of Chemical Physics*, 133(14):144711, 2010.

[81] S. L. Daraszewicz, Y. Giret, N. Naruse, Y. Murooka, J. Yang, D. M. Duffy, A. L. Shluger, and K. Tanimura. Structural dynamics of laser-irradiated gold nanofilms. *Physical Review B*, 88(18):184101, 2013.

[82] H. M. Van Driel. Kinetics of high-density plasmas generated in si by 1.06 - 0.53 micrometer picosecond laser pulses. *Physical Review B*, 35(15):8166, 1987.

[83] S. L. Daraszewicz and D. M. Duffy. Hybrid continuum–atomistic modelling of swift heavy ion radiation damage in germanium. *Nuclear Instruments and Methods in Physics Research Section B: Beam Interactions with Materials and Atoms*, 303:112, 2013.

[84] S. L. Daraszewicz and D. M. Duffy. Extending the inelastic thermal spike model for semiconductors and insulators. *Nuclear Instruments and Methods in Physics Research Section B: Beam Interactions with Materials and Atoms*, 269(14):1646, 2011.

[85] C. A. Klein. Bandgap dependence and related features of radiation ionization energies in semiconductors. *Journal of Applied Physics*, 39(4):2029, 1968.

[86] J. K. Chen, D. Y. Tzou, and J. E. Beraun. Numerical investigation of ultrashort laser damage in semiconductors. *International Journal of Heat and Mass Transfer*, 48(3):501, 2005.

[87] D. M. Duffy, S. L. Daraszewicz, and J. Mulroue. Modelling the effects of electronic excitations in ionic-covalent materials. *Nuclear Instruments and Methods in Physics Research Section B: Beam Interactions with Materials and Atoms*, 277:21, 2012.

[88] T. Grasser, H. Kosina, and S. Selberherr. A review of hydrodynamic and energy-transport models for semiconductor device simulation. *Proceedings of the IEEE*, 91(2):251, 2003.

[89] G. Baccarani and M. R. Wordeman. An investigation of steady-state velocity overshoot in silicon. *Solid-State Electronics*, 28(4):407, 1985.

[90] B. Rethfeld, A. Rämer, N. Brouwer, N. Medvedev, and O. Osmani. Electron dynamics and energy dissipation in highly excited dielectrics. *Nuclear Instruments and Methods in Physics Research Section B: Beam Interactions with Materials and Atoms*, 327:78, 2014.

[91] J. Thorstensen and S. Erik Foss. Temperature dependent ablation threshold in silicon using ultrashort laser pulses. *Journal of Applied Physics*, 112(10):103514, 2012.

[92] A. Rämer, O. Osmani, and B. Rethfeld. Laser damage in silicon: energy absorption, relaxation, and transport. *Journal of Applied Physics*, 116(5):053508, 2014.

[93] G. E. Jellison and F. A. Modine. Optical functions of silicon between 1.7 and 4.7 eV at elevated temperatures. *Physical Review B*, 27(12):7466, 1983.

[94] B. Ziaja, N. Medvedev, V. Tkachenko, T. Maltezopoulos, and W. Wurth. Time-resolved observation of band-gap shrinking and electron-lattice thermalization within X-ray excited gallium arsenide. *Scientific Reports*, 5:18068, 2015.

[95] F. Zhang, S. Li, A. Chen, Y. Jiang, S. Li, and M. Jin. Ultrafast dynamical process of Ge irradiated by the femtosecond laser pulses. *High Power Laser Science and Engineering*, 4(4):12, 2016.

[96] H. S. Sim, S. H. Lee, and K. G. Kang. Femtosecond pulse laser interactions with thin silicon films and crater formation considering optical phonons and wave interference. *Microsystem Technologies*, 14(9-11):1439, 2008.

[97] V. P. Lipp, B. Rethfeld, M. E. Garcia, and D. S. Ivanov. Atomistic-continuum modeling of short laser pulse melting of Si targets. *Physical Review B*, 90(24):245306, 2014.

[98] Y. Gan and J. K. Chen. Combined continuum-atomistic modeling of ultrashort-pulsed laser irradiation of silicon. *Applied Physics A*, 105(2):427, 2011.

[99] L. Shokeen and P. K. Schelling. Role of electronic-excitation effects in the melting and ablation of laser-excited silicon. *Computational Materials Science*, 67:316, 2013.

[100] L. Verlet. Computer experiments on classical fluids. I. Thermodynamical properties of Lennard-Jones molecules. *Physical Review*, 159(1):98, 1967.

[101] W. C. Swope and H. C. Andersen. A computer simulation method for the calculation of equilibrium constants for the formation of physical clusters of molecules: Application to small water clusters. *The Journal of Chemical Physics*, 76(1):637, 1982.

[102] H. J. C. Berendsen, J. P. M. Postma, W. F. van Gunsteren, A. DiNola, and J. R. Haak. Molecular dynamics with coupling to an external bath. *The Journal of Chemical Physics*, 81(8):3684, 1984.

[103] S. Nosé. A unified formulation of the constant temperature molecular dynamics methods. *The Journal of Chemical Physics*, 81(1):511, 1984.

[104] W. G. Hoover. Canonical dynamics: Equilibrium phase-space distributions. *Physical Review A*, 31(3):1695, 1985.

[105] M. W. Finnis and J. E. Sinclair. A simple empirical N-body potential for transition metals. *Philosophical Magazine A*, 50(1):45, 1984.

[106] X. D. Dai, Y. Kong, J. H. Li, and B. X. Liu. Extended Finnis–Sinclair potential for bcc and fcc metals and alloys. *Journal of Physics: Condensed Matter*, 18(19):4527, 2006.

[107] J. Tersoff. New empirical approach for the structure and energy of covalent systems. *Physical Review B*, 37(12):6991, 1988.

[108] G. C. Abell. Empirical chemical pseudopotential theory of molecular and metallic bonding. *Physical Review B*, 31(10):6184, 1985.

[109] T. Kumagai, S. Izumi, S. Hara, and S. Sakai. Development of bond-order potentials that can reproduce the elastic constants and melting point of silicon for classical molecular dynamics simulation. *Computational Materials Science*, 39(2):457, 2007.

[110] T. J Lenosky, B. Sadigh, E. Alonso, V. V Bulatov, and T. D. De La Rubia. Highly optimized empirical potential model of silicon. *Modelling and Simulation in Materials Science and Engineering*, 8(6):825, 2000.

[111] L. Shokeen and P. K. Schelling. Thermodynamics and kinetics of silicon under conditions of strong electronic excitation. *Journal of Applied Physics*, 109(7):073503, 2011.

[112] K. Burke. Perspective on density functional theory. *The Journal of Chemical Physics*, 2012.

[113] P. Hohenberg and W. Kohn. Inhomogeneous electron gas. *Physical Review*, 136(3B):864, 1964.

[114] W. Kohn and L. J. Sham. Self-consistent equations including exchange and correlation effects. *Physical Review*, 140(4A):1133, 1965.

[115] J. P. Perdew, K. Burke, and M. Ernzerhof. Generalized gradient approximation made simple. *Physical Review Letters*, 77(18):3865, 1996.

[116] J. P. Perdew, M. Ernzerhof, and K. Burke. Rationale for mixing exact exchange with density functional approximations. *The Journal of Chemical Physics*, 105(22):9982, 1996.

[117] J. Heyd, G. E. Scuseria, and M. Ernzerhof. Hybrid functionals based on a screened Coulomb potential. *The Journal of Chemical Physics*, 118(18):8207, 2003.

[118] N. D. Mermin. Thermal properties of the inhomogeneous electron gas. *Physical Review*, 137(5A):1441, 1965.

[119] A. Stukowski. Visualization and analysis of atomistic simulation data with OVITO–the Open Visualization Tool. *Modelling and simulation in materials science and engineering*, 18(1):015012, 2010.

[120] C. H. Rycroft, G. S. Grest, J. W. Landry, and M. Z. Bazant. Analysis of granular flow in a pebble-bed nuclear reactor. *Physical Review E*, 74(2):021306, 2006.

[121] G. S. Khara, S. T. Murphy, and D. M. Duffy. Dislocation loop formation by swift heavy ion irradiation of metals. *Journal of Physics: Condensed Matter*, 29(28):285303, 2017.

[122] G. Kaye and T. Laby. Tables of physical and chemical constants.

[123] Z. Yao, M. L. Jenkins, M. Hernández-Mayoral, and M. Kirk. The temperature dependence of heavy-ion damage in iron: A microstructural transition at elevated temperatures. *Philosophical Magazine*, 90(35-36):4623, 2010.

[124] M. Hernández-Mayoral, Z. Yao, M. L. Jenkins, and M. Kirk. Heavy-ion irradiations of Fe and Fe–Cr model alloys Part 2: Damage evolution in thin-foils at higher doses. *Philosophical Magazine*, 88(21):2881, 2008.

[125] X. Yi, M. L. Jenkins, M. Briceno, S. G. Roberts, Z. Zhou, and M. Kirk. In situ study of self-ion irradiation damage in W and W–5Re at 500C. *Philosophical Magazine*, 93(14):1715, 2013.

[126] J. Marian, B. D. Wirth, and J. M. Perlado. Mechanism of formation and growth of 100 interstitial loops in ferritic materials. *Physical Review Letters*, 88(25):255507, 2002.

[127] F. Paschoud, M. Alurralde, G. Szenes, K. Havancsak, and M. Victoria. The distribution of defect clusters produced by swift heavy ions in copper. *Radiation Effects and Defects in Solids*, 126(1):177, 1993.

[128] G.. Kresse and J. Furthmüller. Efficient iterative schemes for ab initio total-energy calculations using a plane-wave basis set. *Physical Review B*, 54(16):11169, 1996.

[129] H. J. Monkhorst and J. D. Pack. Special points for Brillouin-zone integrations. *Physical Review B*, 13(12):5188, 1976.

[130] J. Paier, M. Marsman, K. Hummer, G. Kresse, I. C. Gerber, and J. G. Ángyán. Screened hybrid density functionals applied to solids. *The Journal of Chemical Physics*, 124(15):154709, 2006.

[131] P. Becker, P. Scyfried, and H. Siegert. The lattice parameter of highly pure silicon single crystals. *Zeitschrift für Physik B Condensed Matter*, 48(1):17, 1982.

[132] J. W. Precker and M. A. da Silva. Experimental estimation of the band gap in silicon and germanium from the temperature–voltage curve of diode thermometers. *American Journal of Physics*, 70(11):1150, 2002.

[133] P. K. Schelling. Phase behavior and kinetics of a new bond-order potential for silicon. *Computational Materials Science*, 44(2):274, 2008.

[134] H. Balamane, T. Halicioglu, and W. A. Tiller. Comparative study of silicon empirical interatomic potentials. *Physical Review B*, 46(4):2250, 1992.

[135] T. Steinbach, T. Bierschenk, S. Milz, M. C. Ridgway, and W. Wesch. Swift heavy ion irradiation of crystalline CdTe. *Journal of Physics D: Applied Physics*, 47(6):065301, 2014.

[136] N. Ishikawa, T. Sonoda, T. Sawabe, H. Sugai, and M. Sataka. Electronic stopping power dependence of ion-track size in UO2 irradiated with heavy ions in the energy range of 1 MeV/u. *Nuclear Instruments and Methods in Physics Research Section B: Beam Interactions with Materials and Atoms*, 314:180, 2013.

[137] B. Canut, N. Bonardi, S. M. M. Ramos, and S. Della-Negra. Latent tracks formation in silicon single crystals irradiated with fullerenes in the electronic regime. *Nuclear Instruments and Methods in Physics Research Section B: Beam Interactions with Materials and Atoms*, 146(1):296, 1998.

[138] A. Dunlop, G. Jaskierowicz, and S. Della-Negra. Latent track formation in silicon irradiated by 30 MeV fullerenes. *Nuclear Instruments and Methods in Physics Research Section B: Beam Interactions with Materials and Atoms*, 146(1):302, 1998.

[139] P. Mary, P. Bogdanski, M. Toulemonde, R. Spohr, and J. Vetter. Deep-level transient spectroscopy studies of U-irradiated silicon. *Nuclear Instruments and Methods in Physics Research Section B: Beam Interactions with Materials and Atoms*, 62(3):391, 1992.

[140] IOFFE. Carrier properties of silicon. *http://www.ioffe.ru/SVA/NSM/Semicond/Si/.*

[141] H. Zhao. Temperature dependence of ambipolar diffusion in silicon on insulator. *Applied Physics Letters*, 92(11):112104, 2008.

[142] M. Rosling, H. Bleichner, P. Jonsson, and E. Nordlander. The ambipolar diffusion coefficient in silicon : Dependence on excess-carrier concentration and temperature. *Journal of Applied Physics*, 76(5):2855, 1994.

[143] J. Geist and W. K. Gladden. Transition rate for impact ionization in the approximation of a parabolic band structure. *Physical Review B*, 27(8):4833, 1983.

[144] J. Dziewior and W. Schmid. Auger coefficients for highly doped and highly excited silicon. *Applied Physics Letters*, 31(5):346, 1977.

[145] Y. Giret, S. L. Daraszewicz, D. M. Duffy, A. L. Shluger, and K. Tanimura. Nonthermal solid-to-solid phase transitions in tungsten. *Physical Review B*, 90(9):094103, 2014.

[146] H. Hu, H. Ding, and F. Liu. Quantum Hooke's law to classify pulse laser induced ultrafast melting. *Scientific Reports*, 5:8212, 2015.

[147] J. F. Lutsko, D. Wolf, S. R. Phillpot, and S. Yip. Molecular-dynamics study of lattice-defect-nucleated melting in metals using an embedded-atom-method potential. *Physical Review B*, 40(5):2841, 1989.

[148] J. D. Honeycutt and H. C. Andersen. Molecular dynamics study of melting and freezing of small Lennard-Jones clusters. *The Journal of Physical Chemistry*, 91(19):4950, 1987.